Investigation of inertial sensing using electromagnetically induced transparency

Huang, Chang

2019

Huang, C. (2019). Investigation of inertial sensing using electromagnetically induced transparency. Doctoral thesis, Nanyang Technological University, Singapore.

https://hdl.handle.net/10356/83289

https://doi.org/10.32657/10356/83289

NANYANG TECHNOLOGICAL UNIVERSITY
SINGAPORE

INVESTIGATION OF INERTIAL SENSING USING ELECTROMAGNETICALLY INDUCED TRANSPARENCY

HUANG CHANG

SCHOOL OF PHYSICAL AND MATHEMATICAL SCIENCES

2019

INVESTIGATION OF INERTIAL SENSING USING ELECTROMAGNETICALLY INDUCED TRANSPARENCY

HUANG CHANG

School of Physical and Mathematical Sciences

A thesis submitted to the Nanyang Technological University
in partial fulfilment of the requirements for the degree of
Doctor of Philosophy

2019

Statement of Originality

I hereby certify that the work embodied in this thesis is the result of original research done by me except where otherwise stated in this thesis. The thesis work has not been submitted for a degree or professional qualification to any other university or institution. I declare that this thesis is written by myself and is free of plagiarism and of sufficient grammatical clarity to be examined. I confirm that the investigations were conducted in accord with the ethics policies and integrity standards of Nanyang Technological University and that the research data are presented honestly and without prejudice.

[Input Date Here]

23. Jan. 2019.

Date

[Input Signature Here]

Huang Chang

[Input Name Here]

Huang Chang

Supervisor Declaration Statement

I have reviewed the content and presentation style of this thesis and declare it of sufficient grammatical clarity to be examined. To the best of my knowledge, the thesis is free of plagiarism and the research and writing are those of the candidate's except as acknowledged in the Author Attribution Statement. I confirm that the investigations were conducted in accord with the ethics policies and integrity standards of Nanyang Technological University and that the research data are presented honestly and without prejudice.

[Input Date Here]

23/Jan/2019

Date

[Input Supervisor Signature Here]

[Input Supervisor Name Here]

Lan Shaw En

Authorship Attribution Statement

This thesis contains material from 2 paper(s) published in the following peer-reviewed journal(s) where I was the first and/or corresponding author.

Please amend the typical statements below to suit your circumstances.

Chapter 2 is published as Pei-Chen Kuan, Chang Huang, Wei Sheng Chan, Sandoko Kosen & Shau-Yu Lan, Large Fizeau's light-dragging effect in a moving electromagnetically induced transparent medium *Nature Comm.* **7**, 13030 (2016). DOI: 10.1038/ncomms13030.

The contributions of the co-authors are as follows:

- Prof. Shau-Yu Lan. and Dr. Pei-Chen Kuan conceived and designed the experiment.
- Prof. Shau-Yu Lan wrote the manuscript.
- Wei Sheng Chan and Sandoko Kosen contributed to the early stage of the experiment.
- Dr. Pei-Chen Kuan and I took and analysed the data.
- All authors contributed to the experimental set-up, discussed the results and commented on the manuscript.

Chapter 3 is published as Chang Huang, Pei-Chen Kuan, and Shau-Yu Lan, Laser cooling of ^{85}Rb atoms to the recoil-temperature limit. *Phys. Rev. A* **97**, 023403 (2018). DOI: 10.1103/PhysRevA.97.023403.

The contributions of the co-authors are as follows:

- Prof. Shau-Yu Lan and Dr. Pei-Chen Kuan conceived the experiment.
- Prof. Shau-Yu Lan wrote the manuscript.
- Dr. Pei-Chen Kuan and I built the experimental system.
- I took and analysed data.

Note: If published materials are not inserted as thesis chapters, students must acknowledge co-worker contributions in the acknowledgement section of their thesis.

[Input Date Here]

23 Jan 2019

Date

[Input Signature Here]

Huang Chang

[Input Name Here]

Huang Chang

Acknowledgements

During the past four years, thanks for the support of my parents, my wife, and other family members.

Thanks for the teaching of Prof. Lan Shau-Yu and the resource of the lab from National Research Foundation (NRF) funding to support me for this research project.

Thank you again, I have learned so much.

Ok, it is time to move on.

Chang (Chris) HUANG

January, 2019

Table of Contents

Acknowledgements **1**

Summary **4**

Chapter 1 Introduction **5**

1.1 Cold Atoms 7

1.1.1 Doppler Cooling 8

1.1.2 Magneto-Optical Trap 10

1.1.3 Sub-Doppler Cooling 13

1.1.4 Equipment and Time Sequence 18

1.2 EIT Scheme 22

1.2.1 $\chi^{(1)}$ Diagrams 25

1.2.2 Ω_c Parameter 25

1.2.3 Υ_{21} Parameter 26

1.2.4 Δ and δ Parameter 27

References 29

Chapter 2 Motion Sensing with a Collective State Atoms **32**

2.1 Light Dragging Effect and EIT Enhancement 33

2.2 Experimental Setup 35

2.2.1 Atomic Configuration 35

2.2.2 Optical Setup 38

2.2.3 Timing Sequence 40

2.3 Data and Discussion 41

2.3.1 EIT Spectra 41

2.3.2 Velocity Sensing by Enhanced Light Dragging Effect 43

References 47

Chapter 3 Raman Sideband Cooling 49
3.1 Theory 50
3.1.1 Optical Lattice 50
3.1.1.1 Band Structure 54
3.1.1.2 Crystallography 57
3.1.2 Cooling Mechanism 58
3.2 Experimental Setup 61
3.2.1 Configuration 61
3.2.2 Optical Setup 63
3.2.3 Time Sequence 65
3.3 Data and Discussion 67
3.3.1 Dependency of Cooling Temperature 68
References 76

Chapter 4 Motion Sensing in Periodic Potential 80
4.1 Bloch Oscillation 82
4.1.1 Moving Lattice Picture 82
4.1.2 Quantum Optics Picture 88
4.1.3 Oscillation Efficiency 91
4.2 Experimental Setup 95
4.2.1 Optical Setup 95
4.2.2 Time Sequence 97
4.3 Data and Discussion 99
4.3.1 Theoretical Simulation 102
4.3.2 Phase Measurement Algorithm 107
References 111

Chapter 5 Conclusion 114
References 115

Appendix A Circuit Design 116
A.1 Magnetic Field Switching 116
A.2 PID Stabilization System 118
References 123

Summary

Measuring the motion of quantum particles has been playing a significant role in performing high precision inertial sensing and studying fundamental physics. While most of the motion sensing schemes with cold atoms are based on single-particles. In this thesis, a new measuring method of using a collective state of atoms for motion quantum sensing is introduced. Two experiments were demonstrated to investigate its feasibility. One is related to the light-dragging effect in an electromagnetically induced transparent (EIT) cold ^{85}Rb atomic ensemble. The dragging coefficient F_d was enhanced to 1.67×10^5, which was three orders of magnitude better than the previous experiments. With a large enhancement of the dragging effect, we realised an atom-based velocimeter that has a sensitivity of 1 mm/s, which was two orders of magnitude higher than the velocity width of the atomic medium used before. Such a demonstration could pave the way for motion sensing using the collective state of atoms in a room temperature vapour cell or solid-state material. Another experiment is related to the motion sensing in a driven periodic potential. The motion of the atomic ensemble undergoing Bloch oscillation was measured using the light dragging method. In order to have efficient Bloch oscillation of atoms, the first Raman sideband cooling of ^{85}Rb to pre-cool atomic ensemble close to the recoil temperature (357 nK) was achieved by us. The phase shift measurements showed the linear-like relation to the accelerating time with the data precision 0.00036 rad (0.005 ns, 0.7 mm/s), instead of the stepwise oscillation period τ_B. To observe the stepwise motion, it is required to reduce the lattice field intensity and implement the velocity selection technique to select atoms with a narrow velocity width.

Chapter 1

Introduction

Measuring the motion of some macroscopic object has played a significant role in inertial sensing and navigation. For example, the Doppler radars, as show in Fig. 1.1 [1], rely on measuring the first order Doppler shift of microwaves or ultrasonic waves bouncing off a reflector and analyzing the frequency shift of the data to estimate the corresponding velocities of the object. At single atom level, measuring the motion of atoms has been playing a significant role in performing high precision inertial sensing, such as gravity, gravity gradient, and rotation [2]. It has also been used to study the fundamental physics, including quantum tests of the equivalence principle [3, 4], and measurements of the fine structure constant [5] and Newton's constant G [6]. However, the low probability of the coherent scattering process prohibits precise measurement of light reflecting off atoms.

Alternatively, measuring the velocity of an atom depends on measuring the Doppler shift of the absorption spectrum of single atoms in a large atomic ensemble. Due to the thermal broadening of the ensemble, it is indispensable to map out the velocity distribution of the ensemble to determine the most probable velocity. One method is the Doppler sensitive two-photon Raman velocimetry that uses a pair of counter-propagating laser fields to drive a pair of long-lived states of atoms [7]. By detuning the relative frequency of the counter-propagating laser fields, a sub-group of atoms with finite velocity width, which is determined by the pulse duration, can be selected. Due to the finite temperature of the ensemble, the most probable velocity is then determined by scanning the detuning of the laser fields to map out the Doppler distribution and fit the Maxwell-Boltzmann distribution with the data. As a result, the sensitivity is largely limited by the Doppler broadening

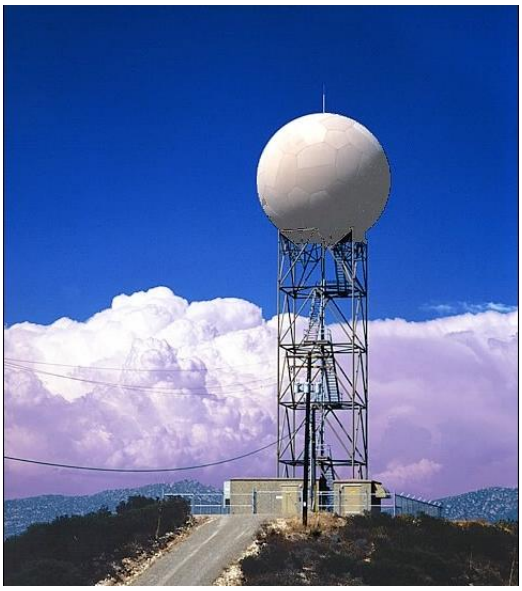

Figure 1.1: A Doppler radar for the forecast (measure the speed of the rain and the hail) and the severe storm research in Kansas City, US [1].

of the atomic ensemble. To improve the sensitivity, one would have to prepare an ensemble at ultra-low temperature [8], which requires a complex laser cooling and trapping setup. In addition, all the measurements must detect the population of atoms in a particular quantum state by shining a resonant light to the atoms and record the absorption or fluorescence from the atomic cloud. Such detection methods destroy the coherent motion of atoms, as a result, each measurement can only detect an instantaneous moment.

Chabé *et al.* used laser-cooled spin-polarized Cesium atoms to achieve a velocity resolution of 70 μm/s, or $v_R/50$ (v_R is the recoil velocity, whose detail is explained in Section 2.2.1) [9]. Reference [10] reported a resolution of $v_R/18$ and Reference [11] reported a resolution of $v_R/17$ (both with Cesium). For Sodium atoms, 290 μm/s, or $v_R/100$ has been reported in Reference [7]. These results were a breakthrough achievement, but the repeated ensemble-reloading and the motion decoherence needed to be improved for the higher efficiency and more experimental requirements, respectively.

This thesis focuses on the development of the new measuring method that detects the phase shift of the light passing through a moving collective quantum state instead of projection measurement of atomic states, and investigating its applications as a new type of motion sensor. This method is based on light-dragging effect using the

collective quantum states of an atomic ensemble, therefore, it can sense the center-of-mass motion of an ensemble directly. In particular, electromagnetically induced transparency (EIT) phenomenon was applied as a versatile and core technology for quantum sensing.

In Section 1.1 and Section 1.2, the laser cooling technology of atoms and the fundamental theory of EIT effect are briefly introduced, respectively. In Chapter 2, we will introduce light dragging effect and use EIT to enhance this effect by three orders of magnitude and demonstrate a method that can sense the centre-of-mass motion of an atomic ensemble directly. In Chapter 4, we will show how to use light dragging effect with EIT to measure the motion of atoms undergoing Bloch oscillations in an optical lattice. However, to ensure the atomic ensemble can perform Bloch oscillation efficiently, the temperature of atoms near the recoil temperature is required. The Raman sideband cooling is, therefore, implemented to cool ^{85}Rb down to few hundreds nano-Kelvin, which is described in Chapter 3.

1.1 Cold Atoms

Atoms in gas form has been widely used for quantum sensing, metrology, and quantum information. They are ideal platforms for those applications because they are stable without any decomposition issue, and have simple energy levels due to no internal rotation and vibration, which is important for manipulating atoms with light.

For room temperature atoms, the velocity distribution of the atomic ensemble causes the Doppler broadening on the atomic transitions, which limits the efficiency and accuracy of atom-light interactions. To avoid this constraint, cooling atoms down to natural linewidth limit is necessary. However, the most powerful fridge or cryogenics could only achieve 4 K (liquid Helium) temperature, which corresponds to a linewidth (FWHM) of its Doppler broadening of about 12 MHz, still larger than the natural linewidth of most atomic transitions, e.g. 6 MHz for ^{85}Rb.

To achieve a lower temperature, the laser cooling technology was invented and refined since 1970s [12, 13]. The basic idea is to directly reduce the atoms' momentum by laser radiation forces, instead of using the heat transfer to another cold reservoir by collisions in the normal fridges. The early laser cooling techniques for atoms

could achieve a temperature lower than 50 μK, and it can also make a condition called "optical molasses" [14], which means that the atoms with a small velocity distribution can be captured by electro-magnetic fields in some small region. In the optical molasses, the motional behaviour of atoms is constrained in a very small range such as that the atoms are sticky with each other, but the friction force in this case is produced by electro-magnetic fields, not the interaction among atoms. Therefore, each atom is identical and isolated, which provides a clean and interesting platform for many applications.

In this experiment, the cooling processes include three parts: Section 1.1.1 Doppler cooling, Section 1.1.2 Magneto-Optical Trap, and Section 1.1.3 Sub-Doppler Cooling. The practice of the above techniques in this experiment is described in Section 1.1.4.

1.1.1 Doppler Cooling

Doppler cooling is a method of laser cooling technologies based on momentum-energy conservation and Doppler effect [15, 16]. The basic idea is shown as Fig. 1.2. Photons with a momentum $\hbar k$ can be absorbed by an atom if the frequency of photons is on-resonant between two energy levels of that atom. The momentum of photon is then transferred to the atom and changes the velocity of the atom. Because of the finite natural linewidth of energy levels, the population relaxes back to the ground state by the spontaneous decay process which emits photons with the momentum $\hbar k$ isotropically, even in the vacuum [17]. This spontaneous relaxation is triggered by the electro-magnetic fields in any space, so the propagation direction of the emission in the relaxation process is isotropic, which results in zero momentum change of the atoms. As a result, the atom can be slowed down by one $\hbar k$ in one absorption-emission cycle.

Considering an atom with a momentum $\mathbf{p}$ absorbs a photon with a momentum $\hbar\mathbf{k}$, the new momentum $\mathbf{p}'$ of the atom after the absorption process is:

$$\begin{aligned} \mathbf{p}' &= \mathbf{p} + \hbar\mathbf{k} \\ p'^2 &= p^2 + (\hbar k)^2 + 2\hbar\mathbf{p}\cdot\mathbf{k}. \end{aligned} \tag{1.1}$$

Using energy conservation, the change of total energy in the process is:

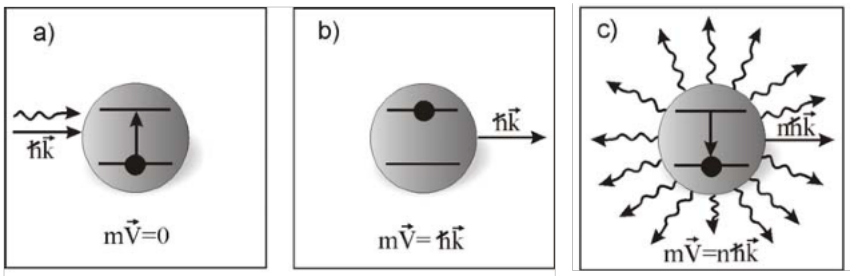

Figure 1.2: (a) A photon with a momentum $\hbar k$ is about to interact with an atom at rest; (b) The photon is absorbed by the atom, and transfers its momentum to the atom; (c) The isotropic relaxation process does not make any change of atom's momentum, so an atom can absorb n photons to receive a momentum $n\hbar k$ [15].

$$E + \frac{p^2}{2M} + \hbar\omega = E' + \frac{p'^2}{2M} \tag{1.2}$$

$$E' = E + \hbar(\omega - \mathbf{k}\cdot\mathbf{v}) - \frac{(\hbar k)^2}{2M}. \tag{1.3}$$

In Eqs. 1.2 and 1.3, E and E' are the internal potential energies of the atom before and after the photon absorption, respectively. $\hbar\omega$ is the photon energy. M and $\mathbf{v}$ are mass and velocity of the atom, respectively. $(\hbar k)^2/2M$ is the recoil energy. The recoil energy is equal to the kinetic energy transferred from a single photon to an atom, which changes the velocity of the atom and is usually very small compared with E. The term $\hbar(\omega - \mathbf{k}\cdot\mathbf{v})$ in Eq. 1.3 is the first order Doppler effect, which shows that the actual photon frequency experienced by the atom is red- or blue- detuned to $\omega - \mathbf{k}\cdot\mathbf{v}$. To decelerate atoms, the photon frequency ω should be red-detuned to achieve the on-resonant transition in the counter-propagating configuration ($\mathbf{k}\cdot\mathbf{v} < 0$) between atoms and photons for the cooling process.

The Doppler cooling mechanism can be represented by the Doppler friction force f [18] as:

$$f_\pm = \pm\frac{\hbar k\Gamma}{2}\frac{\Omega^2/2}{(\delta \mp kv)^2 + \Gamma^2/4)} \tag{1.4}$$

$$f = f_+ - f_- \approx \hbar k^2 \frac{\delta\Omega^2\Gamma}{(\delta^2 + \Gamma^2/4)^2} v, \tag{1.5}$$

where f_+ and f_- are the friction forces along and opposite to the axis of atoms' motion, Γ is the natural linewidth of the excited state, Ω is the Rabi frequency of

the light-atom interaction, and δ is the photon detuning, which is equal to $\omega - \omega_{ab}$ (ω_{ab} is the energy separation of this two level system, $|a\rangle$ and $|b\rangle$, used in the cooling process). In the low-velocity limit $kv \ll \Gamma, \delta$, the total Doppler friction force f can be approximated in Eq. 1.5 and is shown in Fig. 1.3. The friction force in Eq. 1.4 is derived from the rate of momentum transfer from a photon to an atom, which is equal to $\hbar k \times \gamma_{ab}$, where γ_{ab} is the photon scattering rate on $|a\rangle \rightarrow |b\rangle$ transition. The frequency response of the friction force is, therefore, the same as that of the scattering rate. In addition, the friction force spectral profile is shifted due to Doppler effect. The choice of the detuning δ depends on the capture range of the line profile. If it is too large, the cooling becomes inefficient because the cooling temperature limit is set too high in the beginning; if it is too small, there is only a small fraction of atoms participating in the process. There is one more point should be noticed: f is proportional to the light intensity (included in Ω^2), which is very different from the behaviour of sub-Doppler cooling (see Section 1.1.3), which is independent of the light intensity. Owing to random fluctuation of the force, which gives rise to diffusion in momentum space, the minimum temperature T_D of Doppler cooling is obtained for $\delta = -\Gamma/2$ [19] as shown in Eq. 1.6. For ^{85}Rb, T_D is about 140 μK.

$$k_B T_D = \frac{\hbar\Gamma}{2}. \tag{1.6}$$

1.1.2 Magneto-Optical Trap

The Doppler cooling just offers a mechanism to decelerate atoms' motion, but atoms could still diffuse out of the cooling field area. Magneto-Optical Trap (MOT) configuration offers a magnetic potential to confine atoms, as shown in Fig. 1.4. To confine atoms, a pair of anti-Helmholtz coils (see Fig. 1.5) is applied [20]. It provides a region of a quadrupole magnetic field as shown in Fig. 1.6, and uses the magnetic field gradient to produce a position-dependent Zeeman shift on the atoms for the trapping purpose.

The magnetic field gradient near the central position is a linear function of positions along x, y, and z axes, where z axis is defined in Fig. 1.5, and x and y axes are symmetrically identical. In the 1D case along the z-axis, the magnetic field is $\mathbf{B}_z(z) = \mathrm{b}z\mathbf{z}$, where b is a constant. The Zeeman shift induced by B_z is

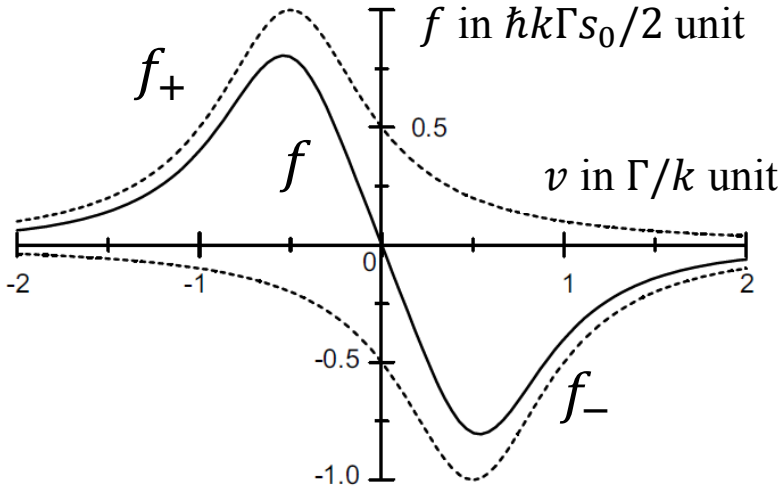

Figure 1.3: The friction forces of f_+, f_- and total f are a function of the atomic velocity v with $\delta = -\Gamma/2$ [18].

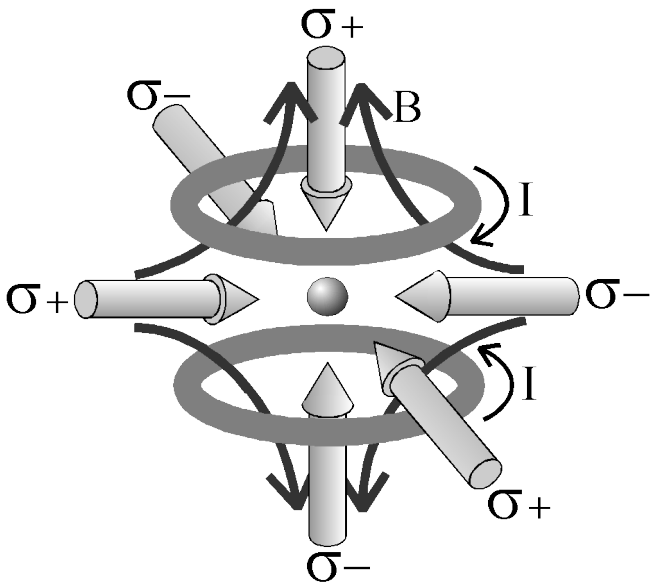

Figure 1.4: A schematic of MOT shows the alignment of the cooling laser beams and the magnetic field produced by a pair of coils. [18]

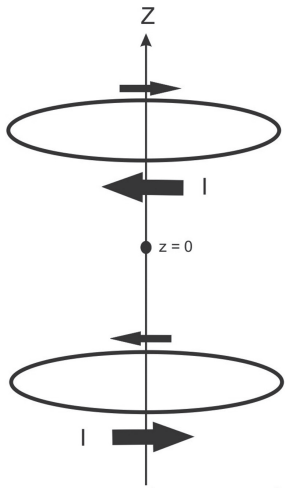

Figure 1.5: Anti-Helmholtz coils. The directions of the current flows in two coils are opposite [20], which produce a quadrupole magnetic field in the MOT area.

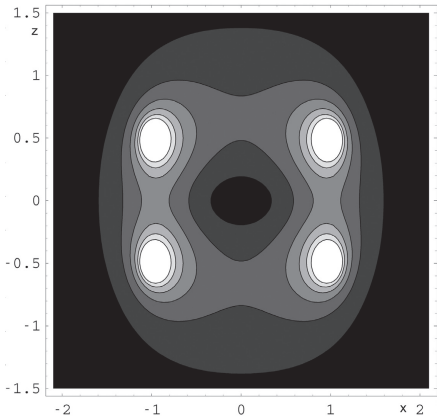

Figure 1.6: The contour plot of quadruple magnetic field on xz plane shows the magnetic field gradient. The brightness corresponds to the field strength [20].

$g_F \mu_B B(z)$, where g_F is the g-factor including the orbital L, spin S, total J angular momentum of the electron, and nuclear angular momentum I as shown in Eqs. 1.7 - 1.9 [21], where μ_B is Bohr magneton $e\hbar/2m_e$.

$$\mathbf{J} = \mathbf{L} + \mathbf{S} \tag{1.7}$$

$$\mathbf{F} = \mathbf{L} + \mathbf{S} + \mathbf{I} \tag{1.8}$$

$$g_F \simeq g_J \frac{F(F+1) - I(I+1) + J(J+1)}{2F(F+1)}. \tag{1.9}$$

Combining the Zeeman shift with Doppler cooling, the friction forces in 1D cooling beams arrangement become:

$$f_\pm = \pm \frac{\hbar k \Gamma}{2} \frac{\Omega^2/2}{(\delta \mp \frac{g_F \mu_B b}{\hbar} z \mp kv)^2 + \Gamma^2/4)}. \tag{1.10}$$

The cooperation between Doppler cooling and position-dependent Zeeman shift is explained In Fig. 1.7. The Zeeman effect modifies the detuning based on the spatial function of the quadrupole magnetic field. The heating effect caused by the cooling field from the opposite direction could be eased with the help of the opposite Zeeman shifts. Taking an example in Fig. 1.7, the atoms in + position can

be decelerated by σ^- polarized cooling field and accelerated by σ^+ polarized cooling field. With the Zeeman shifts by the quadruple field, they have lower probability to absorb σ^+ polarized cooling field due to an increased detuning from the cooling field frequency. The MOT quadruple magnetic field is a function of the space, which not only increases the cooling efficiency, but also produces a trap with zero magnetic field near the center, which provides a functionality to gather the atoms near the central region. The same analysis can be extended to the 3D case. In this experimental setup, three circularly-polarized light fields are applied as the cooling light sources described in Section 1.1.4.

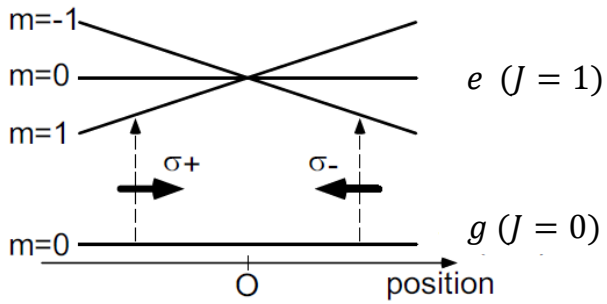

Figure 1.7: In $|g, J = 0\rangle$ to $|e, J = 1\rangle$ case, Zeeman shifts change linearly near the center. σ^+ and σ^- are the right-hand and left-hand circular polarization of the cooling fields [18].

1.1.3 Sub-Doppler Cooling

The lowest temperature that can be achieved in Doppler cooling in Eq. 1.6 is unfortunately still too high for some applications, such as the production of Bose-Einstein Condensate. In 1988, the first sub-Doppler cooling was demostrated by W. Phillips' group in the National Institute of Standards and Technology (NIST) [22]. They developed a new mechanism to overcome the Doppler limit and showed a new limit of the temperature T_R in Eq. 1.11. After many years of studies, the Nobel Prize in Physics 1997 was jointly awarded to Steven Chu, Claude Cohen-Tannoudji and William D. Phillips for the development of sub-Doppler cooling mechanisms to appreciate their contributions in laser cooling technologies and fundamental physics.

$$k_B T_R = \frac{(\hbar k)^2}{2M}. \tag{1.11}$$

In Eq. 1.11, T_R is called the recoil temperature, which corresponds to the kinetic energy of the atom with the mass M absorbing one photon with the momentum $\hbar k$. The recoil energy $k_B T_R$ (frequency) in Eq. 1.11 is typically much smaller than the nature linewidth Γ of the excited state in Eq. 1.6, so sub-Doppler cooling can achieve a cooling temperature much lower than Doppler limit T_D. The mechanism of sub-Doppler cooling is highly related to the polarization variation of the cooling field, so it is also called that polarization gradient cooling (PGC). There are two kinds of configurations, $\sigma^+ - \sigma^-$ and $lin \perp lin$ for sub-Doppler cooling schemes. In our experiment, we use $\sigma^+ - \sigma^-$ configuration of light fields. To analyse the mechanism, the total electric field $E(z,t)$ composed with two counter-propagating light is written as [23]:

$$E(z,t) = \varepsilon^+(z) e^{(-i\omega t)} + c.c., \tag{1.12}$$

where the amplitude and polarization term $\varepsilon^+(z)$ is given by:

$$\varepsilon^+(z) = \varepsilon_0 \epsilon_+ e^{ikz} + \varepsilon_0' \epsilon_- e^{-ikz} \tag{1.13}$$

$$\epsilon_+ = -\frac{1}{\sqrt{2}}(\epsilon_x + i\epsilon_y) \tag{1.14}$$

$$\epsilon_- = \frac{1}{\sqrt{2}}(\epsilon_x - i\epsilon_y). \tag{1.15}$$

In Eq. 1.13, ϵ_+ and ϵ_- are unit vectors for two opposite circular polarizations, and ε_0 and ε_0' are amplitudes of fields with corresponding polarizations. After rearranging Eq. 1.13, it becomes:

$$\varepsilon^+(z) = \frac{1}{\sqrt{2}}(\varepsilon_0' - \varepsilon_0)\epsilon_X - \frac{i}{\sqrt{2}}(\varepsilon_0' + \varepsilon_0)\epsilon_Y \tag{1.16}$$

$$\epsilon_X = \epsilon_x \cos(kz) - \epsilon_y \sin(kz) \tag{1.17}$$

$$\epsilon_Y = \epsilon_x \sin(kz) + \epsilon_y \cos(kz). \tag{1.18}$$

From Eq. 1.16, it can be found that these two counter-propagating light fields form a standing wave with a linear polarization rotating along z-axis, as shown in Fig. 1.8.

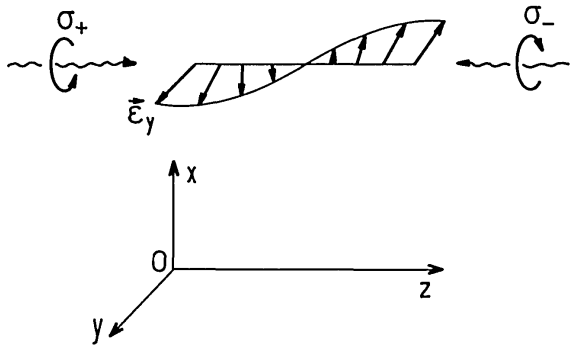

Figure 1.8: The polarization of the standing wave in $\sigma^+ - \sigma^-$ configuration [23].

From Fig. 1.8, it can be seen that the ellipticity of the polarization at all positions keeps the same. Taking $J_g = 1 \leftrightarrow J_e = 2$ transition as an example and considering the transition probabilities with Clebsch-Gordan coefficients shown in Fig. 1.9, the population in different ground Zeeman states after optical pumping with π polarization would be different, where $|g_{-1}\rangle$, $|g_0\rangle$, and $|g_1\rangle$ in the steady state are equal to 4/17, 9/17, and 4/17, respectively.

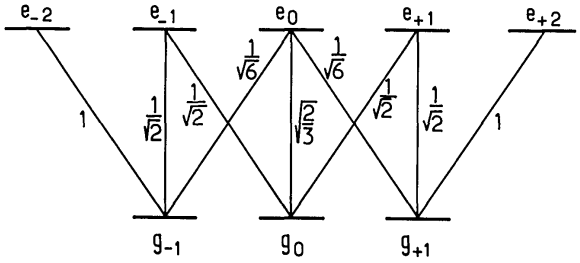

Figure 1.9: Clebsch-Gordan coefficients of $J_g = 1 \leftrightarrow J_e = 2$ transition [23].

In addition, the light fields make energy shifts Δ' of ground state through AC Stark shift [24], so the difference of transition probabilities between $|g_0\rangle \rightarrow |e_0\rangle$ and $|g_{\pm 1}\rangle \rightarrow |e_{\pm 1}\rangle$ causes the energy splitting of the ground state, as seen in Fig. 1.10. This splitting does not change along z axis because all atoms on the z-axis experience the same linearly polarized electric field, which is very different from the mechanism of Sisyphus effect in $lin\perp lin$ configuration [23].

To simplify the theoretical analysis, we assume that $\varepsilon_0' = \varepsilon_0$ in Eq. 1.16. We also assume the atoms stay at rest on the origin (z=0), and the electric field of the cooling field is aligned on y-axis. Now we define y-axis as the quantization axis

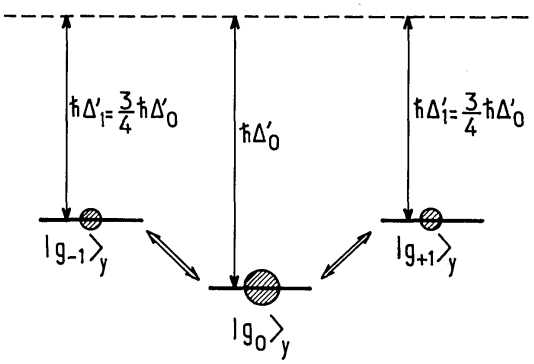

Figure 1.10: Energy shifts of the ground state. $\Delta'_{0,\pm1}$ means the energy shifts of $|g_{0,\pm1}\rangle$. Note all Δ' are negative due to red-detuned light frequency for cooling processes and $\Delta'_0 = (4/3)\Delta'_{\pm1}$ can be derived from the ratio of transition probabilities [23].

of atoms, so the atoms would experience the optical pumping with π polarization, and $|g_{0,\pm1}\rangle_y$ would be the eigenstates of J_y (J is the angular momentum operator). However, when the atoms are moving on z-axis, they would feel a rotating electric field. If we describe the atoms in a rotating and moving frame, the inertial fields which act on atoms keep the same as that at rest, but append an extra magnetic field energy coming from the rotating frame along z-axis. Based on the real condition, we made two assumptions:

$$\Gamma' \ll |\Delta'| \ll \Gamma \tag{1.19}$$

$$kv \ll |\Delta'|. \tag{1.20}$$

In Eq. 1.19, Γ' is the scattering rate of the ground state for population transfers during the cooling process, and Γ is the atomic natural linewidth of the excited state, the same as the definition in Eq. 1.4. In Eq. 1.20, k is the wavenumber of the cooling field; v is the velocity of the atom, the same as that in Eq. 1.3. From Eqs. 1.19 and 1.20, the energy splitting among different Zeeman states is much larger than the linewidth of each level, which makes sub-Doppler cooling possible to work. The light shift Δ' is tuned to be much smaller than Γ, which makes the friction force f of sub-Doppler cooling is much larger than Doppler cooling (it will be explained later). The parameter kv with the atomic velocity is supposed to be much smaller than the light shift Δ', because extra Zeeman shifts show up when the velocity is

too high, which can destroy the working procedures of sub-Doppler cooling. It is why sub-Doppler cooling has to follow Doppler cooling to work in the whole cooling process, and we can treat it as a perturbation in the analysis.

We apply the perturbation theory to calculate the effect from the extra magnetic field, which potential V_{mov} could be shown as:

$$V_{\text{mov}} = kvJ_z. \tag{1.21}$$

Because J_y and J_z cannot commute, the perturbed eigenstates $\overline{|g_{0,\pm1}\rangle_y}$ at rotating moving frame would be the linear combination of $|g_{0,\pm1}\rangle_y$ as a function of the energy shifts Δ' and the velocity factor kv shown in Eqs. 1.22 and 1.23:

$$\overline{|g_0\rangle_y} = |g_0\rangle_y + \frac{kv}{\sqrt{2}(\Delta'_0 - \Delta'_1)}(|g_{+1}\rangle_y + |g_{-1}\rangle_y) \tag{1.22}$$

$$\overline{|g_{\pm1}\rangle_y} = |g_{\pm1}\rangle_y - \frac{kv}{\sqrt{2}(\Delta'_0 - \Delta'_1)}|g_0\rangle_y. \tag{1.23}$$

Since the circularly polarized light is used as the cooling source, so we calculate the average amount of J_z [23] as:

$$\langle J_z\rangle = \overline{{}_y\langle g_0|}J_z\overline{|g_0\rangle_y} + \overline{{}_y\langle g_{+1}|}J_z\overline{|g_{+1}\rangle_y} + \overline{{}_y\langle g_{-1}|}J_z\overline{|g_{-1}\rangle_y} = \frac{40}{17}\frac{\hbar kv}{\Delta'_0}. \tag{1.24}$$

$\langle J_z\rangle$ is proportional to the population difference between $|g_{+1}\rangle_z$ and $|g_{-1}\rangle_z$. Owing to the different transition probabilities between $|g_{+1}\rangle_z$ and $|g_{-1}\rangle_z$ interacting with two circularly polarized cooling fields (see Fig. 1.9), if the atom is moving toward $+z$ direction ($v > 0$), the population on $|g_{-1}\rangle_z$ is more than that on $|g_{+1}\rangle_z$, so the σ^- transition dominates in this case. In our example model in Fig. 1.8, the light field with σ^- polarization propagates in -z direction, which makes the atom decelerated. The same situation happens to the atom moving toward -z direction. To quantize the ability of sub-Doppler cooling, the friction force f can be derived as:

$$f = \frac{dp}{dt} = \frac{\langle J_z\rangle}{\hbar} \cdot \hbar k \cdot \Gamma' \approx \hbar k^2 \frac{\Gamma'}{\Delta'} v. \tag{1.25}$$

Under the low-intensity limit such as $|\Delta'| \ll \Gamma$ (see Eq. 1.19) and $\Omega \ll \Gamma$, the approximations of Γ' and Δ' are given as follows [23]:

$$\Gamma' \approx \frac{\Omega^2 \Gamma}{\delta^2} \tag{1.26}$$

$$\Delta' \approx \frac{\Omega^2}{\delta}. \tag{1.27}$$

The friction force of sub-Doppler cooling can then be approximated as:

$$f \approx \hbar k^2 \frac{\Gamma}{\delta} v. \tag{1.28}$$

If we compare the orders of magnitude of the friction forces of sub-Doppler cooling and Doppler cooling ($f_{\text{Doppler}} \approx \Omega^2/\delta^2 \times f_{\text{sub-Doppler}}$, see Eq. 1.5), we can find that sub-Doppler cooling can offer much stronger friction forces than that Doppler cooling does, because the detuning δ has the same order as Γ in the cooling process. In addition, the friction forces are independent of the intensity of the cooling light field as Eq. 1.28 shows, because the intensity terms, which are proportional to Ω^2 in Γ' and Δ', cancel each other in Eq. 1.25.

Sub-Doppler cooling is widely-used in the production of cold atoms following the Doppler cooling process, because the operation in the experiment is straightforward, even though some fraction of atoms are lost during the process. Although a combination of Doppler and sub-Doppler cooling can typically cool down atoms to a few tens μK, it is still not sufficient for some applications that require atoms in the recoil temperature range. To improve this situation, a cooling method that can bring the temperature of atoms down to recoil temperature is required, such as Raman sideband cooling. Our implementation of Raman sideband cooling will be described in Chapter 3.

1.1.4 Equipment and Time Sequence

In this experiment, the cold atomic ensemble was produced and maintained by a commercial MOT equipment (miniMOT from ColdQuanta), as shown in Figs. 1.11 and 1.12. The miniMOT package is a combo set that provides the cooling beam alignment, MOT coils, Rb atom dispenser, quartz cell vacuum chamber, built-in ion pump and control units. It is a compact setup but we modified it to fit our needs:

1. We rearranged the MOT beams optics so that other experimental apparatus, such as the RF waveguide and CCD camera, can be brought close to atoms.

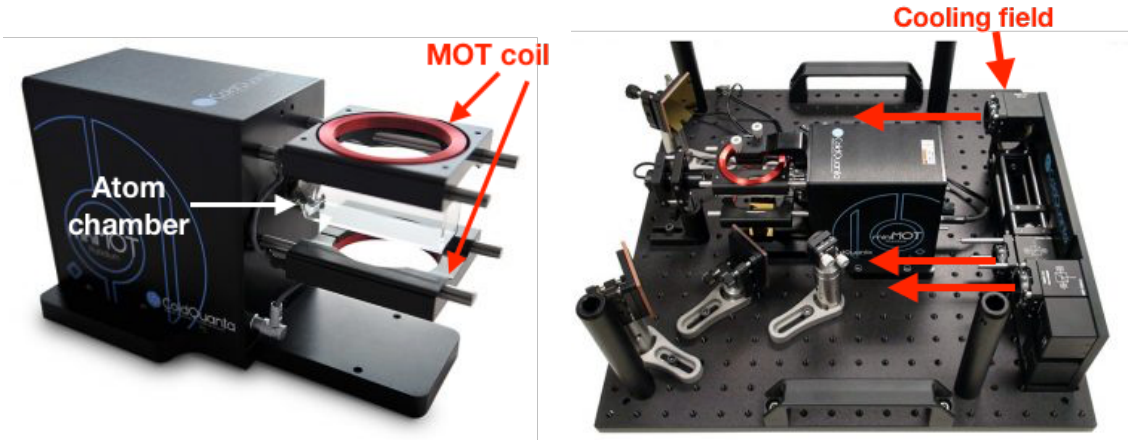

Figure 1.11: miniMOT chamber and its package. The atom chamber, MOT coils and the path of cooling fields are indicated in the figure.

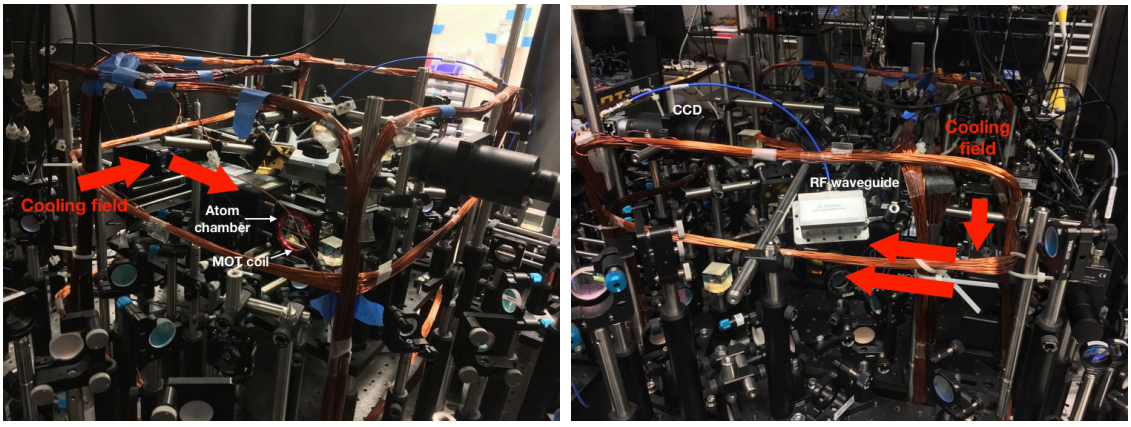

Figure 1.12: miniMOT package in our experimental setup. The atom chamber, MOT coils, the path of cooling fields, RF waveguide and CCD are indicated in the figure.

2. The vacuum pressure indicator was broken after a year of operation. We used the MOT loading time to gauge the vacuum pressure inside the chamber.

3. The current control of the coil is not programmable, so we modified the power supply of the coil pair to have full control of its current, and connect it to our home-made voltage-control current box (see Appendix A.1). Owing to this modification and an analogue voltage-control channel in our controlling system (ADbasic from ADwin), the strength of the magnetic field for our MOT can be programmed.

4. The factory-set maximum current of MOT coil is 1 A. This limits the attainable current for the compressed MOT [25], which requires a current of a few amperes. We used extra coils in the crowded space near the chamber to make this trick barely feasible.

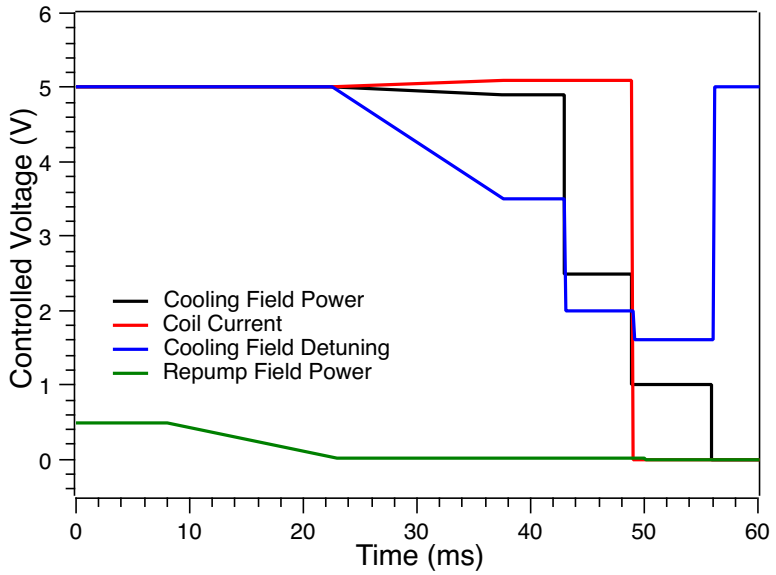

Figure 1.13: The time sequence near the end of the cold atoms production. The four voltage-controlled parameters are the cooling field power, the coil current, the cooling field detuning and the repump field power. The shown time in this figure started after 1-2 s cold atoms production with full power of the cooling field, the MOT magnetic field and the repump field (the control voltage of the cool field power, the coil current, the cooling field detuning and the repump field power were 5 V, 5 V, 5 V and 0.5 V, respectively).

We coupled the red-detuned cooling field and the on-resonant repump field into a

single-mode polarization-maintaining (PM) optical fibre and guided these two fields into the miniMOT package as shown on the right-hand side of Fig. 1.11. A telescope expanded the beam into a diameter of about 1 cm. A beam splitter followed by a quarter waveplate (QWP) separated the beam into three parts and converted their polarization into the circular polarization. These three beams were then guided to the center of the glass cell chamber by three square gold mirrors. They were retro-reflected back by three gold mirrors to form a three-dimensional MOT geometry together with the quadrupole magnetic trap.

Figure 1.13 shows the time sequence close to the end of the cooling process. We usually build and load the cold atoms from the dispensor for 1-2 s, and increase the current of MOT coils at 24th ms to start the MOT compression (see the timescale in Fig. 1.13). During the compressed MOT stage (24th - 38th ms), the cooling field power linearly decreased to 98% of the initial power, meanwhile, the cooling field detuning (absolute values) also linearly increased from -15 to -31 MHz, which means the cooling field releases those cooled and trapped atoms from the shallower and shallower optical lattice built by the cooling field. The coil current (magnetic field) linearly increased from 1 to 1.02 A to make the magnetic trap deeper and denser in space. However, it cannot be increased more due to the current limitation of miniMOT. At about 50th ms, the magnetic field was sharply turned off within 0.1 ms, the cooling field power and detuning were reduced to 20% of the initial power and -50 MHz, respectively. Sub-Doppler cooling stage started to cool down atoms to 30 μK of our ^{85}Rb atomic ensemble.

The green line in Fig. 1.13 indicates the relative power of the repump field. The repump field was used to prevent the optical pumping of atoms to other dark states due to the detuning of the cooling field. The power of the repump field was 1/20 of the cooling field power, which was linearly reduced to 0 from 8th to 21st ms, because we tended to transfer the population to the dark state during the period close to the ending of Doppler cooling stage. This strategy is called “dark MOT”, which reduced the heating effect caused by the optical pumping from the cooling field and the repump field, so that we could get a colder atomic ensemble before sub-Doppler cooling stage.

1.2 EIT Scheme

Electromagnetically induced transparency (EIT) is a non-linear optical phenomenon, which involves the interaction among a non-linear medium and multi-photons to achieve the quantum interference, found in 1990 [26]. As shown in Fig. 1.14, a simple EIT scheme can be implemented in a three-level atomic system, wherein two lower atomic states $|1\rangle$ and $|2\rangle$ with long coherence time are coupled to a third state $|3\rangle$ by optical excitations. A control field resonating on the $|2\rangle \rightarrow |3\rangle$ transition creates a quantum interference with a probe field resonating on the $|1\rangle \rightarrow |3\rangle$ transition. The "transparent" phenomenon of EIT means that the on-resonant probe field is not absorbed because of the presence of the control field, which can be explained in two pictures: dressed atom picture and bare atom picture, see Figs. 1.14 and 1.15.

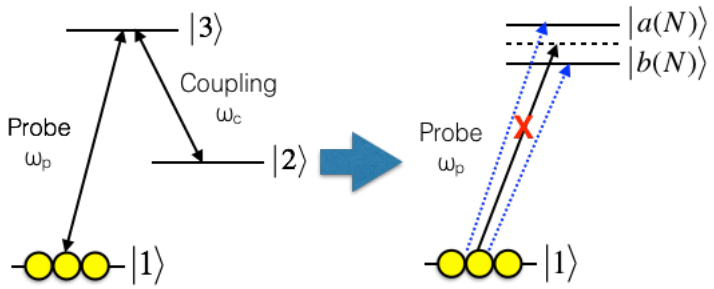

Figure 1.14: Dressed atom picture for EIT mechanism.

Dressed atom picture is a way to describe atom-photon interaction [27], where atom states $(|1\rangle, |2\rangle, |3\rangle \cdots)$ dress up photon number states $(|N\rangle, |N+1\rangle \cdots)$. When the photons are resonant on the transition of the two level system of an atom, the special dressed quantum states are given as Eqs. 1.29 and 1.30:

$$|a(N)\rangle = \frac{1}{\sqrt{2}}(|2, N+1\rangle + |3, N\rangle) \tag{1.29}$$

$$|b(N)\rangle = \frac{1}{\sqrt{2}}(|2, N+1\rangle - |3, N\rangle). \tag{1.30}$$

The definitions of $|a(N)\rangle$ and $|b(N)\rangle$ are shown in Fig. 1.14. Note that the energy levels of $|a(N)\rangle$ and $|b(N)\rangle$ are separated by a energy splitting $\hbar\Omega$, so the probe field becomes off-resonant. In addition, the energy splitting $\hbar\Omega$ is proportional to the square root of the control field intensity, and off-resonant transitions are still possible

to occur in a lower probability. To achieve the obvious transparency phenomenon, the intensity ratio of the control field to the probe field should be as large as possible. In our experiment, the intensity ratio is about 10.

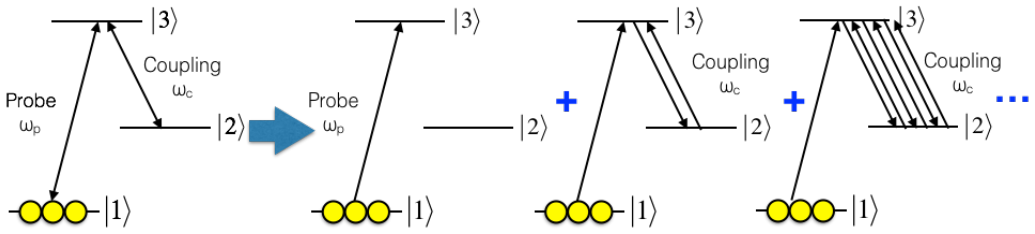

Figure 1.15: Bare atom picture for EIT mechanism.

In bare atom picture, we can use double two-level systems to explain the EIT mechanism.

$$\Psi = c_a(t)e^{-i\omega_a t}|a\rangle + c_b(t)e^{-i\omega_b t}|b\rangle \tag{1.31}$$

$$c_a(t) = \cos(\frac{\Omega}{2}t) \Rightarrow |c_a(t)|^2 = \frac{1+\cos(\Omega t)}{2} \tag{1.32}$$

$$c_b(t) = \sin(\frac{\Omega}{2}t) \Rightarrow |c_b(t)|^2 = \frac{1-\cos(\Omega t)}{2}. \tag{1.33}$$

Equations 1.31 - 1.33 are the descriptions of two-level system $|a\rangle$ and $|b\rangle$ of an atom interacting with an optical field with a Rabi frequency Ω. We take $|1\rangle$ and $|3\rangle$ in Fig. 1.15 as $|a\rangle$ and $|b\rangle$ in Eq. 1.31, and all the population are initially in the state $|a\rangle$ ($c_a(0) = 1$). The population in $|a\rangle$ can be transferred to $|b\rangle$ by a π pulse with the time π/Ω_p. Now we take $|3\rangle$ and $|2\rangle$ in Fig. 1.15 as $|a\rangle$ and $|b\rangle$ in Eq. 1.31. If the Rabi frequency Ω_c of the control field is large enough, the control field can give the atom a $(2+4n)\pi$ pulse (n can be 0 or any positive integer) within the time $(2+4n)\pi/\Omega_c$. When the time is still shorter than the π pulse time π/Ω_p of the probe field, the destructive interference could occur on $|3\rangle$, where no transition is allowed on $|1\rangle \rightarrow |3\rangle$ transition (see Fig. 1.16).

In the quantitative analysis, because the coherence of atomic states is crucial for the quantum interference in EIT process (see Section 1.2.3), the density matrix is more suitable to describe the EIT effect. As shown in Fig. 1.17, by taking the spontaneous relaxation rate Γ and the dephasing rate γ into account, the equation of motion with the density matrix is [28]:

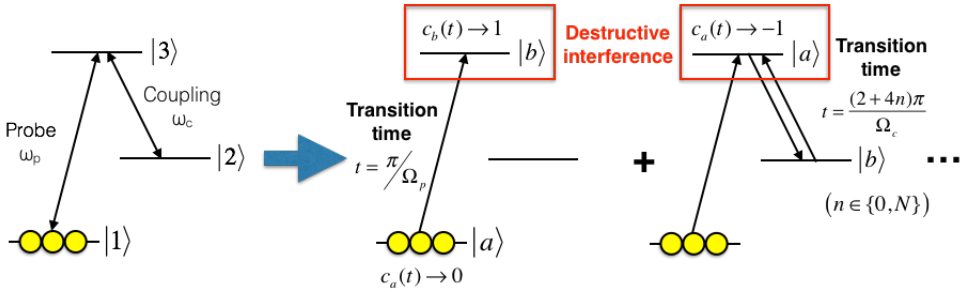

Figure 1.16: The detail of EIT mechanism for the bare atom picture.

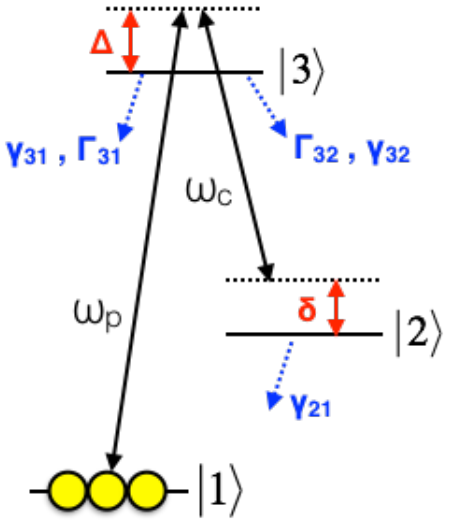

Figure 1.17: EIT three-level system with spontaneous relaxation rate Γ, dephasing rate γ due to collisions among atoms, single-photon detuning Δ and two-photon detuning δ.

$$\frac{d\rho}{dt} = \frac{1}{i\hbar}[H,\rho] + \begin{bmatrix} \Gamma_{31}\rho_{33} & -\gamma_{21}\rho_{12} & -(\frac{\Gamma_{31}}{2}+\gamma_{31})\rho_{13} \\ -\gamma_{21}\rho_{21} & \Gamma_{32}\rho_{33} & -(\frac{\Gamma_{32}}{2}+\gamma_{32})\rho_{23} \\ -(\frac{\Gamma_{31}}{2}+\gamma_{31})\rho_{31} & -(\frac{\Gamma_{32}}{2}+\gamma_{32})\rho_{32} & -(\Gamma_{31}+\Gamma_{32})\rho_{33} \end{bmatrix}. \quad (1.34)$$

Solving Eq. 1.34, the electric susceptibility $\chi^{(1)}$ for the probe field can be obtained as follows:

$$\chi^{(1)}(-\omega_p,\omega_p) \propto \rho_{31} \propto \frac{4\delta(|\Omega_c|^2 - 4\delta\Delta) - 4\Delta\Upsilon_{21}^2}{||\Omega_c|^2 + (\Upsilon_{31}+i2\Delta)(\Upsilon_{21}+i2\delta)|^2} + i\frac{8\delta^2\Upsilon_{31} + 2\Upsilon_{21}(|\Omega_c|^2 + \Upsilon_{21}\Upsilon_{31})}{||\Omega_c|^2 + (\Upsilon_{31}+i2\Delta)(\Upsilon_{21}+i2\delta)|^2}, \quad (1.35)$$

where Δ and δ are single-photon detuning $(\omega_{31} - \omega_p)$ and two-photon detuning $(\omega_{21} - (\omega_p - \omega_c))$, respectively. Γ and γ are the spontaneous relaxation rate and dephasing rate, respectively, as indicated in Fig. 1.17. $\Upsilon_{31} = \Gamma_{31}/2 + \Gamma_{32}/2 + \gamma_{31}$. $\Upsilon_{21} = \gamma_{21}$ $(\Gamma_{21} = 0)$. Because Eq. 1.35 has a complicated form and includes many variables, some special conditions will be discussed.

1.2.1 $\chi^{(1)}$ Diagrams

Figure 1.18 shows the behaviour of EIT effects. When each parameters in Eq. 1.35 are fixed except ω_p ($\Delta = \delta$ in this case), the EIT produces a narrow spectral window in $Re[\chi^{(1)}]$ and $Im[\chi^{(1)}]$ diagrams. Figure 1.18 also shows the potential application called "slow light". Owing to the very narrow EIT spectral window, the slope of $Re[\chi^{(1)}]$ to the frequency can be very large, which makes the group velocity v_g (see Eq. 1.36) of the light in the EIT medium much smaller than the light speed c in the vacuum, so the interaction time between light and EIT medium would be much longer than normal condition. We apply this dispersive condition for demonstrating the light-dragging effect in Chapter 2.

$$v_g = \frac{c}{n + \omega_p(\frac{dn}{d\omega_p})} \quad (1.36)$$

1.2.2 Ω_c Parameter

The magnitudes of Ω_c are related to the intensity of the control field. Figure 1.19 shows the correlation between the width of the EIT window and Ω_c, which is con-

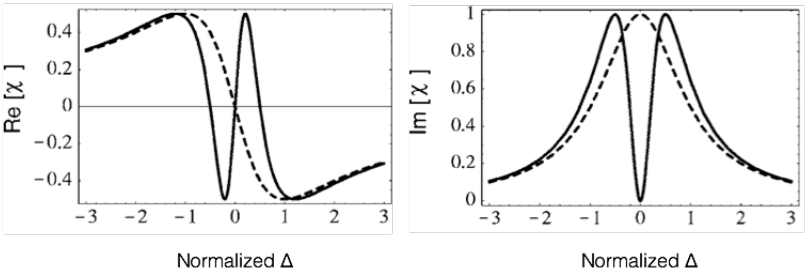

Figure 1.18: The plots of the refractive index $Re[\chi^{(1)}]$ and the absorbance $Im[\chi^{(1)}]$ as a function of normalized Δ. Dashed lines are the conditions without the control field, and solid lines are the conditions with the control field [28].

sistent with the results of the dressed atom picture in Fig. 1.14.

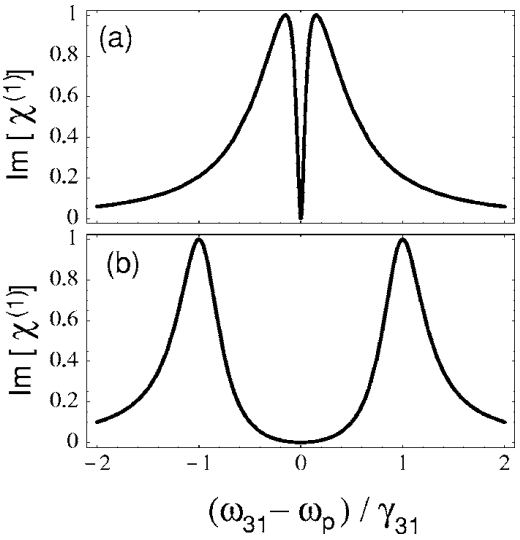

Figure 1.19: The plots of the absorbance $Im[\chi^{(1)}]$ as a function of normalized Δ with two different Ω_c: (a) $\Omega_c = 0.3\Upsilon_{31}$; (b) $\Omega_c = 2\Upsilon_{31}$ [28].

1.2.3 Υ_{21} Parameter

EIT uses the coherence between two ground states for quantum interference. However, the total dephasing process would destroy the coherence between these two ground states, as shown in Fig. 1.20. The total dephasing rate Υ includes the spontaneous decay rate Γ and the dephasing rate γ from collisions among atoms, which

is the reason why the two hyperfine ground states are chosen as $|1\rangle$ and $|2\rangle$ to avoid the spontaneous decay process between them.

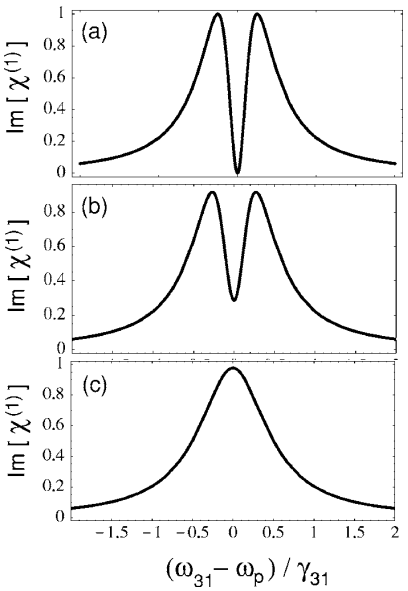

Figure 1.20: The diagrams of the absorbance $Im[\chi^{(1)}]$ as a function of normalized Δ with three different Υ_{21}: (a) $\Upsilon_{21} = 0$; (b) $\Upsilon_{21} = 0.1\Upsilon_{31}$; (c) $\Upsilon_{21} = 10\Upsilon_{31}$ [28].

1.2.4 Δ and δ Parameter

From Fig. 1.21, we can see all $Im[\chi^{(1)}]$ are 0 if the δ keeps 0, which shows the reason why the efficiency of EIT is sensitive to the two-photon detuning δ, rather than the single-photon detuning Δ.

In addition, if a large detuning of the control field Δ_c is chosen as shown in Fig. 1.22, the EIT spectrum would show a non-symmetrical behaviour [29, 30]. An advanced cooling technology called EIT cooling takes advantage of the narrow line in Fig. 1.23 to suppress the transitions of the carrier ($v \rightarrow v$, $\Delta v = 0$, where v is the quantum number of vibrational levels in the optical lattice) and the heating process ($\Delta v > 0$) [30], to obtain the similar performance as Raman sideband cooling (discussed in Chapter 3).

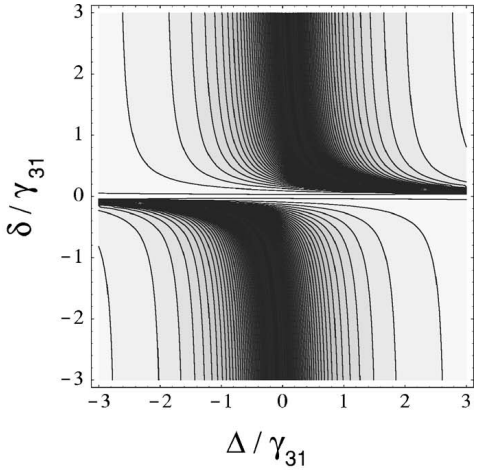

Figure 1.21: The contour plot of $Im[\chi^{(1)}]$ as a function of normalized Δ (Δ/Υ_{31}) and δ (δ/Υ_{31}), the darkness corresponds to the absolute value of $Im[\chi^{(1)}]$ [28].

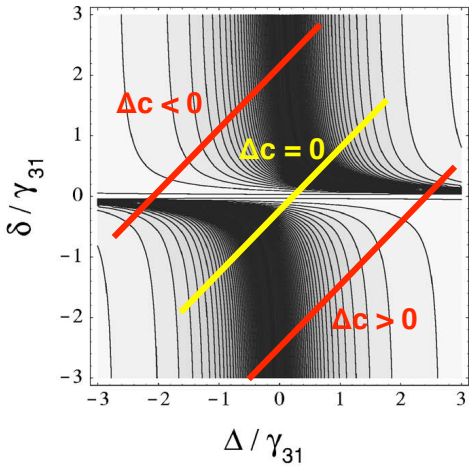

Figure 1.22: The axis of normalized Δ marked on Fig. 1.21 with different detunings of the control field Δ_c [28]; the yellow line is the case with a symmetrical spectrum like Fig. 1.18; the red lines perform two opposite non-symmetrical spectra, one of them is like Fig. 1.23

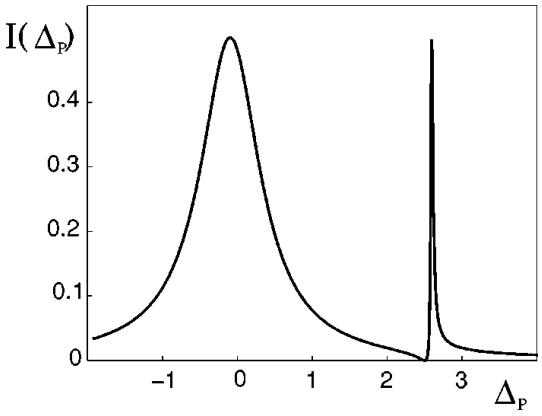

Figure 1.23: The diagrams of the absorbance $Im[\chi^{(1)}]$ as a function of normalized detuning of the probe field Δ_p (the definition of Δ_p is the same as Δ in Fig. 1.22) with a positive detuning of the control field ($\Delta_c > 0$) [30].

References

[1] US Storm Prediction Center. Doppler Radar (`https://www.spc.noaa.gov/faq/tornado/doppler.htm`).

[2] A. D. Cronin, J. Schmiedmayer, and D. E. Pritchard. Optics and Interferometry with Atoms and Molecules. *Rev. Mod. Phys.*, 81(3):1051–1129, July-September 2009.

[3] D. Schlippert, J. Hartwig, H. Albers, L. L. Richardson, C. Schubert, A. Roura, W. P. Schleich, W. Ertmer, and E. M. Rasel. Quantum Test of the Universality of Free Fall. *Phys. Rev. Lett.*, 112(20):203002, May 2014.

[4] L. Zhou, S. Long, B. Tang, X. Chen, F. Gao, W. Peng, W. Duan, J. Zhong, Z. Xiong, J. Wang, Y. Zhang, and M. Zhan. Test of Equivalence Principle at 10^{-8} Level by a Dual-species Double-diffraction Raman Atom Interferometer. *Phys. Rev. Lett.*, 115(1):013004, July 2015.

[5] R. H. Parker, C. Yu, W. Zhong, B. Estey, and H. Müller. Measurement of the Fine-structure Constant as a Test of the Standard Model. *Science*, 360(6385):191–195, April 2018.

[6] G. Rosi, F. Sorrentino, L. Cacciapuoti, M. Prevedelli, and G. M. Tino. Precision Measurement of the Newtonian Gravitational Constant using cold Atoms. *Nature*, 510(7506):518–521, June 2014.

[7] M. Kasevich, D. S. Weiss, E. Riis, K. Moler, S. Kasapi, and S. Chu. Atomic Velocity Selection Using Stimulated Raman Transitions. *Phys. Rev. Lett.*, 66(18):2297–2300, May 1991.

[8] T. Kovachy, J. M. Hogan, A. Sugarbaker, S. M. Dickerson, C. A. Donnelly, C. Overstreet, and M. A. Kasevich. Matter Wave Lensing to Picokelvin Temperatures. *Phys. Rev. Lett.*, 114(14):143004, April 2015.

[9] J. Chabé, H. Lignier, P. Szriftgiser, and J. C. Garreau. Improving Raman Velocimetry of Laser-cooled Cesium Atoms by Spin-polarization. *Optics Comm.*, 274(1):254–259, February 2007.

[10] M. B. Dahan, E. Peik, J. Reichel, Y. Castin, and C. Salomon. Bloch Oscillations of Atoms in an Optical Potential. *Phys. Rev. Lett.*, 76(24):4508–4511, June 1996.

[11] D. A. Steck. *Quantum Chaos, Transport, and Decoherence in Atom Optics*. PhD thesis, University of Texas, USA, 2001.

[12] T. W. Hansch and A. L. Schawlow. Cooling of Gases by Laser Radiation. *Optics Comm.*, 13(1):68–69, January 1975.

[13] A. Ashkin. Trapping of Atoms by Resonance Radiation Pressure. *Phys. Rev. Lett.*, 40(12):729–732, March 1978.

[14] S. Chu, L. Hollberg, J. E. Bjorkholm, A. Cable, and A. Ashkin. Three-dimensional Viscous Confinement and Cooling of Atoms by Resonance Radiation Pressure. *Phys. Rev. Lett.*, 55:48–51, 1985.

[15] K. Kowalski, V. C. Long, K. D. Xuan, M. Głódź, B. N. Huy, and J. Szonert. Magneto-optical Trap: Fundamentals and Realization. *CMST.*, SI(2):115–129, 2010.

[16] W. Phillips and H. Metcalf. Laser Deceleration of an Atomic Beam. *Phys. Rev. Lett.*, 48:596–599, 1982.

[17] M. O. Scully and M. S. Zubairy. *Quantum Optics*. Cambridge University Press, 1997.

[18] H. J. Metcalf and P. van der Straten. *Laser Cooling and Trapping*. Springer, 1999.

[19] W. D. Phillips. Laser Cooling and Trapping of Neutral Atoms. *Rev. Mod. Phys.*, 70:721–741, 1998.

[20] H. Youk. Numerical Study of Quadrupole Magnetic Traps for Neutral Atoms: Anti-Helmholtz Coils and a U-chip. *CUPJ.*, 3(2):13–18, 2005.

[21] D. A. Steck. Alkali D Line Data (`https://steck.us/alkalidata/`), April 2008.

[22] P. D. Lett, R. N. Watts, C. I. Westbrook, W. D. Phillips, P. L. Gould, and H. J. Metcalf. Observation of Atoms Laser Cooled below the Doppler Limit. *Phys. Rev. Lett.*, 61(2):169, July 1988.

[23] J. Dalibard and C. Cohen-Tannoudji. Laser Cooling below the Doppler Limit by Polarization Gradients: Simple Theoretical Models. *J. Opt. Soc. Am. B*, 6(11):2023–2045, 1989.

[24] N. B. Delone and V. P. Krainov. AC Stark Shift of Atomic Energy Levels. *Physics-Uspekhi*, 42(7):669–688, 1999.

[25] W. Petrich, M. H. Anderson, J. R. Ensher, and E. A. Cornell. Behavior of Atoms in a Compressed Magneto-optical Trap. *J. Opt. Soc. Am. B*, 11(8):1332–1335, August 1994.

[26] S. E. Harris, J. E. Field, and A. Imamoğlu. Nonlinear Optical Processes using Electromagnetically Induced Transparency. *Phys. Rev. Lett.*, 64:1107, 1990.

[27] C. J. Foot. *Atomic Physics*. Oxford, 2005.

[28] M. Fleischhauer, A. Imamoglu, and J. P. Marangos. Electromagnetically Induced Transparency: Optics in Coherent Media. *Rev. Mod. Phys.*, 77(2):633–673, 2005.

[29] G. Morigi, J. Eschner, and C. H. Keitel. Ground State Laser Cooling Using Electromagnetically Induced Transparency. *Phys. Rev. Lett.*, 85(21):4458–4461, November 2000.

[30] G. Morigi. Cooling Atomic Motion with Quantum Interference. *Phys. Rev. A*, 67:03342, March 2003.

Chapter 2

Motion Sensing with a Collective State Atoms

Currently, atom-based motion sensors rely on measuring the first-order Doppler shift of the atomic transition for single-particles. By using Doppler-sensitive detection methods, e.g. two-photon Raman transition [1, 2], the Doppler distribution can be mapped out, and then use the distribution to determine the center-of-mass velocity of an atomic ensemble. The two-photon Raman transition detects the atomic state destructively, so for each data point, the cold atoms have to be reloaded, which takes a long time and increases the concern of the system stability. To improve this tedious procedure, instead of detecting atoms directly, we would like to measure the center-of-mass motion of an atomic ensemble by the phase shift measurement of light passing through the moving medium. This method is an application of light dragging effect, which offers us an opportunity to acquire the motional behaviour averaging the whole atomic ensemble with single-shot measurement.

As one of the most influential experiments on the development of modern macroscopic theory from Newtonian mechanics to Einstein's special theory of relativity, the phenomenon of light dragging in a moving medium has been discussed and observed extensively in different types of systems. To have a significant dragging effect, the long duration of light travelling in the medium is preferred. In 2012, Davuluri *et al.* published their theoretical work [3] about the connection between light dragging effect and slow light in a hot vapour cell. In our case, we experimentally demonstrated the light dragging effect with EIT enhancement in cold atoms, all details had been published (see Reference [4]). Here we demonstrate a light-dragging ex-

periment in an electromagnetically induced transparent cold atomic ensemble and enhance the dragging effect by at least three orders of magnitude compared with the previous experiments. With a large enhancement of the dragging effect, we realise an atom-based velocimeter that has a sensitivity two orders of magnitude higher than the velocity width of the atomic medium used. Such a demonstration could pave the way for motion sensing using the collective state of atoms in a room temperature vapour cell or solid state material.

2.1 Light Dragging Effect and EIT Enhancement

The light dragging effect was discovered by H. Fizeau in 1851 before the Einstein's special theory of relativity [5, 6]. Figure 2.1 shows a schematic of Fizeau's water flowing experiment [7]. Light was separated into two beams and passed the flowing water tube in a counter-propagating direction. The phase shift of the interferometer formed by the counter-propagating light after passing through the water was observed. However, because the optical paths of these two beams are identical, the observed phase shift cannot be well-explained at that time.

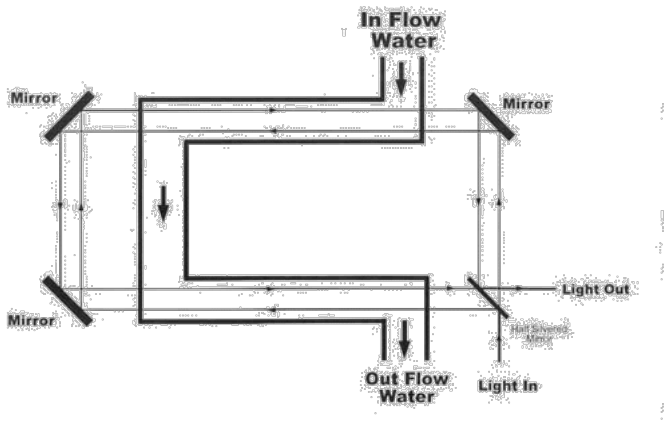

Figure 2.1: The setup of Fizeau's water flowing experiment in 1851 [7].

After a few decades, H. A. Lorentz took advantage of Einstein's special relativity and introduced a dragging coefficient F_d to describe changes of the phase velocity v_p of the light in the moving medium with the velocity v and the refractive index n [8] shown in Eqs. 2.1 and 2.2:

$$v_p = c + F_d v \tag{2.1}$$

$$F_d = 1 - \frac{1}{n^2} + \frac{\omega}{n}\frac{\partial n(\omega)}{\partial \omega}, \tag{2.2}$$

where ω is the angular frequency of the light. Equation 2.2 shows the reason why the dragging coefficient F_d is usually very small because the refractive indexes n of most matters are close to 1, and the dispersions $\partial n(\omega)/\partial\omega$ are insignificant.

Light dragging effect is difficult to be detected due to the small F_d in most cases. From Eq. 2.2, an obvious method to increase F_d is to engineer a high dispersion within a spectral range of the probe field. Unfortunately, under most of the conditions, the frequency range with the highest dispersion happens when the absorption is largest. To overcome the difficulty mentioned above and enhance the sensitivity of the measurement based on the light dragging effect simultaneously, EIT scheme was implemented in our system. As mentioned in Section 1.2, EIT can artificially open up a transparent window for the probe field and create a high-dispersion region as shown in Fig. 1.18. The spectral width of EIT is fully tunable by the intensity of the control field, which means F_d can be controlled to fit the experimental requirement.

To calculate the phase shift of light in the dragging effect, we considered the group velocity of a wave-packet and used Taylor's expansion to obtain the mathematical form of the group velocity v_g as Eq. 2.4 shows (ignore group velocity dispersion and higher order terms). The relation between the velocity v of the moving medium and the phase shift $\Delta\varphi$ through a medium of length L can, therefore, be derived as shown in Eq. 2.6 (assume $n \approx 1$):

$$F_d \approx \omega(\frac{\partial n}{\partial \omega}) \tag{2.3}$$

$$v_g = \frac{c}{n + \omega(\frac{\partial n(\omega)}{\partial \omega})} \approx \frac{c}{\omega(\frac{\partial n(\omega)}{\partial \omega})} \tag{2.4}$$

$$v_p = c(1 + \frac{v}{v_g}) \tag{2.5}$$

$$\varphi = kL = \frac{\omega}{v_p}L \approx \frac{\omega L}{c}(1 - \frac{v}{v_g}) \Rightarrow \Delta\varphi = -\frac{\omega}{c}t_g v = -\frac{kL}{c}F_d v. \tag{2.6}$$

In Eq. 2.6, $t_g = L/v_g$ is the group delay of the light passing the medium. Because of the benefit of EIT scheme, t_g can be a few μs long in our experiment,

which increases dramatically, compared with other normal media. The velocity v of the moving medium (it is the cold atomic ensemble in our experiment) can then be obtained given that ω and c are both known quantities.

2.2 Experimental Setup

Motion sensing using the light dragging effect is the first experimental project demonstrated in our optical system. In this section, the atomic configuration, the optical setup and the experimental timing sequence for the motion sensing project will be introduced. The atomic transitions of the preprocessing laser cooling step are also included, whose optical setup and timing sequence are discussed in Section 1.1.4.

2.2.1 Atomic Configuration

In this experiment, ^{85}Rb atom was chosen as the EIT medium, because there are several advantages. First of all, the dipole transition wavelength of ^{85}Rb is visible / near infrared (IR) light, which provides us more choices of laser sources; Secondly, the splittings of energy levels in ^{85}Rb hyperfine structure are easy to set up for the lasers in our equipments. Finally, the atomic mass M of ^{85}Rb is relatively heavier than most of popular atoms like H, Li, Na and so on. Heavier atoms have slower recoil velocity ($v_{\text{recoil}} = \hbar k/M$) and slower thermal velocity ($v_{\text{thermal}} = \sqrt{3k_BT/M}$), which could be more efficient in the cooling processes.

There were many laser fields with different frequencies in this experiment, as shown in Fig. 2.2. They can be classified into three parts by the different usages:

1. The cooling field: $|F = 3\rangle \rightarrow |F' = 4\rangle$ (15 MHz red-detuned and circularly polarized). The cooling field was used to decelerate the moving hot atoms by adding momentum kicks in the opposite direction. To maximize the scattering efficiency and avoid heating effects caused by this cooling field, its frequency needs to be red-detuned due to Doppler effect (see Section 1.1.1). Additionally, it is better to choose a cyclic transition as the cooling field, because the absorbed electrons could relax back to their initial states only, which makes the cooling process able to run continuously. Also, the scattering rate should be as high as possible. The circularly polarized field is able to pump the population to the spin-polarized states, which fits the bill.

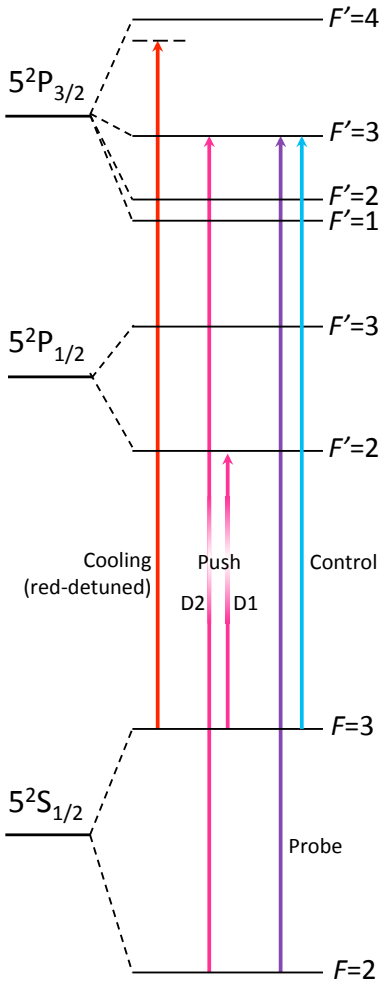

Figure 2.2: ^{85}Rb hyperfine structure and the relative transitions used in the experiment. The red arrow is the cooling field with 20 MHz red-detuned from D2 $|F = 3\rangle \rightarrow |F' = 4\rangle$ transition. The two magenta arrows (D2 $|F = 2\rangle \rightarrow |F' = 3\rangle$ and D1 $|F = 3\rangle \rightarrow |F' = 2\rangle$) are the push fields to accelerate atoms by the momentum kicks. The purple (D2 $|F = 2\rangle \rightarrow |F' = 3\rangle$)and skyblue (D2 $|F = 3\rangle \rightarrow |F' = 3\rangle$) arrows are the probe and control field, respectively, for phase shift measurements.

2. The push field: there were two push fields (D2 $|F = 2\rangle \rightarrow |F' = 3\rangle$ and D1 $|F = 3\rangle \rightarrow |F' = 2\rangle$), both of which were versatile in this experiment. The function of the push fields is to provide the momentum kicks by the resonant scattering to push the atomic cloud upward or downward and control its average velocity. In addition, both of these two push fields were separated into two parts, one was (a) in Fig. 2.3, which was a directional laser field for the pushing task; the other was (b) in Fig. 2.3, which co-propagated with the cooling field for the repump of the cooling process (D2 push field) and the fluorescence imaging process (D1 and D2 push field), as shown in the right-hand side of Fig. 2.3. D2 push field was also used as a repump field for the cooling process, to prevent some part of the population from transferring to $|F = 2\rangle$ due to the off-resonant transition $|F = 3\rangle \rightarrow |F' = 3\rangle$ caused by the red-detuned cooling field. D1 and D2 push fields were also the excitation fields for the fluorescence imaging of the atomic ensemble. We used a CCD camera to measure the shape and position of the atomic ensemble from the fluorescence of atoms by absorbing D1 and D2 push fields.

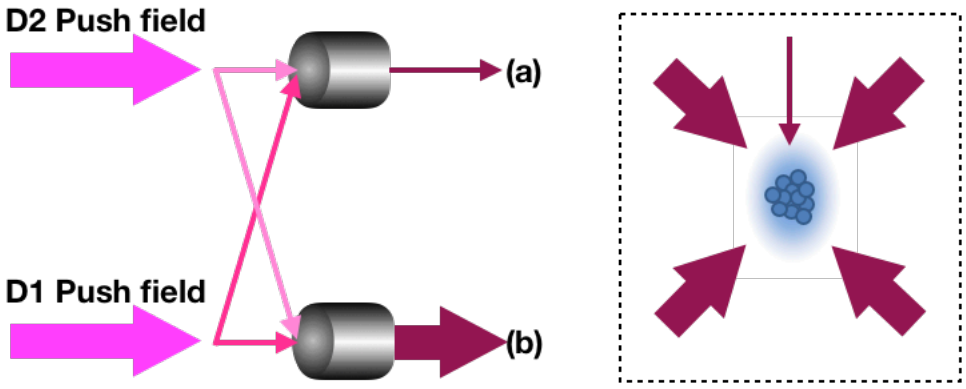

Figure 2.3: D1 and D2 push fields are separated into two parts and then coupled into different optical fibres: (a) a directional laser field to provide momentum kicks for the pushing task; (b) a sixfold laser field, which co-propagates with the cooling field, working as the repump field of the cooling process or the excitation field for the fluorescence imaging of the atomic ensemble.

3. The probe field D2 $|F = 2\rangle \rightarrow |F' = 3\rangle$ and the control field D2 $|F = 3\rangle \rightarrow |F' = 3\rangle$ were used for EIT scheme (see Fig. 1.17), and their frequencies could be turned by an acoustic-optical modulator (AOM) and an electric-optical modulator

(EOM) for different single-photon detuning Δ and two-photon detuning δ (see Fig. 1.17).

2.2.2 Optical Setup

The main optical setup is shown in Fig. 2.4. For the push fields, we coupled both push fields together and set a stable magnetic indexing mount (NX1N - 16-Position Indexing Mount from ThorLabs, Inc.) to direct the optical path upward or downward. In addition, the velocity of the atomic ensemble is tuned by the intensity of the push fields.

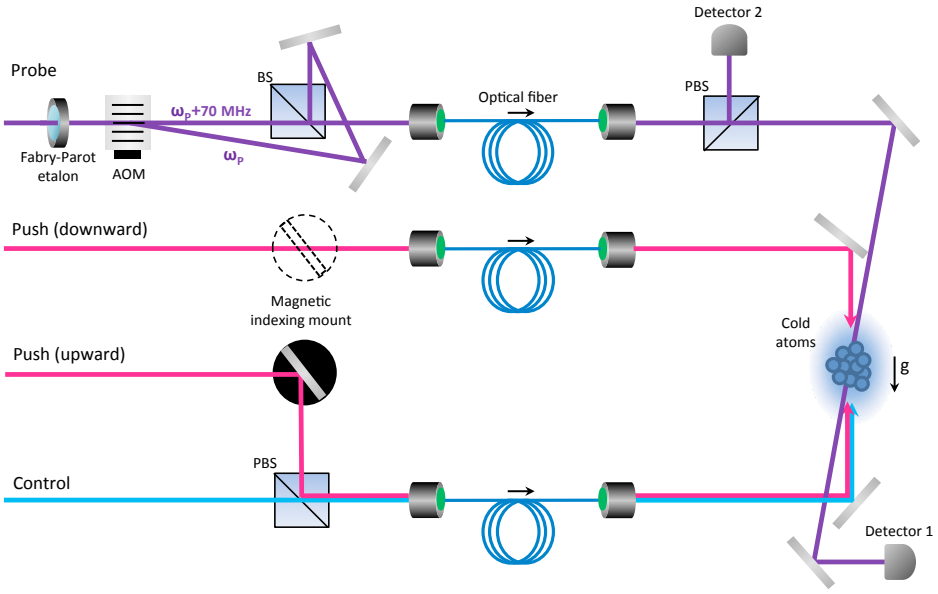

Figure 2.4: The primary optical setup in the motion sensing experiment.

In order to gain the sensitivity, we aligned the probe field and the control field in the counter-propagating direction ($\measuredangle 183°$ between two light beams), as the phase shift $\Delta\varphi$ of the light dragging was proportional to the effective wavevector $\mathbf{k}_s$ ($\mathbf{k}_s = \mathbf{k}_p - \mathbf{k}_c \approx 2\mathbf{k}_p$) atoms experience [9]. The power of the probe field was set about 1 μW, much weaker than that of the control fields, which are about 600 μW and 2000 μW. The two beams were overlapped on the atomic cloud of about 1.4 mm in length in the optical fields' direction. The control beam was collimated with a waist of about 4 mm and the probe beam was slightly focusing at the center of the atomic cloud with a waist of about 0.5 mm (shown in Fig. 2.5). The intensity ratio of the

control and probe fields is about 10 : 1.

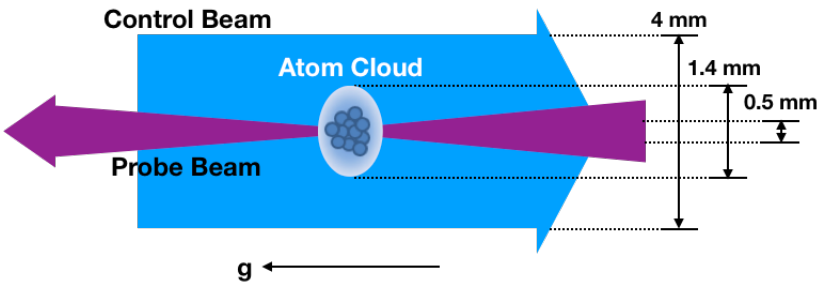

Figure 2.5: The size comparison of the control field, the probe field, and the atomic cloud.

The control field was generated from a diode laser, and part of the power was sent through an electro-optical modulator (EOM). The first sideband after the modulator passed through a solid Fabry-Pérot cavity followed by a 70 MHz acoustic-optical modulator (AOM). The field coming out of lower first order served as the probe field, and the zero order served as an auxiliary field which then combined with the probe field by a non-polarising beam splitter to form a 70 MHz beating signal. This 70 MHz signal was further split: part of the beam was sent through the atomic ensemble for the light-dragging experiment, and the other half served as a local oscillator for phase comparison as shown in Fig. 2.4. Since the auxiliary field was 70 MHz detuned from the probe field, it did not experience the large light-dragging effect as the probe field, therefore, the phase shift of the 70MHz signal resulted from the phase velocity dragging of the probe field only.

The detectors are APD with 1 μW saturation power (APD120A/M - Si Avalanche Photodetector, 400 - 1000 nm from ThorLabs, Inc.), and the calculation method of phase differences is introduced in Section 4.3.2. Moreover, the phase noise from the vibration of optical elements is able to be greatly reduced, because the sub-millimetre fluctuation of the optical path is negligible compared to the wavelength of 70 MHz beating signal.

The solid Fabry-Pérot cavity is based on the interference concept as the frequency filtering mechanism. For our central wavelength of the light field of 780 nm and the thickness of the etalon of 7 mm, the free spectral range (FSR) is about 14 GHz. Transmission linewidth is 0.6 GHz, the extinction ratio is about 23.6 and

the finesse (F) is about 23. However, the etalon is sensitive to the perturbation from surroundings, such as temperature, which will cause a shift of the resonance condition. We mounted the cavity with a thermoelectric cooler (TEC) to stabilise the temperature.

For pulsing the probe field, the radio frequency fed into the AOM was amplitude-modulated by a Guassian pulse with FWHM of 5 μs from an arbitrary function generator. EOM (Phase Modulator from EOspace, Inc.) was used to fine-tune the frequency of the probe field and scan the EIT spectra.

2.2.3 Timing Sequence

The timing sequence for the experiment is shown in Fig. 2.6. Initially, we cooled the atoms close to 40 μK in a magnetic-optical trap. The upward or downward push fields with 0.7 ms duration were then sent to the atoms after 5 ms. The EIT pulses were applied to the atoms after the pushing process. The control field was introduced 0.5 ms earlier for optical pumping to prepare all the population in the ground state $|F = 2\rangle$.

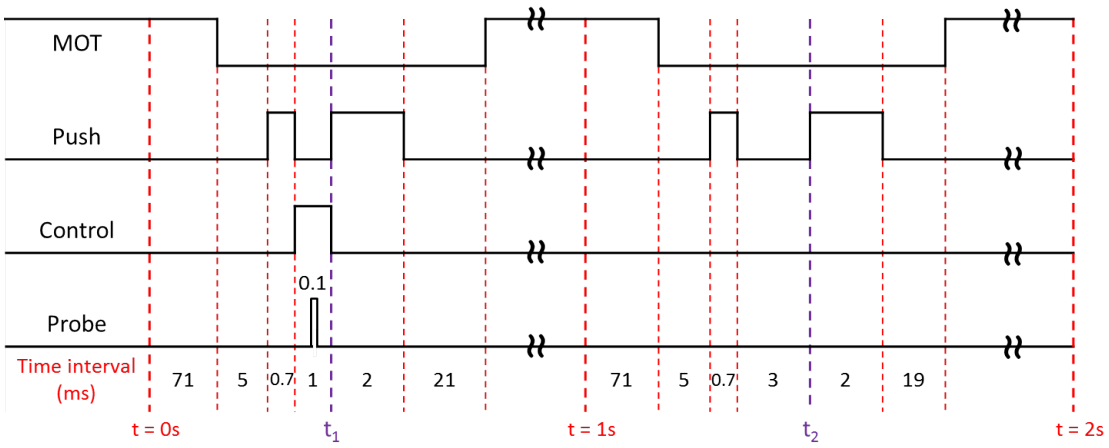

Figure 2.6: The time sequences of the motion sensing experiment.

The velocity of the atomic ensemble was calculated by measuring the positions of the atomic ensemble on a CCD camera at two different timing t_1 and t_2 separated by 2 ms (see Eq. 2.7). The CCD camera received the fluorescence from the atoms excited by the push fields. We also measured the temperature of atomic ensemble

using time-of-flight (TOF) method by comparing the widths of the atomic cloud at two different flight time (t_1 and t_2, they are 1 ms and 3 ms in our experiment) to calculate the temperature (see Eq. 2.8).

$$v_{\text{average}} = \frac{position(t_2) - position(t_1)}{t_2 - t_1} \tag{2.7}$$

$$T_{x,y,z} = \frac{M}{k_B} \frac{width(t_2)^2 - width(t_1)^2}{t_2^2 - t_1^2}. \tag{2.8}$$

In Eq. 2.8, $T_{x,y,z}$ is the temperature of one of x, y and z axes; M is the mass of single ^{85}Rb atom; k_B is Boltzmann constant ($\approx 1.38 \times 10^{-23} m^2 s^{-2} kg K^{-1}$). The method of temperature measurement and calculation are based on the application of Ballistic expansion of thermal atoms, as discussed in References [10, 11].

2.3 Data and Discussion

2.3.1 EIT Spectra

Figure 2.7 shows the transmission T of the probe pulse as a function of the probe field detuning while the control field detuning is fixed (equal to two photon detuning δ). The results fit the theoretical model of Eqs. 2.9 and 2.10 [12] (In Eq 2.9, k_0 is the wavevector of the probe field in the vacuum; n is the number density of atoms; σ_{abs} is the cross-section of one atom in ensemble average; ρ_{31} is the density matrix element between the ground state and the excited state ($|1\rangle$ and $|3\rangle$), the same as the definition in Eq. 1.35; Γ (Γ_{31}) is the spontaneous decay rate; Ω_p is the Rabi frequency of the probe field; OD is the optical depth), which integrate the effects from all hyperfine levels of $5^2P_{3/2}$. Referring to the parameters of the first order electric susceptibility $Im[\chi^1]$ in Eq. 1.35), the obtained result was OD 36.0(4), the control field Rabi frequency Ω_c was 0.582(5)Γ, and the ground state coherence Υ_{21} was 0.0031(1)Γ (Γ is about 6 MHz), so the high coherence between ground states ($|1\rangle$ and $|2\rangle$) was achieved.

$$T = exp(-\frac{1}{2}k_0 L \cdot Im[\chi^{(1)}]) = exp(-\frac{1}{2}n\sigma_{abs}L)$$
$$= exp(-\frac{1}{2}n\frac{3\lambda^2}{2\pi}Im[\frac{\rho_{31}\Gamma}{\Omega_p}] \cdot L)$$
$$= exp(-OD \cdot \frac{\Gamma}{2} \cdot Im[\frac{\rho_{31}}{\Omega_p}]) \quad (2.9)$$
$$OD = \frac{3\lambda^2}{2\pi}nL. \quad (2.10)$$

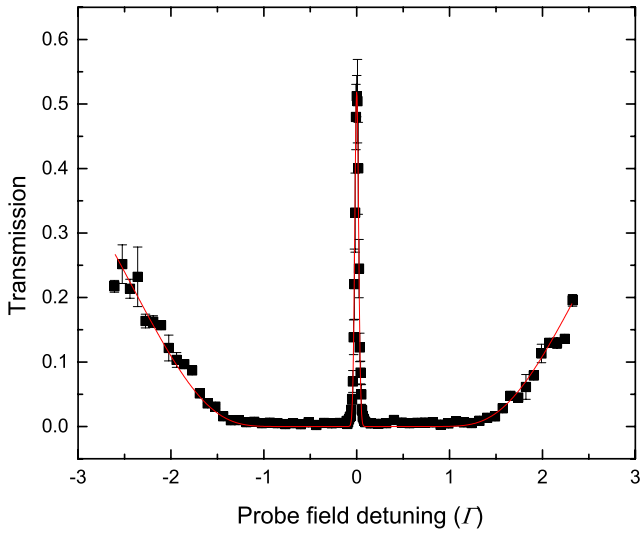

Figure 2.7: The transmission spectrum as a function of the probe field detuning in the unit of excited state relaxation rate Γ of ^{85}Rb.

In Fig. 2.8, the EIT spectrum is measured with two different control field powers. Our results fit these data with a Lorentzian function and obtained the peak widths of 0.306(6)Γ and 0.134(1)Γ for 2 and 0.6 mW of the control field power, respectively. From Fig. 1.19 and Eq. 2.11 [12], the width of the EIT transmission peak ($\Delta\omega_{\text{trans}}$) is directly proportional to the square of the Rabi frequency (proportional to the intensity) of the control field (Ω_c), and inversely proportional to the square root of OD (under the assumption of the dephasing rate $\Upsilon_{21} \approx 0$, see its definition in Eqs. 1.34 and 1.35). Our experimental results matched the theoretical equations, and we can see that if we tend to increase the light dragging effect without sacrificing

the probe intensity, the OD has to be increased to compensate the decrease of the dispersion (inversely proportional to $\Delta\omega_{\text{trans}}$).

$$\Delta\omega_{\text{trans}} = \frac{\Omega_c^2}{\Gamma\sqrt{OD}}. \tag{2.11}$$

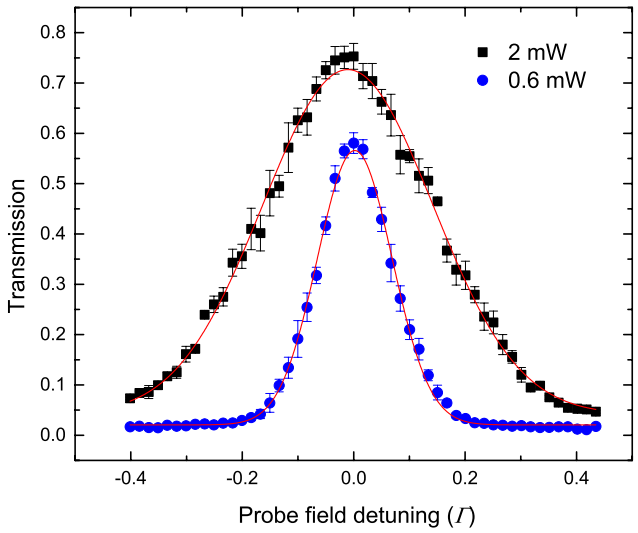

Figure 2.8: The transmission spectrum as a function of the probe field detuning. Black squares and blue circles show the spectra with 2 and 0.6 mW of the control field power, respectively.

2.3.2 Velocity Sensing by Enhanced Light Dragging Effect

In this experiment, we hope to build an optical system to sense infinitesimal velocity change by measuring and amplifying phase shifts of the signal light passing through the moving medium. We built a cooling system to produce cold atoms, and then made the whole atomic ensemble move in either positive or negative z-direction by momentum kicks from push fields. Also, we measured the phase differences between the data acquired in Detector 1 and Detector 2 (see Fig. 2.4).

The velocity of the atomic ensemble was controlled by the push field power, which was correlated to the input power of their AOM switches. The power control of AOM switches was set in the analogue setting of the experimental time sequence,

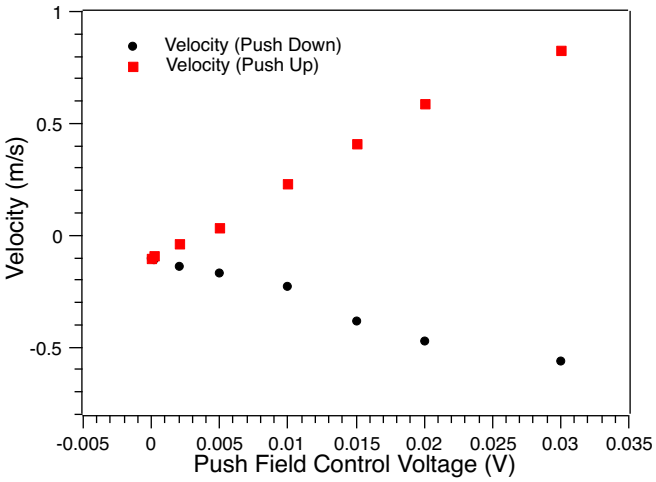

Figure 2.9: The velocity of the atomic ensemble as a function of the push field power controlled by the AOM amplitude control voltage with different directions.

so the voltage (power) output was consistent and repeatable. In Fig. 2.9, we can see the velocity of the ensemble was almost linearly increasing with the voltage change of the push field. There was one point worth noticing: the velocity at the zero voltage point was a negative value, because the gravity needed to be taken in account. In addition, one of push fields (D1) connected with a digital setting port, not controlled by analogue setting, which meant its power cannot be fine-tuned. As a result, the slope of velocity in push-up and push-down cases did not look symmetric in Fig. 2.9.

In Fig. 2.10, the delay time in the y-axis is proportional to the phase shift $\Delta\varphi$, where $2\pi\times$ delay time = phase shift $\times$ period of 70 MHz beating (14.28 ns). From these two spectra, we can find the near-linearity of the relation between the ensemble velocity and the delay time (phase shift), where the little deviations come from the fluctuation in the group time delay t_g (see Eq. 2.6). The slopes of data line in the above two cases are very different, which show the trade-off of EIT properties. Based on Eq. 2.6, the slope is proportional to the dispersion $(\partial n/\partial\omega)$, and the EIT spectral width is proportional to the power of the control field (see Eq. 2.11), so the slope becomes smaller when the power of the control field is higher. In our experimental result, the spectrum with 0.6 mW of the control field power has a larger slope than that with 2 mW of the control field power, so it performs a better velocity-sensing. However, if the power of the control field is too low, the probe will be absorbed due

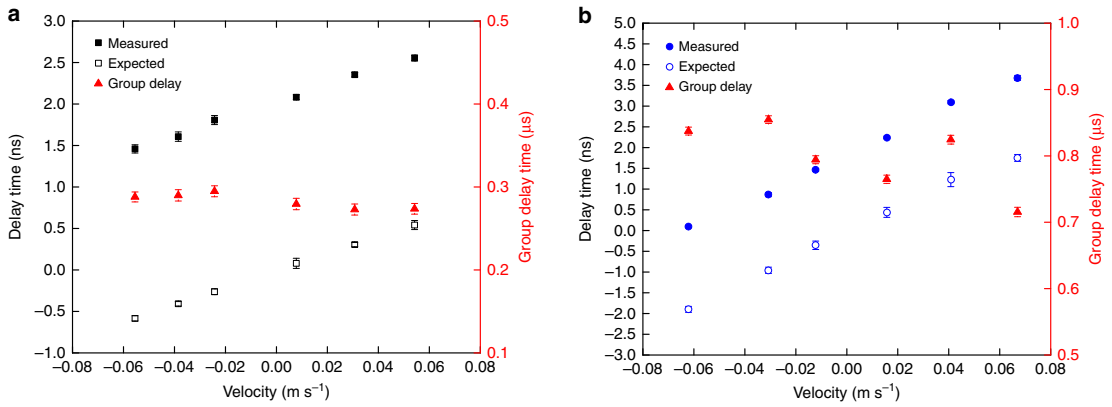

Figure 2.10: The phase delay time as a function of the atomic ensemble velocity. (a) With control field power of 2 mW. The black solid squares and the black open squares are the measured phases and the expected phases (left axis), respectively, which refer to Eq. 2.6 and group delay measurements. (b) With control power of 0.6 mW. The blue solid circles and the blue open circles are the measured phases and the expected phases (left axis), respectively, which refer to Eq. 2.6 and group delay measurements. The red solid triangles are the group delay times (right axis). The phase delay are measured in terms of the delay time. One cycle corresponds to 1/70 MHz = 14.29 ns. The measured phase uncertainty is by taking the standard error of three cycles of 70 MHz sinusoidal wave in the probe field envelope and averaging for 20 experimental cycles. Each experimental cycle takes 2 s. The group delay of the probe field is measured at each velocity by fitting the center of the probe field pulse with a Gaussian function.

to decoherence (see the EIT mechanism in Fig. 1.16), and the working range of the ensemble velocity becomes very small. For example, in our complete data plots in Fig. 2.11, some data points on the left-hand side had a larger deviation from a theoretical linear line. This was because those data points were outside of the range of the EIT width in 0.6 mW case. This deviation was not observed in 2.0 mW case because it had a larger EIT linewidth.

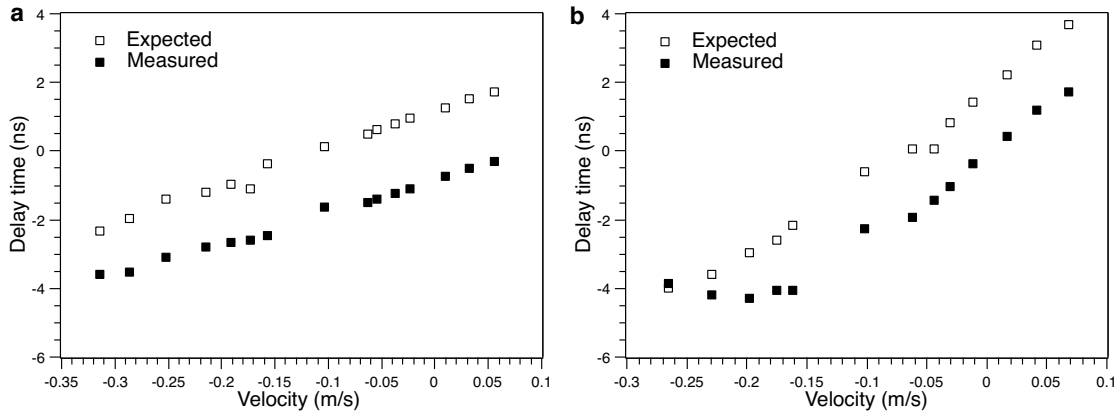

Figure 2.11: The phase delay time as a function of the atomic ensemble velocity in full range of our experiment. The filled squares and the hollow squares are experimental values and calculated values by Eq. 2.6, respectively. (a) With control field power of 2.0 mW; (b) With control field power of 0.6 mW.

There are some offsets between the measured delay time and the calculated ones. We managed to reduce the control field power gradually, and found it would disappear at some threshold value of the control field power, which meant that it came from the EIT process. Now we focus on the velocity range near 0 m/s, and offset to experimental data, the perfect matching between experimental and theoretical values was obtained as Fig. 2.12 shows.

With the measured atomic cloud size 1.4 mm and our largest group delay time t_g 855 ns, the dragging coefficient F_d in our experiment had reached 1.83×10^5, which was two orders of magnitude larger than that with hot ^{85}Rb vapor [13] and five orders of magnitude larger than the original light dragging effect [5, 6], because of the benefit from EIT enhancement. For the velocity sensing, our experimental setup can perform a stable data acquisition and statistical calculations, so the error bars are

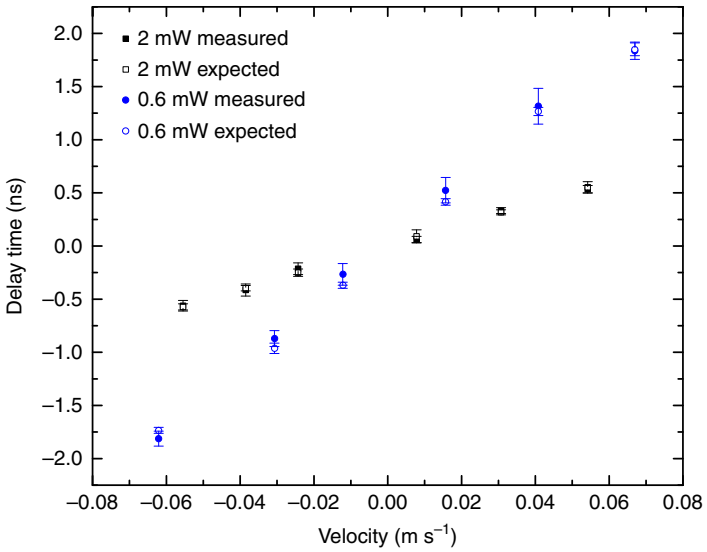

Figure 2.12: The phase delay times in Fig. 2.10 offset to zero at zero velocity. The solid circles (0.6 mW control field power) and squares (2 mW control field power) are the measured delayed phases and the open circles (0.6 mW control field power) and squares (2 mW control field power) are the expected delayed phases in Eq. 2.6 and group delay measurements.

insignificant on the data plots. In our experiment, we took advantage of heterodyne setup to reduce the phase uncertainty, which was about 0.01 rad averaging for 20 experimental data points in a 2 s acquisition cycle. The uncertainty of the ensemble velocity $\Delta v = 0.01/k_s/t_g = 1$ mm/s was $v_R/6$ (v_R is the recoil velocity) and two orders of magnitude smaller than thermal velocity uncertainty (Doppler broadening, about 100 mm/s) of the atomic ensemble.

References

[1] K. Moler, D. S.Weiss, M. Kasevich, and S. Chu. Theoretical Analysis of Velocity-selective Raman Transitions. *Phys. Rev. A*, 45(1):342–348, January 1992.

[2] J. Chabé, H. Lignier, P. Szriftgiser, and J. C. Garreau. Improving Raman Velocimetry of Laser-cooled Cesium Atoms by Spin-polarization. *Optics Comm.*, 274(1):254–259, February 2007.

[3] S. Davuluri and Y. V. Rostovtsev. Controllable Enhanced Dragging of Light in Ultradispersive Media. *Phys. Rev. A*, 86:013806, 2012.

[4] P.-C. Kuan, C. Huang, W. S. Chan, S. Kosen, and S.-Y. Lan. Large Fizeau's Light-dragging Effect in a Moving Electromagnetically Induced Transparent Medium. *Nature Comm.*, 7:13030, October 2016.

[5] H. Fizeau. Sur les Hypothèses Relatives à l'éther Lumineux. *C. R. Acad. Sci.*, 33:349–355, 1851.

[6] H. Fizeau. The Hypotheses Relating to the Luminous Aether, and an Experiment which Appears to Demonstrate that the Motion of Bodies Alters the Velocity with which Light Propagates itself in their Interior. *Philosophical Magazine*, 2:568–573, 1851.

[7] D. Wortzman. The Atom Universe Model: A Work In Progress (`http://gyroverse.com/document-sep2000.htm`), September 1999.

[8] H. A. Lorentz. Electromagnetic Phenomena in a System Moving with Any Velocity Less than that of Light. *Proc. K. Ned. Akad. Wet.*, 6:809–831, 1904.

[9] M. Fleischhauer and M. D. Lukin. Dark-state Polaritons in Electromagnetically Induced Transparency. *Phys. Rev. Lett.*, 84(22):5094–5097, 2000.

[10] L. You and M. Holland. Ballistic Expansion of Trapped Thermal Atoms. *Phys. Rev. A*, 53(1):R1–R4, January 1996.

[11] T. M. Brzozowski, M. Maczynska, M. Zawada, J. Zachorowski, and W. Gawlik. Time-of-flight Measurement of the Temperature of Cold Atoms for Short Trap–Probe Beam Distances. *J. Opt. B: Quantum Semiclass. Opt.*, 4:62–66, January 2002.

[12] M. Fleischhauer, A. Imamoglu, and J. P. Marangos. Electromagnetically Induced Transparency: Optics in Coherent Media. *Rev. Mod. Phys.*, 77(2):633–673, 2005.

[13] A. Safari, I. D. Leon, M. Mirhosseini, O. S. Magaña-Loaiza, and R. W. Boyd. Light-drag Enhancement by a Highly Dispersive Rubidium Vapor. *Phys. Rev. Lett.*, 116:013601, 2016.

Chapter 3

Raman Sideband Cooling

In Chapter 2, an application of EIT on the light dragging effect of a moving medium in a free space was introduced. After the demonstration in a free space, we tend to apply this technique to the moving atoms in a driven periodic potential. In particular, we plan to observe the periodic motion of atoms undergoing Bloch oscillation in a moving optical lattice. However, to observe the coherent motion of atoms in a driven optical lattice, atoms need to be loaded into the optical lattice sites and dragged by that moving lattice. The efficiencies of the loading and dragging process strongly depend on the temperature of the atomic ensemble. To maximize it, the atoms need to be cooled down to the recoil temperature of D1 or D2 transitions.

To approach the recoil temperature of atoms for our further experiments, an advanced cooling technique is necessary. However, many cooling techniques achieve a lower temperature accompanied with high loss of atoms, such as Raman cooling (velocity selection) [1–3] and evaporative cooling [4, 5]. Here, we apply Raman sideband cooling technique in our system, which can both keep a large fraction of atoms and closely reach the recoil temperature. Raman sideband cooling was first demonstrated with ions [6]. In neutral atoms, Raman sideband cooling has been demonstrated with ^{6}Li [7], ^{39}K [8], ^{87}Rb [9–11], and ^{133}Cs [12–16]. Different experimental arrangements are required for different fine and hyperfine structures of atomic species. ^{85}Rb atoms get a great interest in atomic physics due to their high natural abundance in Rb isotopes and opposite sign of scattering length of their hyperfine ground states [17]. On the other hand, the small energy separation of the hyperfine states and large collision loss make ^{85}Rb less popular than ^{87}Rb in the community. In our experiment, we demonstrated the degenerate Raman sideband

cooling of ^{85}Rb atoms in a 2D lattice, and achieve 60% number of atoms remaining in our cold atomic ensemble with a cooling temperature 400 nK close to the recoil temperature 357 nK of ^{85}Rb D1 line transition [18].

3.1 Theory

Raman sideband cooling is one of ground-state cooling techniques, whose mechanism is based on loading atoms into a harmonic potential well, and then transfer the population of atoms to the vibrational ground state of the harmonic potential to achieve a lower temperature. The quantized energy levels in the external potential well are the core of the ground-state cooling technique. In our experiment, they are provided by the optical lattice, whose properties are introduced in Section 3.1.1. With the foundation built from the optical lattice, the detail of the cooling mechanism is introduced in Section 3.1.2.

3.1.1 Optical Lattice

A key role in Raman sideband cooling is the optical lattice. Simply speaking, an optical lattice is the potential well produced by the standing wave of coherent laser fields. Here a 1D lattice / standing wave is used as an example:

$$\begin{aligned} E_{\text{forward}} &= A \cdot \cos(k_z z - \omega t) \\ E_{\text{backward}} &= A \cdot \cos(k_z z + \omega t) \\ E_{\text{total}} &= E_{\text{forward}} + E_{\text{backward}} = 2A \cdot \cos(k_z z)\cos(\omega t), \end{aligned} \tag{3.1}$$

where k_z is the wave vector on the propagation direction z-axis; A is the amplitude of the light field; ω is oscillation frequency. We can see that the electric field E_{total} of the standing wave periodically distributes and oscillates in the free space. Atoms are trapped within the wavelength size potential through AC Stark shift.

AC Stark effect (shift), or light shift, describes how an atom responds to a light field (AC electromagnetic filed), which is shown in Fig. 3.1. The same as EIT effect in Section 1.2, there are two pictures for understanding this behaviour: the dressed atom picture and the bare atom picture. Figure 3.2 shows the mechanism of AC Stark effect in the dressed atom picture [19]. Ω is the Rabi frequency of the

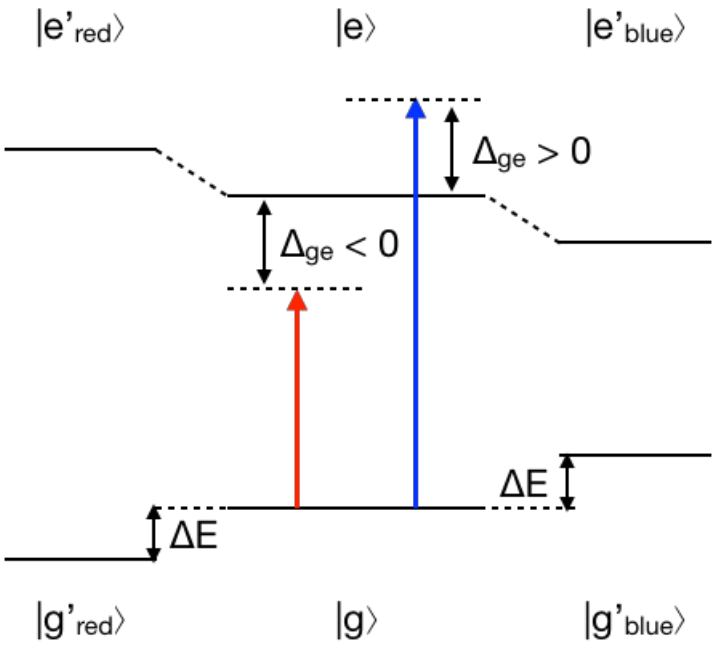

Figure 3.1: Far-detuned light field with detuning Δ_{ge} causes AC Stark effect, which makes the energy level shifts ΔE based on the magnitude and sign of the detuning. $|g\rangle$ and $|e\rangle$ represent the ground state and the excited state in a two-level system.

interaction between the incident light and the atom, and the definitions of $|g\rangle$ and $|e\rangle$ are the same as those in Fig. 3.1; $|a(N)\rangle$ and $|b(N)\rangle$ are similar to those in Eqs. 1.29 and 1.30, with an extra detuning Δ_{ge} as follows:

$$|a(N)\rangle = sin\theta|g, N+1\rangle + cos\theta|e, N\rangle \tag{3.2}$$

$$E_{|a(N)\rangle} = \frac{\hbar}{2}(\Delta_{ge} + \sqrt{\Delta_{ge}^2 + \Omega^2}) \tag{3.3}$$

$$|b(N)\rangle = cos\theta|g, N+1\rangle - sin\theta|e, N\rangle \tag{3.4}$$

$$E_{|b(N)\rangle} = \frac{\hbar}{2}(\Delta_{ge} - \sqrt{\Delta_{ge}^2 + \Omega^2}) \tag{3.5}$$

$$\theta = \frac{1}{2}tan^{-1}(-\frac{\Omega}{\Delta_{ge}}), \quad 0 \leq \theta \leq \frac{\pi}{2}. \tag{3.6}$$

In the case of the far-detuned light field ($|\Delta_{ge}| \gg \Omega$), and $\Delta_{ge} > 0$ as shown in Fig. 3.2, the configuration and the energy of $|a(N)\rangle$ and $|b(N)\rangle$ are approximated as:

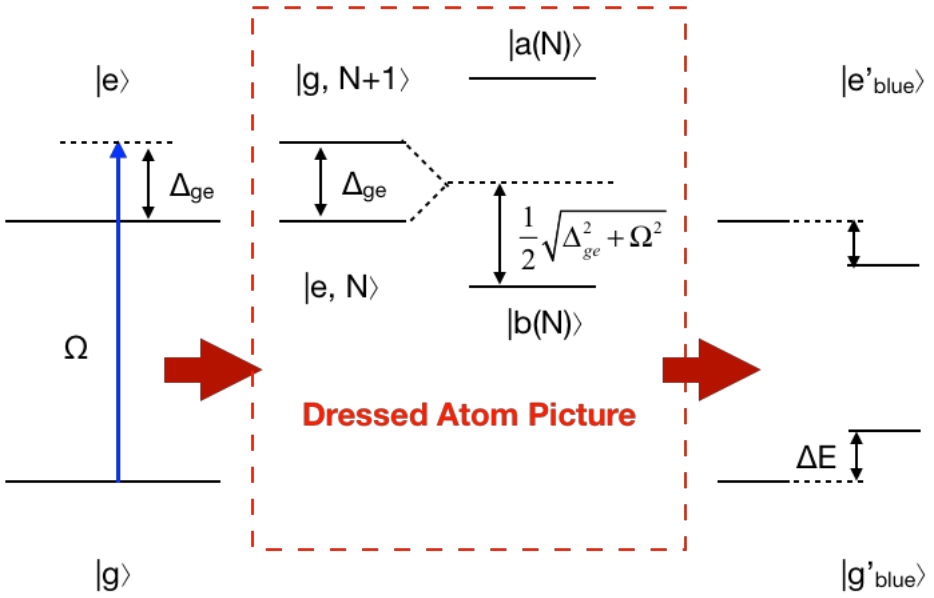

Figure 3.2: The mechanism of AC Stark shift ΔE in dressed atom picture. The definitions of symbols are discussed in the text.

$$|a(N)\rangle \approx |g, N+1\rangle \tag{3.7}$$

$$E_{|a(N)\rangle} \approx \hbar\Delta_{ge} + \frac{\hbar\Omega^2}{4|\Delta_{ge}|} \tag{3.8}$$

$$\Rightarrow \Delta E_g = E_{|a(N)\rangle} - \Delta_{ge} = +\frac{\hbar\Omega^2}{4|\Delta_{ge}|} \tag{3.9}$$

$$|b(N)\rangle \approx |e, N\rangle \tag{3.10}$$

$$E_{|b(N)\rangle} \approx -\frac{\hbar\Omega^2}{4|\Delta_{ge}|} \tag{3.11}$$

$$\Rightarrow \Delta E_e = E_{|b(N)\rangle} = -\frac{\hbar\Omega^2}{4|\Delta_{ge}|}. \tag{3.12}$$

The absolute value $\Delta E_{g,e}$ of the AC Stark shift in Eqs. 3.9 and 3.12 can be obtained as $\hbar\Omega^2/4|\Delta_{ge}|$, which is directly proportional to the intensity of the incident light field, and inversely proportional to the detuning of the light field frequency. In the optical lattice, we tend to trap atoms in a potential well, so a large detuning (a few GHz usually) is chosen to prevent the loss from unexpected scattering, and this kind of optical lattice is also called "non-dissipative optical lattice".

In the bare atom picture, AC Stark effect is treated as the energy shift caused by the induced dipole moment in classical electromagnetism [20], or the second-order

time-dependent perturbation theory in quantum mechanics [21, 22]. The induced dipole moment $\mathbf{P}$ (per unit volume) is written as below:

$$\mathbf{P} = \alpha \cdot \mathbf{E} + \beta : \mathbf{EE} + \gamma : \mathbf{EEE} + \cdots , \tag{3.13}$$

where $\mathbf{E}$ is the electric field which induces the dipole moment $\mathbf{P}$; α is the polarizability; β and γ are the high-order terms, called hyperpolarizability. The hyperpolarizability is the key role to induce non-linear optical effects, but it highly depends on the deviation from the harmonic oscillator model of electron binding potentials and chemical bonds or charge transfer phenomena in molecules or solids. Throughout this thesis, the polarizability α is only considered in the analysis. The induced dipole energy is shown as follows:

$$\begin{aligned} \Delta E &= -\int_{\upsilon} \mathbf{P} \cdot \mathbf{E} d\upsilon = -\int_{\upsilon} \mathbf{E} \cdot \alpha \cdot \mathbf{E} d\upsilon \\ &\approx \sum_{e} \frac{\langle g|\mathbf{d} \cdot \mathbf{E}^*|e\rangle\langle e|\mathbf{d} \cdot \mathbf{E}|g\rangle}{\hbar\Delta_{ge}} = \frac{\hbar\Omega^2}{4\Delta_{ge}}. \end{aligned} \tag{3.14}$$

In Eq. 3.14, the Rabi frequency Ω is defined as $(2/\hbar)\langle e|\mathbf{d} \cdot \mathbf{E}|g\rangle$, and the derived ΔE is the same as that in dressed atom picture. AC Stark effect corresponds to the behaviour of two transition dipole moments, $\langle g|\mathbf{d} \cdot \mathbf{E}^*|e\rangle$ and $\langle e|\mathbf{d} \cdot \mathbf{E}|g\rangle$, so the polarization direction of $\mathbf{E}$ is very crucial, because Clebsch-Gordan coefficients of atomic transitions between different Zeeman states are different. In another words, we could treat the polarizability α as a rank-2 tensor, and the perturbation Hamiltonian $\widehat{H}'$ of AC Stark effect is written as [23]:

$$\widehat{H}'(F) = c_0^{(0)}(F) + \sum_{q=-1}^{1} c_q^{(1)}(F)\, {}^{FF}\widehat{T}_q^{(1)} + \sum_{q=-2}^{2} c_q^{(2)}(F)\, {}^{FF}\widehat{T}_q^{(2)}, \tag{3.15}$$

where $c_q^k(-k \leq q \leq k)$ is the proportional coefficient, which is a function of the detuning Δ_{ge}, Rabi frequency Ω, total angular momentum quantum number F, and symmetric condition relying on the polarization of the incident light field; ${}^{FF}\widehat{T}_q^{(k)}$ is the irreducible tensor operator, which shows the different behaviours among magnetic quantum numbers m_F. In Eq. 3.15, the first term is called scaler light shift, which depends on the intensity of the light field. The second term is called vector light shift, which is proportional to the magnetic quantum number m_F. This term

offers a fictitious Zeeman effect [24]. The third term is called tensor light shift, which is a function of the square of magnetic quantum number m_F^2 [23, 25, 26]. Here, we choose a large detuning Δ_{ge} (12 GHz) and the light field with relatively low intensity (around 50 mW per beam with 1 cm^2 cross section). From Eq. 3.14, the difference of AC Stark shifts among different Zeeman states is, therefore, small enough to be ignored, which means that only scaler light shift would be taken into account in our experiment.

3.1.1.1 Band Structure

Both of an optical lattice and a dipole trap take advantage of AC Stark effect to trap atoms, but they are different in many ways, one of which is the band structure. Taking the general case of 1D optical lattice as an example, the light field **E** is defined as those in Eqs. 1.12 - 1.15, with a tilted angle θ of the polarization as shown in Eq. 3.16:

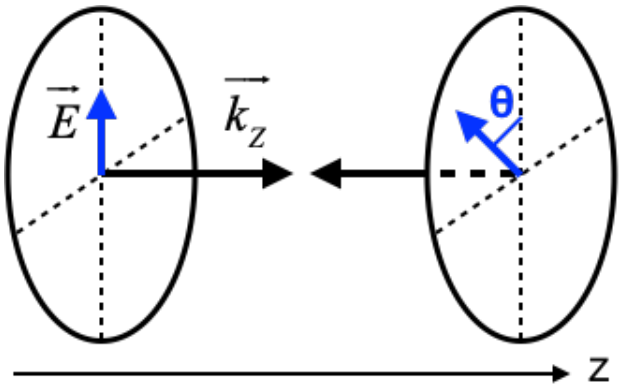

Figure 3.3: The geometry of two counter-propagating light fields to build an optical lattice [27].

$$\mathbf{E}(z) = \sqrt{2}A\{-e^{-i\theta/2}\cos(kz+\theta/2)\epsilon_+ + e^{i\theta/2}\cos(kz-\theta/2)\epsilon_-\}, \tag{3.16}$$

where A is the amplitude, with the same definition as ε_0 or ε_0' in Eq. 1.13. ϵ_+ and ϵ_- are the right-handed and left-handed helicity of the light field. With the spatial distribution of the light field, the potential operator $\widehat{U}(z)$ of the optical lattice can be written as follows [27]:

$$\begin{aligned}\widehat{U}(z) &= -\mathbf{E}(z)\cdot\widehat{\alpha}\cdot\mathbf{E}(z) - \widehat{\mu}\cdot\mathbf{B} \\ &= -\frac{2U_0}{3}\{2[1+cos\theta\cos(2kz)]\widehat{I} + [sin\theta\sin(2kz)]\widehat{\sigma}_z\} - \frac{\hbar}{2}\gamma\mathbf{B}\cdot\widehat{\sigma}, \end{aligned} \tag{3.17}$$

where U_0 is a constant potential without spatial and polarization factor; $\widehat{I}$ and $\widehat{\sigma}$ are the identity and Pauli spin operator, respectively; $\mathbf{B}$ is an external magnetic field. From Eq. 3.17, we can see that the potential of the optical lattice consists of a simple periodic distribution and two kinds of interactions with magnetic fields, one of which is an internal magnetic field produced by the curl of the time-variable electric field $(\epsilon^*(z)\times\epsilon(z))$, and the other one is externally applied ($\mathbf{B}$). The internal magnetic field is the source of the vector light shift, which is always along the propagation direction of the light field and vanishes in the linear polarization case. However, the optical lattice is also affected by other magnetic fields in any direction, so the Pauli operator $\widehat{\sigma}$ in the last term is not specifically projected on z-axis (propagation direction). AC Stark shift on the Zeeman state is a function of the magnetic quantum number along with the light propagating direction as the quantization axis, so the external magnetic field could break the symmetry of the band structure of the optical lattice. Fortunately, it is not an issue in our experiment because of the large detuning, low field power and linear polarization of the lattice field.

From $\widehat{U}(z)$ in Eq. 3.17, the band structure of 1D lattice could be solved. Taking Cs atoms as an example, Fig. 3.4 shows the potential and the corresponding band structure [27]. In Fig. 3.4, E_R is the recoil energy of the lattice field; Γ is the spontaneous decay rate of the excited state $6P_{3/2}(F'=5)$; k and q are the lattice photon momentum and particle quasi-momentum in the lattice, respectively. The details of the band structure will be discussed in Chapter 4. In our Raman sideband cooling experiment, the lattice band is approximated with a simple harmonic oscillator model with energy series $E_{\text{lattice}} = \hbar\omega_{\text{vib}}(v+1/2)$, where ω_{vib} is the angular frequency of the vibration in the lattice; v is a non-negative integer, which represents the quantum number of discrete energy levels of a quantum harmonic oscillator.

Aforementioned discussions are related to the axial trapping of 1D lattice. The 1D dipole trap lacks the axial confinement, so it has no band structure in axial direction, just be a guiding channel. In fact, both of 1D lattice and dipole trap can produce radial trapping based on the beam profile, so it should also produce some

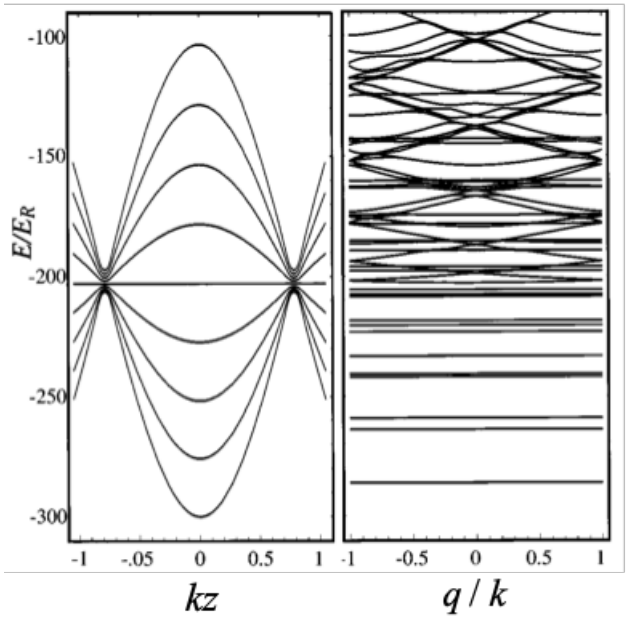

Figure 3.4: 1D lin⊥lin lattice with $U_0 = 150E_R$ and detuning -2000Γ from $6S_{1/2}(F = 4)$ to $6P_{3/2}(F' = 5)$ of Cs atoms. *Left*: the potential energies of different Zeeman states calculated with Eq. 3.17, as a function of the spatial phase factor kz; *Right*: the complete band structures of different Zeeman states in the first Brillouin zone. Below the crossing points of the energy bands, the bands are in the tight-binding regime with the energy width less than $0.1E_R$. Above, there are hybrid bands with energy crossing points due to stimulated Raman resonance between some Zeeman states [27].

band structure in principle. But, the beam size (diameter) of our lattice field is relatively large (about 0.7 cm), compared with the atomic cloud size (0.14 cm) and the spatial period of the lattice (390 nm), so the potential in the radial direction could be treated as a constant in our experiment.

3.1.1.2 Crystallography

The optical lattice is produced by the standing wave of the light field owning some similar properties as a lattice in a solid, one of which is the band structure, and another one is the geometric structure in crystallography. Taking a general 3D lattice as an example, we assume that the periodic interval is $\mathbf{a}$, and the potential $\widehat{U}$ shows the spatial periodicity as below:

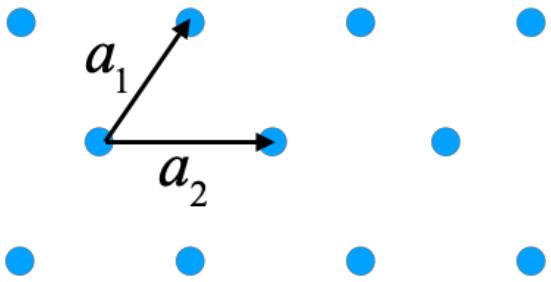

Figure 3.5: The spatial base vector $\mathbf{a}_i$ in a lattice.

$$\widehat{U}(\mathbf{r}) = \widehat{U}(\mathbf{r} + \mathbf{a}) \tag{3.18}$$

$$\mathbf{a} = n_1\mathbf{a}_1 + n_2\mathbf{a}_2 + n_3\mathbf{a}_3, \tag{3.19}$$

where n_i and $\mathbf{a}_i$ are integers and base vectors in the unit cell of the lattice, respectively. Considering the orientation of light beams for optical lattice, and dropping the time-dependent term $exp(i\omega t)$ in Eq. 1.12 to simplify the model, the corresponding geometry of the lattice can be obtained as follows:

$$\mathbf{E}(\mathbf{r}) = \sum_m \varepsilon_m \epsilon_m e^{i\mathbf{k}_m\cdot\mathbf{r}} + c.c. \tag{3.20}$$

$$U(\mathbf{r}) \propto I \propto |\mathbf{E}^*\mathbf{E}| = \sum_m \varepsilon_m^2 + \sum_{m<n} 2\varepsilon_m\varepsilon_n^*(\epsilon_m\cdot\epsilon_n)cos[(\mathbf{k}_m - \mathbf{k}_n)\cdot\mathbf{r}]. \tag{3.21}$$

ε_m, ϵ_m and $\mathbf{k}_m$ are the amplitude, the polarization direction and the wave vector of the mth light field, respectively, with the same definitions as those in Eqs. 1.12-1.15. $\mathbf{r}$ and $(\mathbf{k}_m - \mathbf{k}_n)$ are the general position vector and the reducible base vector of the lattice field in k-space, respectively. The set of base vectors in k-space are also called the translational vectors $\mathbf{G}$ of the reciprocal lattice in solid state physics [28]. Owing to the linear dependency of vectors in the space, we could select some of them as the base vectors $\mathbf{a}_i^*$ in k-space, e.g. select 3 $(\mathbf{k}_m - \mathbf{k}_n)$ vectors $(\mathbf{k}_1 - \mathbf{k}_2, \mathbf{k}_1 - \mathbf{k}_3, \mathbf{k}_1 - \mathbf{k}_4)$ as base vectors $(\mathbf{a}_1^*, \mathbf{a}_2^*, \mathbf{a}_3^*)$ of a 3D reciprocal lattice. Because of the orthogonality between base vectors in the direct lattice and reciprocal lattice, we could derive the set of base vectors $\mathbf{a}_i$ in direct lattice [29, 30]:

$$\mathbf{a}_i \cdot \mathbf{a}_j^* = 2\pi\delta_{ij} \tag{3.22}$$

$$\mathbf{a}_1 = 2\pi\frac{\mathbf{a}_2^* \times \mathbf{a}_3^*}{\mathbf{a}_1^* \cdot \mathbf{a}_2^* \times \mathbf{a}_3^*}, \quad \mathbf{a}_2 = 2\pi\frac{\mathbf{a}_3^* \times \mathbf{a}_1^*}{\mathbf{a}_1^* \cdot \mathbf{a}_2^* \times \mathbf{a}_3^*}, \quad \mathbf{a}_3 = 2\pi\frac{\mathbf{a}_1^* \times \mathbf{a}_2^*}{\mathbf{a}_1^* \cdot \mathbf{a}_2^* \times \mathbf{a}_3^*}, \tag{3.23}$$

where δ_{ij} is Kronecker delta, equal to 1 for $i = j$, or 0 for $i \neq j$. Equation 3.23 shows the calculation of $\mathbf{a}_i$ of a general 3D lattice. Taking a 4-beam tetrahedral geometry of light fields to produce a 3D lattice as an example, Fig. 3.6 shows the light beam orientation and the unit cell of the corresponding real-space lattice [30].

3.1.2 Cooling Mechanism

As mentioned in Section 1.1.3 and the beginning of this chapter, sub-Doppler cooling technique is although straightforward to operate, it is hard to reach the recoil temperature. To solve this issue, a new technique to provide a confinement to atoms, which more efficient than the dissipative lattice of sub-Doppler cooling, was developed, which is also called the ground-state cooling technique.

The mechanism of the ground-state cooling is to build an artificial trap to limit the motion of atoms, which quantizes the energy of atoms in the trap, and then stepwise transfer the atomic population to the ground state of the trap by the elaborated, specific momentum kicks for the reduction of the kinetic energy of atoms, and finally achieve a lower temperature. The so-called artificial trap could be any potential well, one of which is the optical lattice. Raman sideband cooling and EIT cooling (mentioned in Section 1.2.4) are both members of the ground-state cooling

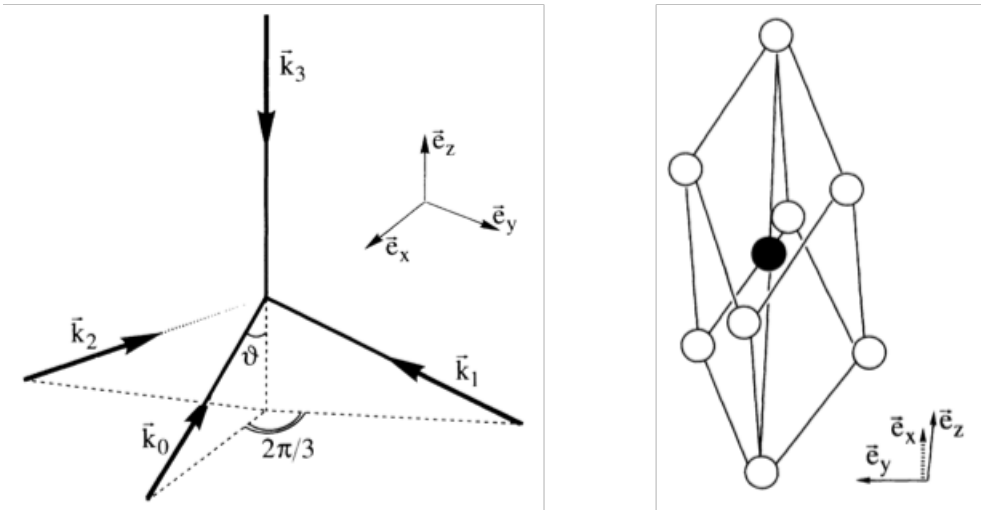

Figure 3.6: The light wave vector $\mathbf{k}_m$ orientation and the unit cell of the corresponding lattice. $\mathbf{e}_{x,y,z}$ are unit vectors of the spatial axes; θ is the angle between z axis and other three light beams, which affects the final geometry of the lattice; white and black balls indicate two types of lattice sites with different helicities of the light fields [30].

family. In our system, the one we implement is Raman sideband cooling, which consists of four components: optical lattice, magnetic field, two-photon Raman field, and optical pumping field.

In Raman sideband cooling, the potential produced by the optical lattice is approximated as a harmonic oscillator model, so the total external energy E_{lattice} of an atom in the lattice is $\hbar\omega_{\text{vib}}(v+1/2)$, as mentioned in Section 3.1.1.1. Taking a 1D lattice along z-axis as an example in Eqs. 3.24 - 3.26, η is Lamb Dicke parameter. k_z is the wave vector of light field along z-axis. z_0 is the vibration width in the ground state ($v = 0$) of the harmonic oscillator model. η^2 shows the ratio of the recoil frequency ω_R to the vibrational level spacing ω_{vib}. The $(2v + 1)$ term represents the increase of the vibration width of higher motional states. Lamb Dicke regime requires that the light field makes a small enough phase difference ($k_z z$) within the interaction length ($z = z_0\sqrt{2v + 1}$) to suppress high-order transitions among motional states [31].

$$\eta = k_z z_0 \tag{3.24}$$

$$\eta^2 = (\sqrt{\frac{2m\omega_R}{\hbar}}\sqrt{\frac{\hbar}{2m\omega_{\text{vib}}}})^2 = \frac{\omega_R}{\omega_{\text{vib}}} \tag{3.25}$$

$$\eta^2(2v+1) \ll 1, \tag{3.26}$$

Other than defining the quantisation axis for atom-light interaction, an external magnetic field is not necessary for Raman sideband cooling. However, in order to simplify the optical setup, the degenerate Raman sideband cooling was developed to share the light field of the optical lattice and two-photon Raman transition by a specific Zeeman splitting. In Fig. 3.7, a two-photon Raman transition is implemented to transfer the population into different vibrational levels by two degenerate Raman fields. To make this situation happen, the Zeeman splitting needs to be tuned to match the vibrational level spacing [12].

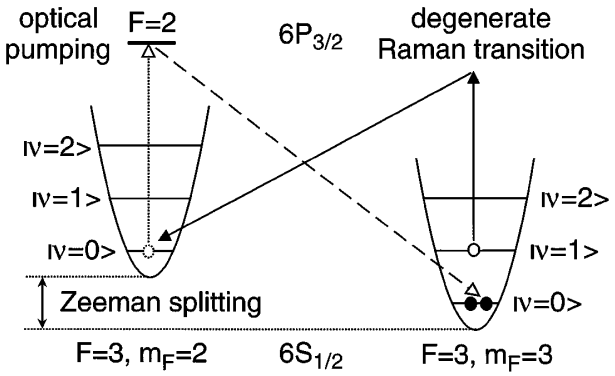

Figure 3.7: The cooling cycle of the degenerate Raman sideband cooling for Cs $|F = 3\rangle$ state [12].

The functionality of Raman field is to transfer the population into other motional states of different vibrational quantum numbers ($v \leftrightarrow v \pm 1$) by providing $\hbar\mathbf{a}_i^*$ momentum kick (see Eq. 3.23). However, two-photon Raman field could also transfer the population to higher vibrational level as a heating process ($v \rightarrow v+1$). Optical pumping field is then used to pump atoms on the lower vibrational level into another Zeeman state while preserving the same vibrational level. Finally, to end up the cooling process, the population of atoms fall into a dark state without the pumping effect of two-photon Raman field and optical pumping field by choosing a

proper polarization of the optical pumping field. As the example in Fig. 3.7, the polarization of optical pumping field should be $\sigma^+ + \pi$.

3.2 Experimental Setup

3.2.1 Configuration

The atomic transitions used in our experiment are shown in Fig. 3.8. The configurations of Doppler cooling and sub-Doppler cooling are already discussed in Section 2.2.1. Only the key roles of Raman sideband cooling fields are described as follows:

1. The optical lattice field: it was produced by a taper-amplifier seeded by a diode laser locked at 12 GHz red-detuned D2 transition. Each lattice beam is about 47 mW and 7 mm beam waist. The diode laser was injection-locked by the cooling laser, and its frequency was tuned by a phase-modulated EOM (electro-optical modulator) at 12 GHz. The -1 order sideband of the EOM was filtered through a temperature-controlled Fabry-Pérot etalon to injection-lock the diode laser.

2. The circularly-polarized optical pumping field: 20 MHz blue-detuned D1 $|F = 3\rangle \rightarrow |F' = 2\rangle$ transition. This D1 transition and polarization were chosen to pump atoms into the spin-polarized state, which is a dark state in D1 $|F = 3\rangle \rightarrow |F' = 2\rangle$ transition. 20 MHz blue-detuning was set to reduce the single-photon scattering rate and the Raman coupling between the dark state and its neighbourhood vibrational states, which are discussed in Section 3.3.1. The larger hyperfine splitting of the excited state (360 MHz, much larger than that of D2 line) could avoid unexpected off-resonant transitions. As shown in Fig. 3.9, σ^+ and a little fraction of π polarization are both required in the cooling process, so we tilted a small angle (10°) of the beam orientation to produce π polarization light, as shown in Fig. 3.10.

3. 2-state repump field: even with a small probability, atoms which interact with the optical pumping field can be pumped to the $|F = 2\rangle$ state and leave the cooling process. We prepared a 2-state repump field with the resonant MOT repump field to pump atoms back to the $|F = 3\rangle$ state to continue the cooling process.

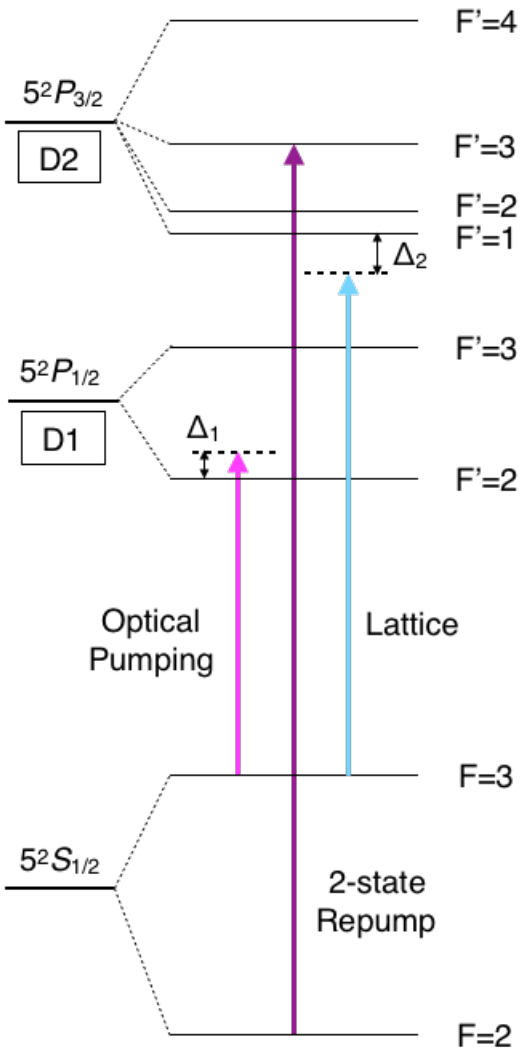

Figure 3.8: The atomic transitions for degenerate Raman sideband cooling. The magenta arrow is the optical pumping field with 20 MHz (Δ_1) blue-detuned from D1 $|F = 3\rangle \rightarrow |F' = 2\rangle$ transition. The purple arrow is 2-state repump field with D2 $|F = 2\rangle \rightarrow |F' = 3\rangle$ transition. The skyblue arrow is the lattice field with 12 GHz (Δ_2) red-detuned from D2 transition.

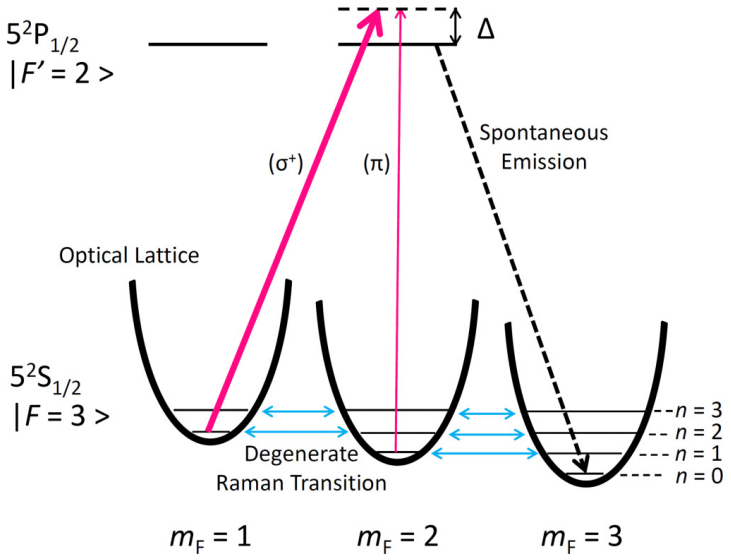

Figure 3.9: Degenerate Raman sideband cooling scheme in this experiment. The cyan lines are degenerate Raman fields; the magenta lines are optical pumping fields, where their thickness qualitatively represent the power difference between σ^+ and π polarized fields; Δ is the detuning of the optical pumping field.

3.2.2 Optical Setup

Figure 3.10 shows the alignment of our experimental setup for Raman sideband cooling. The three cyan lines are the light fields of the optical lattice and two-photon Raman transitions, which refer to the design in Reference [32]. Our optical lattice is a 2D lattice on xy plane, where the spatial function of its potential U is shown in Eq. 3.27, based on the analysis in Section 3.1.1.2.

$$U = -\frac{4}{3}u[\frac{3}{2} + \cos(\sqrt{3}ky) + \cos(\frac{\sqrt{3}ky - 3kx}{2}) + \cos(\frac{\sqrt{3}ky + 3kx}{2})], \tag{3.27}$$

where u is the potential energy made by a single light beam, k is the wavevector of the lattice field. To illustrate the geometric structure, the contour plot is used to show the potential distribution as in Fig. 3.11 (set u and k are both 1 for simulation). Near the center of the potential dip (e.g. x=0 and y=0), Eq. 3.27 could be approximated with Eq. 3.28. The harmonic oscillator model and its energy level series will then be used in the further discussion.

$$U \approx u[-6 + 3k^2(x^2 + y^2)]. \tag{3.28}$$

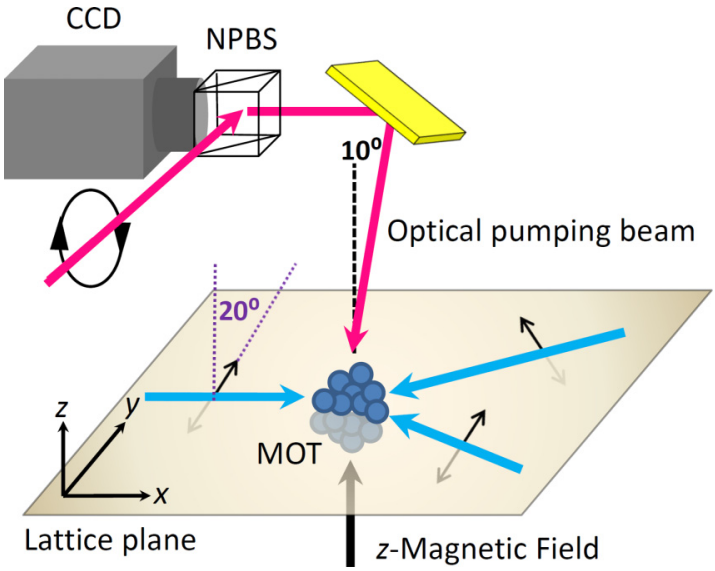

Figure 3.10: The optical setup of Raman sideband cooling. The details of components in the setup are explained in the text.

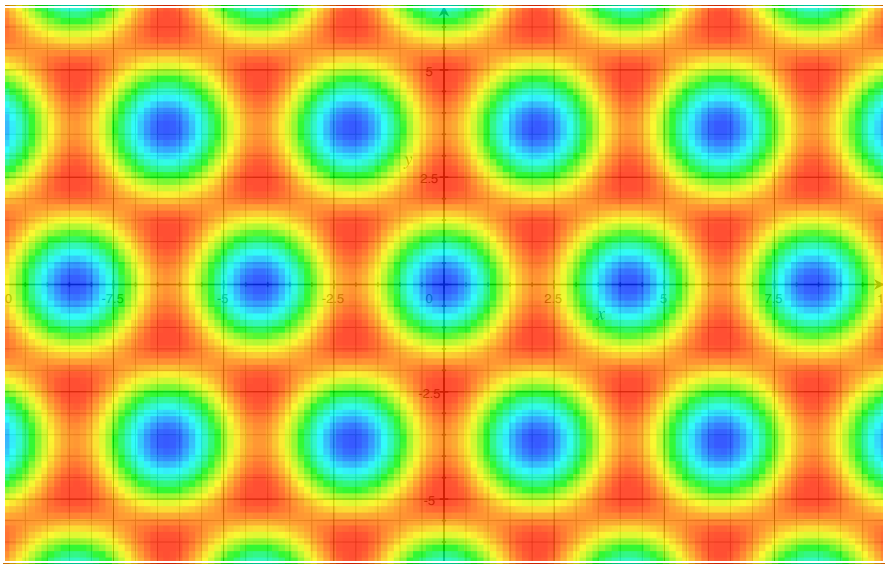

Figure 3.11: The contour plot shows the energy distribution of the lattice potential U in Eq. 3.27. The blue to red color indicates the potential energy from low to high values.

Another function of the lattice field is to play the role of two-photon Raman field. Usually, two fields with different frequencies are required to drive a stimulated Raman transition for population transfer from one state to another with different

energy. In our experiment, we applied an external magnetic field along z axis to shift the energy of the Zeeman states with one vibrational level spacing ($\hbar\omega_{\mathrm{vib}}$), and tilted a small polarization angle (20°) to create π and $\sigma^{\pm}$ polarization simultaneously. The lattice field could, therefore, drive the degenerate Raman transitions (see Fig. 3.9), which dramatically simplified the optical setup.

The optical pumping field was sent nearly vertically to the atomic cloud. We used a non-polarizing beam splitter (NPBS) and a gold mirror to steer the optical pumping beam into the atomic cloud, and tilted a small orientation angle (10°) along the vertical direction to create an extra π polarization as shown in Fig. 3.9. The CCD camera was used to record the fluorescent image of the atomic cloud on xy plane and measure the temperature of the atomic ensemble along x and y axes (the calculation equation is the same as Eq. 2.8). The results are shown in Fig. 3.12.

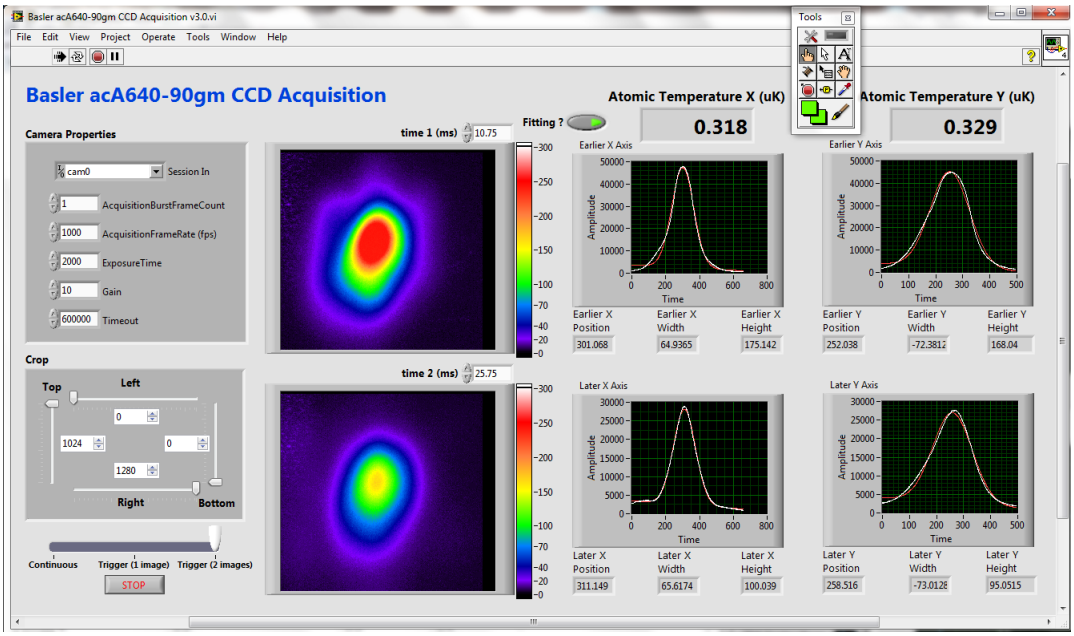

Figure 3.12: The program interface of the CCD image acquisition and the measured temperature of x and y profiles.

3.2.3 Time Sequence

As discussed in Section 3.2.1 and 3.2.2, the time sequence of our Raman sideband cooling system shown in Fig. 3.13 is composed of four parts. Firstly, MOT fields

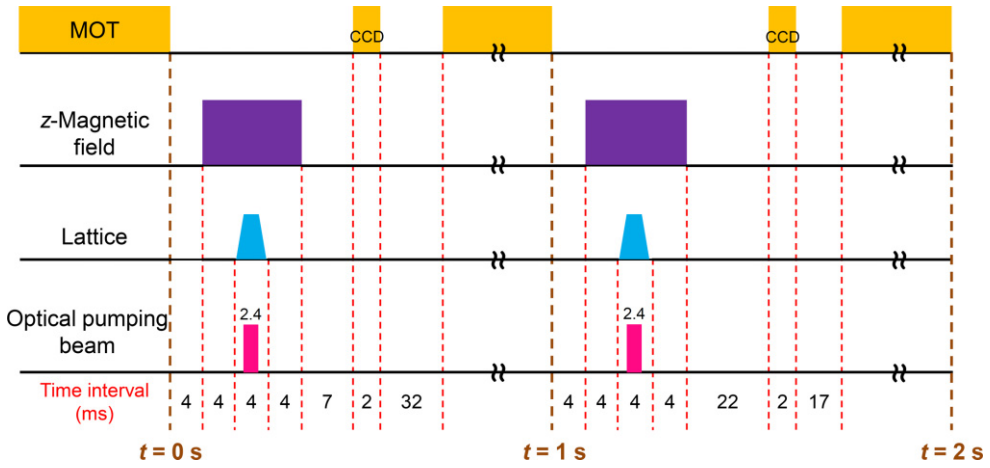

Figure 3.13: The time sequence of the Raman sideband cooling. The detail is explained in the text.

containing the cooling field, the repump field and the quadrupole magnetic field, were implemented to build a cold atomic ensemble with the temperature around 20 μK (see the details in Sections 1.1.4 and 2.2.1). Secondly, the magnetic field along z-axis was switched on to shift the Zeeman states and define the quantization axis for atom-light interaction. We extended the duration of 4 ms before and after the cooling process, to ensure a steady state of the magnetic field along z-axis during the cooling process. Thirdly, the lattice field was adiabatically switched on for a 2D optical lattice and transfered the population to the vibrational (motional) states with smaller quantum numbers by two-photon degenerate Raman transitions. The lattice pulse was created by a function generator following Eq. 3.29, which was optimized with the duration 4 ms. The rising / falling time 0.8 ms of the lattice pulse was shown in Fig. 3.14. The adiabaticity of the lattice pulse was very crucial, where the rising stage loaded atoms into the lattice trap with a slowly-increased potential well shown in Fig. 3.14, to prevent the atoms from the internal transition to higher lattice bands in the beginning; the falling stage could process the adiabatic cooling to cool down the atoms further [33] after Raman sideband cooling. Fourthly, the optical pumping field and 2-state repump field were introduced during the steady state of the lattice field (the 2.4 ms plateau in Fig. 3.14) to pump the population into the dark state $|F = 3, m_F = 3\rangle$ and finish the cooling process. Also, at 7 and 22 ms after the cooling process, MOT field was opened again for atomic cloud imaging

to measure the temperature with time-of-flight method in Eq. 2.8.

$$I = \tanh(b(t - 0.4)) + \tanh(-b(t - 3.6)) \tag{3.29}$$

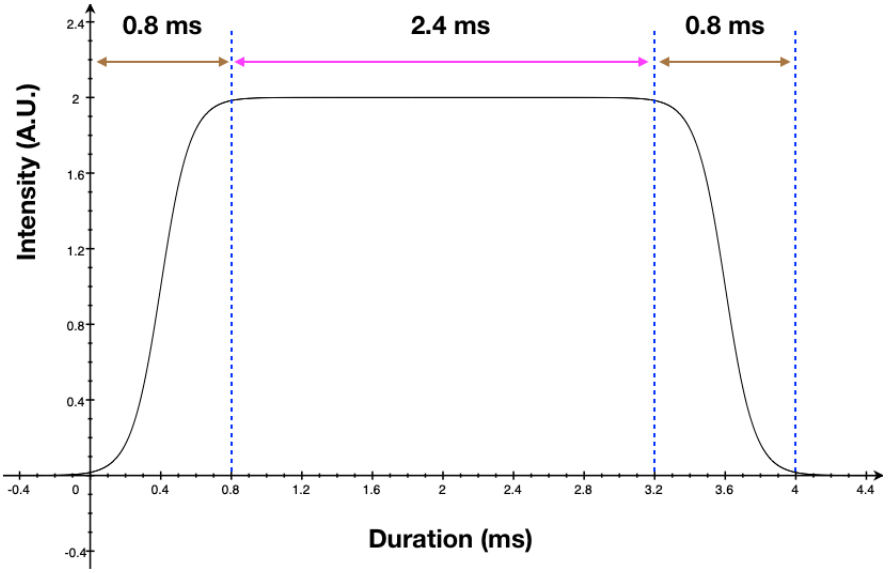

Figure 3.14: The time profile of the lattice pulse created by a function generator with Eq. 3.29. b is 6 in this figure, which is proportional to the rising / falling slope.

3.3 Data and Discussion

In our experiment [18], Raman sideband cooling could achieve 400 nK, which is very close to the recoil temperature 357 nK for D1 transition. Figure 3.15 shows the atomic cloud profiles at 7 and 22 ms release time after Raman sideband cooling process. The width of the atomic cloud is smaller after sideband cooling compared to the atomic ensemble only cooled by Doppler cooling and sub-Doppler cooling techniques. Another reason we chose Raman sideband cooling was its low loss of atoms. Raman sideband cooling transfers the population from higher energy levels to lower energy levels instead of abandoning them. In our experiment, more than 60% of atoms remained in the trap after Raman sideband cooling.

To confirm that atoms were pumped to the spin-polarised state after the cooling process, the Zeman spectrum was measured as shown in Fig. 3.17. We integrated the acquired intensity data of the 2D cloud image after the population transfer by

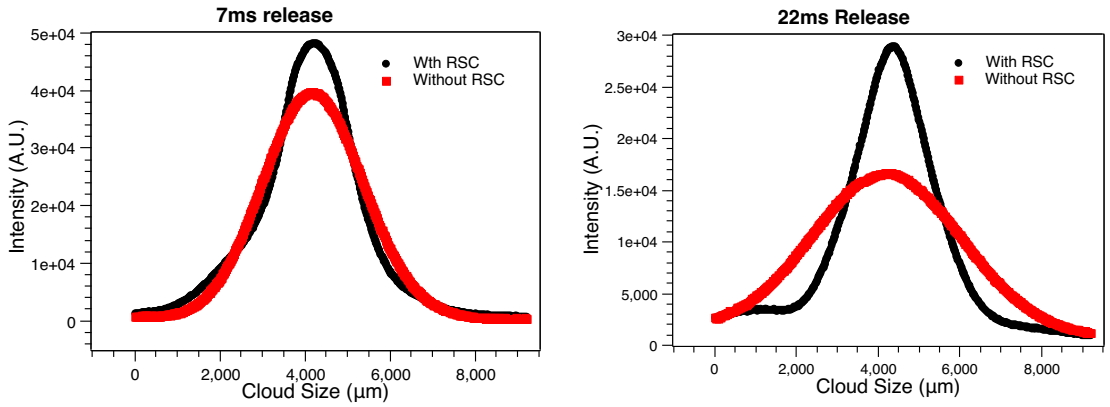

Figure 3.15: Spatial profiles of the atomic cloud with and without Raman sideband cooling (RSC) at 7 and 22 ms release time after the cooling process.

the radio wave and the removal of atoms in $|F = 3\rangle$ by a blow-away field (see Fig. 3.16). We scanned the radio wave frequency to measure the population of atoms in the Zeeman states as shown in Fig. 3.17. Owing to the fluctuation of the laser power, magnetic field, and the small Zeeman splitting, we were not able to resolve all the Zeeman sub-levels. Nonetheless, an obvious peak on the left-handed side showed that the population was pumped to the spin-polarized state $|F = 3, m_F = 3\rangle$ after Raman sideband cooling.

3.3.1 Dependency of Cooling Temperature

The final temperature achieved by Raman sideband cooling is the result of the competition between cooling and heating mechanisms. Refer to Reference [34], the energy change ΔE of atoms in a cooling cycle is:

$$\Delta E = \hbar\omega_{\text{vib}}(2\eta^2 - 1). \tag{3.30}$$

The first term in Eq. 3.30 refers to the increase of two recoil energy E_R from the optical pumping field (absorption and emission) in each cooling cycle, and the second term is related to the decrease of the energy of an atom by one quanta of the vibrational energy $\hbar\omega_{\text{vib}}$. The cooling effect takes place when ΔE is negative. Please note that the population transfer caused by two-photon degenerate Raman transition is not homogeneous due to the fluctuation or the spatial gradient of the

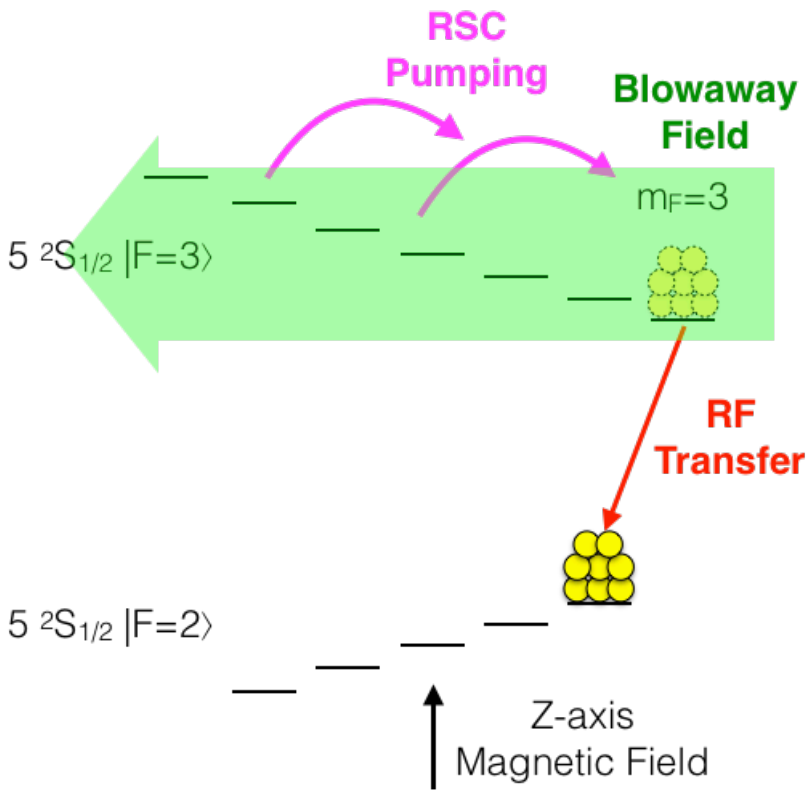

Figure 3.16: The measurement scheme of Zeeman spectrum.

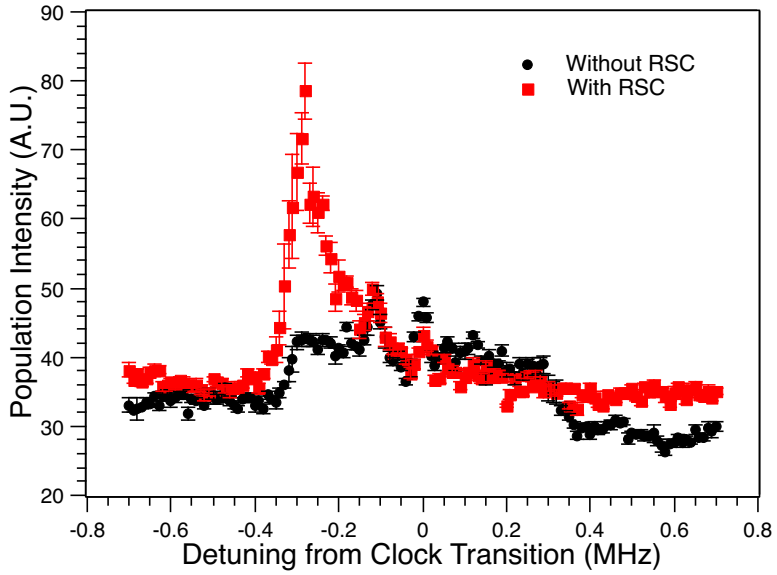

Figure 3.17: Zeeman spectrum with and without Raman sideband cooling.

lattice field power and z-axis magnetic field. As a result, the cooling efficiency might not be uniform through the whole atomic ensemble.

Assuming the cooling is uniform in the ensemble, we consider an empirical equation of the time evolution of the cooling temperature of atoms as below:

$$\frac{dT}{dt} = \frac{\hbar\omega_{\text{vib}}\overline{n}\gamma(2\eta^2 - 1)}{k_B}, \tag{3.31}$$

where $\overline{n}$ is the average occupation number of atoms in the harmonic potential and can be written as a function of temperature from the partition function of the energy series of the harmonic oscillator states shown in Eq. 3.32:

$$\begin{aligned}\overline{n} &= \sum_{v=0}^{\infty} exp(-\hbar\omega_{\text{vib}}(v+\frac{1}{2})/k_BT) \\ &\approx \frac{e^{-\frac{1}{2}\hbar\omega_{\text{vib}}/k_BT}}{1-e^{-\hbar\omega_{\text{vib}}/k_BT}} = \frac{1-\frac{1}{2}\frac{\hbar\omega_{\text{vib}}}{k_BT}}{\frac{\hbar\omega_{\text{vib}}}{k_BT}} = \frac{T-T_0}{2T_0}\end{aligned} \tag{3.32}$$

$$T_0 = \frac{\hbar\omega_{\text{vib}}}{2k_B}. \tag{3.33}$$

In Eqs. 3.32 and 3.33, T_0 is the temperature of atoms with zero-point energy $\hbar\omega_{\text{vib}}/2$. γ in Eq. 3.31 is the photon scattering rate of the optical pumping field, calculated as below:

$$\gamma = \frac{I/I_s\Gamma/2}{1+4(\Delta/\Gamma)^2}, \tag{3.34}$$

where I is the intensity of the optical pumping field, I_s (8 mW/cm^2) is the saturation intensity of ^{85}Rb D1 transition $|F=3\rangle \rightarrow |F'=2\rangle$ with π polarization, and Γ and Δ are the spontaneous decay rate of $|F'=2\rangle$ state and the detuning of $|F=3\rangle \rightarrow |F'=2\rangle$ transition driven by the optical pumping field, respectively. The temperature after Raman sideband cooling process could be derived after modifying Eq. 3.31 shown as follows:

$$\frac{dT}{dt} = \frac{\hbar\omega_{\text{vib}} \cdot \frac{T-T_0}{2T_0} \cdot \gamma(I,\Delta)(2\eta^2-1)}{k_B} = -A\frac{T}{T_0} + A \tag{3.35}$$

$$A = -\frac{\hbar\omega_{\text{vib}}\gamma}{2k_B}(2\eta^2-1)$$

$$\int_{T_i}^{T_f} \frac{dT}{-A\frac{T}{T_0}+A} = \int_0^{t_f} dt \tag{3.36}$$

$$T_f = T_0 + (T_i - T_0)e^{-t_f\frac{A}{T_0}}, \tag{3.37}$$

where T_i and T_f are the temperature before and after Raman sideband cooling process, respectively, and t_f is the time duration of the cooling process, which is 2.4 ms in our optimized case (see Fig. 3.14). After Raman sideband cooling process, the lattice power is slowly ramped to zero, where the population on the vibrational states would stay in their original states without internal transitions. When the vibrational level spacing $\hbar\omega_{\text{vib}}$ decreases, atoms gradually lose the potential energy from the lattice trap and keep the same population distribution $exp(-\hbar\omega_{vib}(v+1/2)/k_BT)$ based on Boltzmann distribution. As a result, the final temperature T decreases, which is called the adiabatic cooling, as mentioned in Section 3.2.3. Referring to Reference [33], the final temperature T_{ff} could be derived as follows:

$$T_{ff} = T_R(\frac{Q_0}{k})^2\frac{1+4f_B+f_B^2}{12(1-f_B)^2}, \tag{3.38}$$

where T_R is the recoil temperature and Q_0 is the spatial frequency in k-space, $(\mathbf{a}_i^* = \mathbf{k}_m - \mathbf{k}_n)$ as discussed in Section 3.1.1.2. In our 2D triangular lattice, $Q_0 = \sqrt{3}k$, where k is the wavevector of the lattice field. f_B is Boltzmann factor $exp(-\hbar\omega_{\text{vib}}/k_BT_f)$. We fit our experimental data with the theoretical model of Eqs. 3.37 and 3.38 of the final temperature T_{ff} on the cooling duration, the detuning of the optical pumping field and the lattice field power.

Figures 3.18 and 3.19 show the temperature as a function of the cooling duration t_f. In this experiment, the temperature gradually decreased with the time duration of the cooling process, which followed the time evolution of the ensemble temperature in Eq. 3.31, as shown in Fig. 3.18. However, the temperature rised in longer cooling duration cases because atoms sliped out of the dipole trap along z-axis, where the vibrational frequency ω_{vib} became a function of time. When the atoms started to escape from the dipole trapping beam area, the cooling mechanism cannot

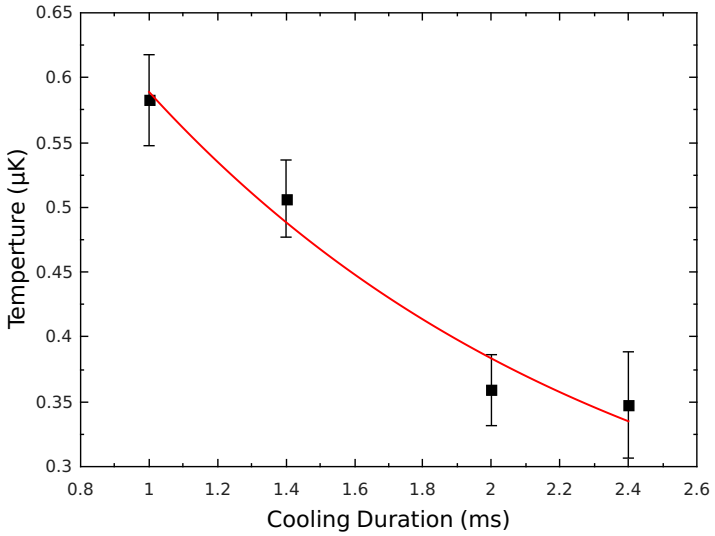

Figure 3.18: The cooling temperature as a function of the duration of Raman sideband cooling. The power and detuning of the optical pumping field are 1 mW and +20 MHz, respectively; the power of the lattice field is 47 mW per beam; and the temperature is measured with y-axis profile. In the theoretical fit, the vibrational frequency ω_{vib} is assumed as a constant.

work efficiently, which resulted in the increase of the temperature. The tendency of the increase of the temperature matches our theoretical model and shows that the optimized duration for the cooling process is 2.4 ms, as shown in Fig. 3.19.

The optical pumping field played an important role in Raman sideband cooling, so we checked the cooling temperature as a function of the optical pumping field power with different detuning Δ, as shown in Fig. 3.20. The fitting results of the final temperature matched our theoretical model in the low power range as shown in Fig. 3.21. When the power I of the optical pumping field increased, it blew the atomic ensemble away, which is the reason why the temperature increased and some data points were missing in the high power region. We also checked four detuning values and measured the final temperature. Different detuning Δ had a similar trend as a function of the pumping field power. However, when the sign of the detuning reversed, the behaviour was different due to the sign of AC Stark shift. The red detuned optical pumping field shifted the vibrational levels down, which increased the coupling between the dark state $|F = 3, m_F = 3, v = 0\rangle$ and the neighbour vibrational state $|F = 3, m_F = 2, v = 0\rangle$. As a result, the intended dark state

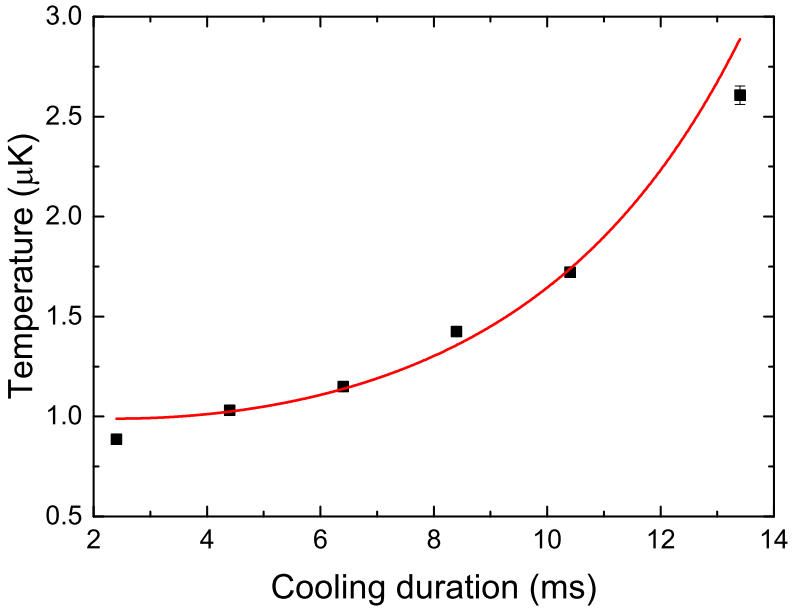

Figure 3.19: The cooling temperature as a function of the duration of Raman sideband cooling. The power and detuning of the optical pumping field are 1 mW and +20 MHz, respectively; the power of the lattice field is 47 mW per beam; and the temperature is measured with y-axis profile. In the theoretical fit, the vibrational frequency ω_{vib} is set as a function of the cooling duration due to the escape of atoms from the dipole trap on z-axis.

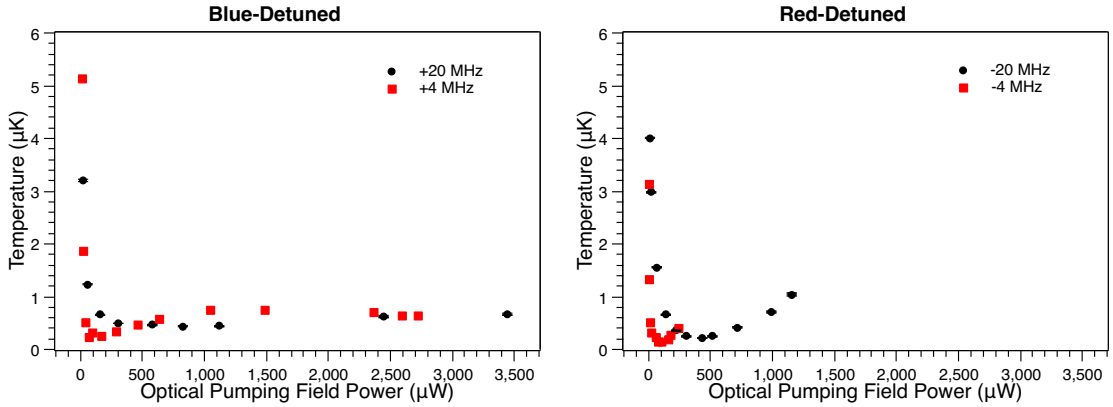

Figure 3.20: The cooling temperature as a function of the power of the optical pumping field with different detunings. The power of the lattice field is 47 mW per beam; the cooling duration is 2.4 ms and the temperature is measured with y-axis profile.

was not dark, which caused the atomic ensemble being blown away. Because the optimized final temperatures did not depend on the detuning of the optical pumping field, the larger blue detuning (+20 MHz) and higher power (1 mW) were chosen in our experiment for the lower power sensitivity.

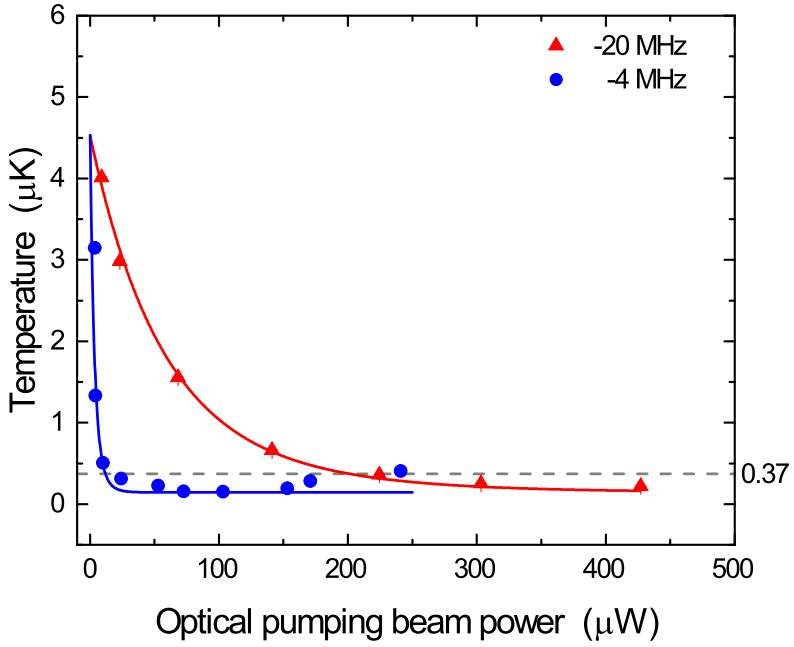

Figure 3.21: The cooling temperature is a function of the optical pumping power in the low power range of Fig. 3.20 with -4 and -20 MHz detuning from $|F = 3\rangle \rightarrow |F' = 2\rangle$. The solid lines are the corresponding fitting curves based on Eqs. 3.37 and 3.38.

Figure 3.22 shows the cooling temperature as a function of the lattice power. In this experiment, the power and the detuning of the optical pumping field were 1 mW and +20 MHz, respectively. The cooling duration was 2.4 ms, and the z-axis magnetic field was optimized for different vibrational level spacings ω_{vib}. The lattice power was converted to Lamb-Dicke parameter η (see Eqs. 3.24, 3.25 and 3.30) for the curve fitting. The heating effect increased with the decreasing lattice power (increasing η), so the temperature would increase shown in our theoretical model. The temperature difference between x and y axes came from the imperfect alignment of the lattice beams, so the vibrational energies in different axes were not degenerate, which caused the difference of the final temperature. The ground state

temperature was calculated from the zero-point energy of the harmonic oscillator model, and we can see that the experimental temperature started to approach the ground state temperature in the low limit range with $\eta < 0.45$, which meant the population did not completely transfer to the lowest vibrational state ($v = 0$) or the harmonic oscillator model deviated from the lattice band structure in the low power region of the lattice field.

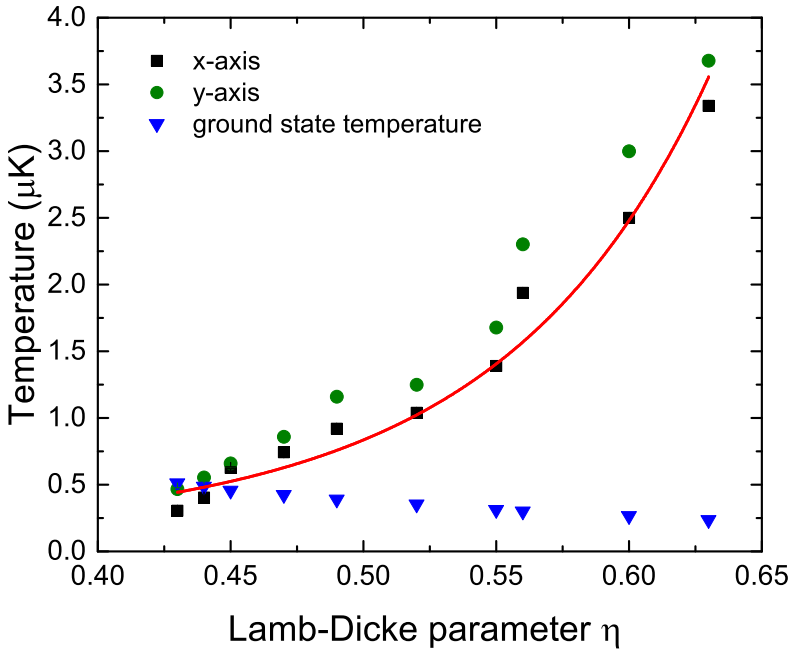

Figure 3.22: The cooling temperature is a function of Lamb-Dicke parameter η. The black squares and the green circles are the temperatures measured with x-axis and y-axis profiles; the red solid line is the theoretical fitting curve of x-axis data; the blue triangles are the calculated ground state temperatures.

The density of the atomic ensemble was estimated by measuring the optical depth (OD) after Raman sideband cooling. A circularly polarised probe beam of 1 μW and 2 μs long, resonant on the D2 line $|F = 3\rangle \rightarrow |F = 4\rangle$, was sent along the quantisation axis direction. We measured the transmission of the probe beam and obtained $OD = 7(2)$. Combining the size of the ensemble $L = 0.7(2)$ mm in the z-direction, we calculated the number density of atoms $n = 8.0(3) \times 10^{10}$ cm^{-3} after Raman sideband cooling with $OD = \sigma n L$, where σ is the resonant cross section for isotropic light polarisation. The corresponding phase-space density $n\lambda_{dB}^3$ is about

1/581, where λ_{dB} is the thermal de Broglie wavelength. The final temperature is consistently around the recoil temperature $T_R = 370$ nK, and the number of atoms after cooling are $1.4(2) \times 10^7$. It can be extended to three-dimensional cooling by adding another lattice beam in the z-axis. This performance will be the foundation for our further experiments, e.g. Bloch oscillation in Chapter 4.

References

[1] A. D. Cronin, J. Schmiedmayer, and D. E. Pritchard. Optics and Interferometry with Atoms and Molecules. *Rev. Mod. Phys.*, 81(3):1051–1129, July-September 2009.

[2] K. Moler, D. S.Weiss, M. Kasevich, and S. Chu. Theoretical Analysis of Velocity-selective Raman Transitions. *Phys. Rev. A*, 45(1):342–348, January 1992.

[3] H. J. Lee, C. S. Adams, M. Kasevich, and S. Chu. Raman Cooling of Atoms in an Optical Dipole Trap. *Phys. Rev. Lett.*, 76(15):2658–2661, April 1996.

[4] K. B. Davis, M.-O. Mewes, M. A. Joffe, M. R. Andrews, and W. Ketterle. Evaporative Cooling of Sodium Atoms. *Phys. Rev. Lett.*, 74(26):5202–5205, June 1995.

[5] W. Petrich, M. H. Anderson, J. R. Ensher, and E. A. Cornell. Stable, Tightly Confining Magnetic Trap for Evaporative Cooling of Neutral Atoms. *Phys. Rev. Lett.*, 74(17):3352–3355, April 1995.

[6] F. Diedrich, J. C. Bergquist, W. M. Itano, and D. J. Wineland. Laser Cooling to the Zero-point Energy of Motion. *Phys. Rev. Lett.*, 62(4):403–406, January 1989.

[7] M. F. Parsons, F. Huber, A. Mazurenko, C. S. Chiu, and W. Setiawan. Site-resolved Imaging of Fermionic ^{6}Li in an Optical Lattice. *Phys. Rev. Lett.*, 114(21):213002, May 2015.

[8] M. Grobner, P. Weinmann, E. Kirilov, and H.-C. Nagerl. Degenerate Raman Sideband Cooling of ^{39}K. *Phys. Rev. A*, 95(3):033412, March 2017.

[9] J. Hu, A. Urvoy, Z. Vendeiro, V. Crépel, W. Chen, and V. Vuletić. Creation of a Bose-condensed gas of ^{87}Rb by laser cooling. *Science*, 358(6366):1078–1080, November 2017.

[10] J. D. Thompson, T. G. Tiecke, A. S. Zibrov, V. Vuletic, and M. D. Lukin. Coherence and Raman Sideband Cooling of a Single Atom in an Optical Tweezer. *Phys. Rev. Lett.*, 110(13):133001, March 2013.

[11] A. M. Kaufman, B. J. Lester, and C. A. Regal. Cooling a Single Atom in an Optical Tweezer to Its Quantum Ground State. *Phys. Rev. X*, 2(4):041014, November 2012.

[12] V. Vuletic, C. Chin, A. J. Kerman, and S. Chu. Degenerate Raman Sideband Cooling of Trapped Cesium Atoms at Very High Atomic Densities. *Phys. Rev. Lett.*, 81(26):5768–5771, December 1998.

[13] H. Perrin, A. Kuhn, I. Bouchoule, and C. Salomon. Sideband Cooling of Neutral Atoms in a Far-detuned Optical Lattice. *Eur. Phys. Lett.*, 42(4):395–400, May 1998.

[14] S. E. Hamann, D. L. Haycock, G. Klose, P. H. Pax, I. H. Deutsch, and P. S. Jessen. Resolved-sideband Raman Cooling to the Ground State of an Optical Lattice. *Phys. Rev. Lett.*, 80(19):4149–4152, May 1998.

[15] A. J. Kerman, V. Vuletic, C. Chin, and S. Chu. Beyond Optical Molasses: 3D Raman Sideband Cooling of Atomic Cesium to High Phase-space Density. *Phys. Rev. Lett.*, 84(3):439–442, January 2000.

[16] D.-J. Han, S. Wolf, S. Oliver, C. McCormick, M. T. DePue, and D. S. Weiss. 3D Raman Sideband Cooling of Cesium Atoms at High Density. *Phys. Rev. Lett.*, 85(4):724–727, July 2000.

[17] S. J. J. M. F. Kokkelmans, B. J. Verhaar, K. Gibble, and D. J. Heinzen. Predictions for Laser-cooled Rb Clocks. *Phys. Rev. A*, 56(6):R4389–R4392, December 1997.

[18] C. Huang, P.-C. Kuan, and S.-Y. Lan. Laser Cooling of ^{85}Rb Atoms to the Recoil-temperature Limit. *Phys. Rev. A*, 97:023403, February 2018.

[19] C. J. Foot. *Atomic Physics*. Oxford, 2005.

[20] S. Pancharatnam. Light Shifts in Semiclassical Dispersion Theory. *J. Opt. Soc. Am.*, 56:1636, 1966.

[21] N. B. Delone and V. P. Krainov. AC Stark Shift of Atomic Energy Levels. *Physics-Uspekhi*, 42(7):669–688, 1999.

[22] A. Khadjavit and A. Lurio. Stark Effect in the Excited States of Rb, Cs, Cd, and Hg. *Phys. Rev.*, 167(1):128–135, March 1968.

[23] C. Cohen-Tannoudji and J. Dupont-Roc. Experimental Study of Zeeman Light Shifts in Weak Magnetic Fields. *Phys. Rev. A*, 5(2):968–984, February 1972.

[24] C. Y. Park, H. Noh, C. M. Lee, and D. Cho. Measurement of the Zeeman-like AC Stark shift. *Phys. Rev. A*, 63:032512, 2001.

[25] D. Cho. Vector and Tensor Transition Polarizabilities between the $6S_{1/2}$ and $5D_{3/2}$ States of the Cesium Atom. *J. Korean Phys. Soc.*, 29(3):300–304, June 1996.

[26] F. L. Kien, P. Schneeweiss, and A. Rauschenbeutel. Dynamical Polarizability of Atoms in Arbitrary Light Fields: General Theory and Application to Cesium. *Eur. Phys. J. D*, 67:92, 2013.

[27] I. H. Deutsch and P. S. Jessen. Quantum-state Control in Optical Lattices. *Phys. Rev. A*, 57(3):1972–1986, March 1998.

[28] M. Fox. *Optical Properties of Solids*. Oxford, 2nd edition, 2010.

[29] G. H. Duffey. *Applied Group Theory for Physicists and Chemists*. Dover, 2015.

[30] K. I. Petsas, A. B. Coates, and G. Grynberg. Crystallography of Optical Lattices. *Phys. Rev. A*, 50(6):5173–5189, December 1994.

[31] D. J. Wineland, C. Monroe, W. M. Itano, D. Leibfried, B. E. King, and D. M. Meekhof. Experimental Issues in Coherent Quantum-state Manipulation of Trapped Atomic Ions. *J. Res. Natl. Inst. Stand. Technol.*, 103(3):259–328, May 1998.

[32] A. V. Taichenachev, A. M. Tumaikin, and V. I. Yudin. Two-dimensional Sideband Raman Cooling and Zeeman-state Preparation in an Optical Lattice. *Phys. Rev. A*, 63:033402, 2001.

[33] A. Kastberg, W. D. Phillips, S. L. Rolston, and R. J. C. Spreeuw. Adiabatic Cooling of Cesium to 700 nK in an Optical Lattice. *Phys. Rev. Lett.*, 74(9):1542–1545, February 1995.

[34] N. B. L. Forster, W. Alt, A. Widera, D. Meschede, and A. Alberti. Microwave Control of Atomic Motional States in a Spin-dependent Optical Lattice. *J. Phys. B: At. Mol. Opt. Phys.*, 46:104006, May 2013.

Chapter 4

Motion Sensing in Periodic Potential

In Chapter 2, a new measuring method using the EIT-enhanced light dragging effect is introduced. In that experiment, the atomic ensemble moved in a free space, driven by momentum kicks from the push field. After that, we focused on the collective behaviour of atoms in a driven periodic potential. In particular, we investigated Bloch oscillation of atoms using light-dragging method for the potential applications of the precision measurement of the recoil velocity in the driven potential, and studied the topological phases of the spin wave in the moving medium.

Bloch oscillation is a pure quantum phenomenon, "anticipated" by Felix Bloch in 1929 [1]. The basic idea is that, when a particle in a lattice is applied by an inertial force, its velocity will oscillate, rather than a monotonic increase. From the research of the electrical conductivity of the solid lattice, Bloch found that the microscopic behaviour of electrons does not simply follow the classical electromagnetism equation: $\mathbf{J} = \sigma\mathbf{E}$, where $\mathbf{J}$ is the current density, σ is the electrical conductivity, and $\mathbf{E}$ is the external electric field. He predicted the oscillatory behaviour based on the derivation from quantum theories. Unfortunately, this phenomenon could not be demonstrated and observed in a normal solid system, because the Bloch oscillation period was much longer than the defect scattering period in a solid lattice. For example, the concentration of the lattice vacancy defects of FCC (face centered cubic) copper in the room temperature is about 10^{-14} [2], and the relaxation (collision) time of an electron is about 10^{-15} s [3], so the vacancy defect scattering period is about 100 ms. Considering the effect of other defects, Bloch oscillation period must

be longer than the defect scattering period. According to the second law of thermodynamics, to minimize the Gibb's free energy of the production of the solid lattice, the defects (e.g. vacancies, dislocations [4], interstitial sites [5], grain boundaries and many kinds of impurities) naturally exist in all solid matters, as Fig. 4.1 illustrates. The concentration of them in the room temperature can be large, no matter which crystal is. When an electron moves in a solid lattice, it would be scattered or deflected by an asymmetric surrounding particles, which is caused by any of defects. Therefore, the oscillation behaviour is hard to be observed.

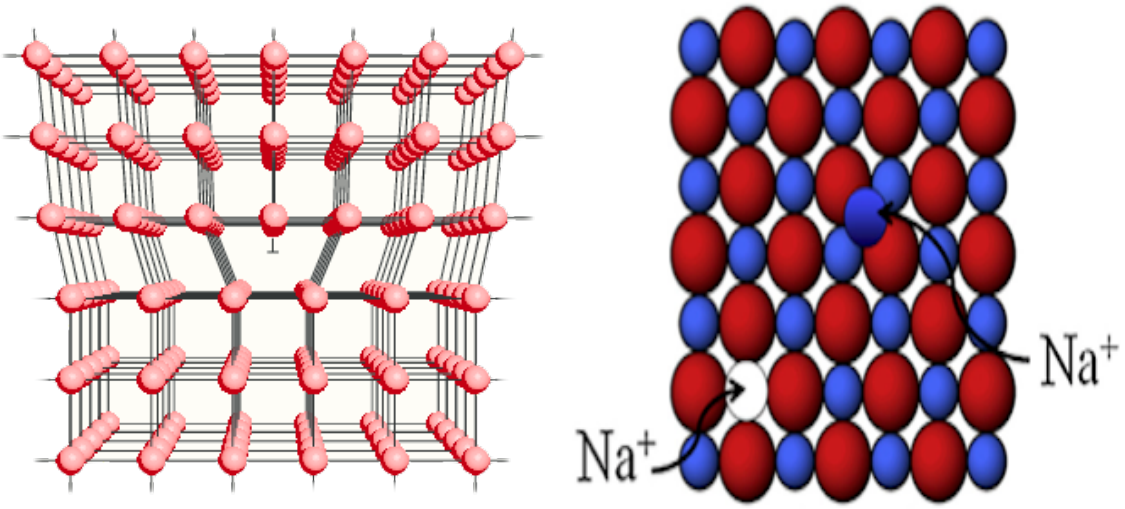

Figure 4.1: *Left*: dislocation defect in a crystal [4]; *Right*: an interstitial defect and a vacancy of a sodium atom co-exist to balance the charge neutrality in an ionic crystal [5].

In 1993, Waschke *et al.* observed Bloch oscillation in a semiconductor crystal by detecting the radiation emitted by electrons [6]. With the help of the superlattice structure, the oscillation period could be 600 fs, much shorter than that in the metal, which made the possibility of the completion of the oscillation. Compared with the challenges in a real lattice, there are some inherent advantages for the optical lattice: 1. the optical lattice is created by the light field, so it can be turned on or off in any time; 2. the optical lattice is a perfect lattice without any defect of the real lattice, so atoms have a long lifetime to complete the oscillation; 3. the lattice vectors (base vectors in k-space, see Section 3.1.1.2) $\mathbf{a}_i^*$ are well defined, so it is easy to modify

and analyse the behaviours of atoms in this artificial structure. In Chapter 3, we introduce Raman sideband cooling to cool down atoms to the recoil temperature. In this chapter, the detail of Bloch oscillation after Raman sideband cooling will be discussed.

4.1 Bloch Oscillation

Bloch "oscillation" sounds like a classical motional behaviour of particles, but it is truly a pure quantum phenomenon, which verifies the wave-particle duality of the matter. Here, atoms (or other particles) are treated as matter waves and interact with a periodic structure with the wave nature. When atoms are accelerated by some external force, their average momentum (wavevector) would linearly increase up to a critical value, e.g. the half of the lattice vector $\mathbf{a}_i^*$ in the first Brillouin zone, and then reflect with the reversed momentum. For Bloch oscillation in a 1D optical lattice, the oscillation amplitude is not determined by the physical distance between lattice planes, and the oscillation period is not a function of the lattice trapping potential. To explain Bloch oscillation in an optical lattice, two pictures: moving lattice picture and quantum optics picture are used.

4.1.1 Moving Lattice Picture

In the theoretical frame of solid state physics, the Hamiltonian of the particle in a 1D periodic potential is:

$$\widehat{H}_M = \frac{\widehat{p}_M^2}{2M} + \widehat{U}(z). \tag{4.1}$$

Equation 4.1 neglects the internal motion of the electrons in the atom, where $\widehat{p}_M$ is the momentum of the center of mass of the atom; M is the mass of the atom; $\widehat{U}(z)$ is the periodic potential created by the optical lattice, with the same definition as Eq. 3.18, which is a function of the position on z-axis. Based on Bloch theorem, the wave function Ψ of an atom in a lattice can be written as:

$$\Psi_{n,q}(z) = e^{iqz} u_{n,q}(z), \tag{4.2}$$

where n is a discrete quantum number of the lattice energy bands; q is a continuous

quasi-momentum of the atom, which is the momentum conserved within the lattice vector $\big(q = p_M^* + Na_i^*$, where p_M^* is the real momentum of the atom with the average velocity $\langle v\rangle$ ($\langle v\rangle = \hbar^{-1}(\mathrm{d}E/\mathrm{d}q)$) and the effective mass M^* in the lattice $\big(M^* = \hbar^2(\mathrm{d}^2E/\mathrm{d}q^2)^{-1}\big)$; N is any integer; a_i^* is the absolute value of the lattice vector; E is the total energy of the atom in the lattice$\big)$. In addition, $u_{n,q}(z)$ is the periodic wavepacket function corresponding to the lattice structure and the intrinsic properties of the atom; $\Psi_{n,q}(z)$ is also called Bloch state, which describes how the matter wave of the atom distributes in the lattice, such as a plane wave $exp(iqz)$ with some specific waveform $u_{n,q}(z)$. In Section 3.1.1.1, we assume that the radial trapping is uniform because of the large size of our lattice light beams, which well supports the approximation of the atomic plan wave in the axial direction. To accelerate atoms, an external force F is applied on the atom, so the quasi-momentum q and atomic wavepacket function $u_{n,q}$ become time-dependent as below:

$$\Psi_{n,q}(z,t) = e^{iq(t)z}u_{n,q}(z,t) \tag{4.3}$$

$$q(t) = q(0) + \frac{Ft}{\hbar}. \tag{4.4}$$

Equation 4.4 describes the linear increase of the atomic quasi-momentum $q(t)$ under a constant external force F. However, an atom is electrically neutral, so the external electric field does not work in this case. Instead, a moving lattice is implemented to accelerate cold atoms for Bloch oscillation. In Fig. 4.2, when the atom starts to interact with two lattice fields, the frequency detuning between the two fields provides an initial velocity v of the atom. However, the light fields with different frequencies cannot construct a standing wave (optical lattice) in the lab frame, so it is necessary to consider this configuration in the moving frame of the atom. Based on the first order of Doppler effect, moving atoms actually experience the light field with a frequency shift $\mathbf{k}\cdot\mathbf{v}$, which is kv in 1D case as shown in Eqs. 4.5 - 4.7, where $\mathbf{k}$ is the wavevector of the lattice field.

$$\omega_1 - k_1 v = \omega_2 + k_2 v \tag{4.5}$$

$$v = \frac{\Delta\omega}{2k} \quad (\Delta\omega = \omega_1 - \omega_2) \tag{4.6}$$

$$a = \frac{d}{dt}(\frac{\Delta\omega}{2k}) = \frac{\Delta\dot{\omega}}{2k}. \tag{4.7}$$

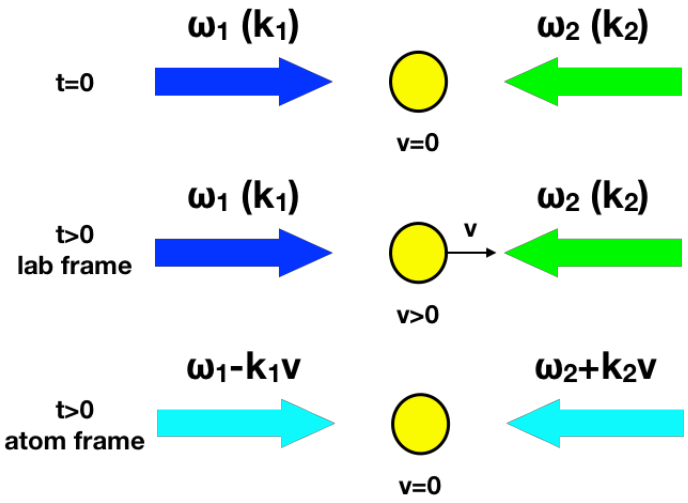

Figure 4.2: An atom experiences a moving lattice in its frame with the detuning between two lattice fields ($\omega_1 > \omega_2$).

Equation 4.5 shows the condition of the moving lattice. Under the approximation $k_1 \approx k_2 = k$, the velocity of the moving lattice is equal to the velocity of the atom, as shown in Eq. 4.6. Because the velocity of the atom can be controlled by the detuning between two lattice fields, it is possible to tune the acceleration of the atom's velocity as well. Equation 4.7 shows the correlation between the acceleration a and the change of the frequency $\Delta\dot{\omega}$. If the detuning $\Delta\omega$ is linearly ramped up, the external force F caused by the moving lattice is a constant value ($F = -Ma$) and the quasi-momentum $q(t)$ in Eq. 4.4 would linearly increase over time.

In the moving lattice, the band structure is the same as the static lattice. Figure 4.3 shows the difference between the free particle case and the lattice case in the first Brillouin zone [7]. The energy E of free particles is a parabolic function of the momentum p ($E = p^2/2M$), so there is no inflection and the possibility to oscillate. Based on Bloch theorem, when atoms distribute in a periodic potential, the lattice potential interacts with the atoms periodically, and finally produce allowed energy bands and forbidden energy gaps. As (b) in Fig. 4.3 [7], we can see the quasi-momentum span is from $-\pi/d$ to π/d, and there are some band gaps near the Brillouin zone boundaries ($q = \mp\pi/d$ or $\mp k$) between two energy bands, which plays a key role in Bloch oscillation.

With the band structure and the external force F, the mechanism of Bloch oscillation in the 1D lattice is shown in Fig. 4.4. Initially, the atom is in an inertial

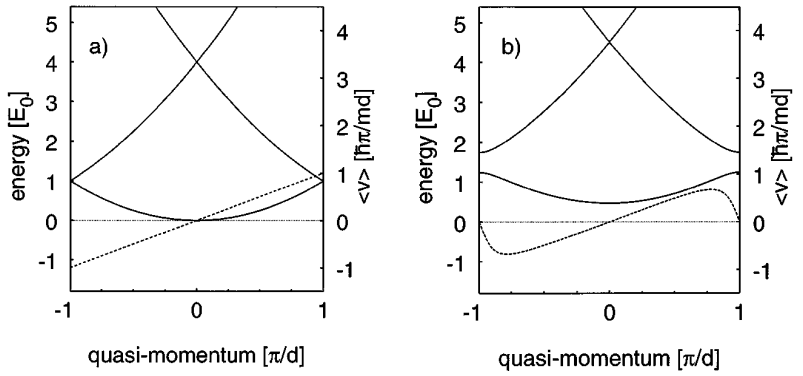

Figure 4.3: The band structure $E_{n,q}$ (solid lines) and the average velocity $\langle v \rangle$ (dash lines) of the atom in a 1D lattice are a function of the quasi-momentum q. E_0 is the recoil energy; d is $\lambda/2$, the spatial period of the lattice. (a) free particle case; (b) optical lattice case, which shows the difference near the periodic zone boundary $q = \pm\pi/d$ from the free particle case in (a) [7].

frame at rest or with a constant velocity v. When the detuning $\Delta\omega$ starts ramping, the atom is applied by a force F, and its quasi-momentum $q(t)$ follows the change over the time. At half of the oscillation period ($\tau_B/2$), the atom reaches the boundary of the Brillouin zone. The zone boundary in the solid state physics is a special region due to the two-way momentum kicks from the lattice vector $\mathbf{a}_i^*$. The same as the boundary ($q = \pm\pi/d$) of the optical lattice case in Fig. 4.3, the average velocity of the atom $\left(\langle v \rangle = \hbar^{-1}(\mathrm{d}E/\mathrm{d}q)\right)$ is 0 and its momentum is not well defined, which mixes $+k$ ($+\pi/d$) and $-k$ ($-\pi/d$) due to the periodicity of the atomic wavefunction in the lattice and the reversible two-photon Raman transition given by the lattice field, which shifts the momentum $+2\hbar k$ or $-2\hbar k$ on the boundary position. At the zone boundary, the atom has two choices: reflecting back by the $2\hbar k$ momentum kicks of two-photon Raman transition or jumping to a higher energy band. The first choice is Bloch oscillation. The second choice causes the loss out of the moving lattice, because Bloch oscillation on the higher energy band involves higher order of multi-photon transitions. However, the probability of such a transition in a higher energy band is much lower than that in the fundamental band. For example, the four-photon transition is required for Bloch oscillation in the first excited band.

The work of Dahan *et al.* in Fig. 4.5 showed the experimental data of the direct observation of Bloch oscillation [7]. The Cs atoms were accelerated by a moving

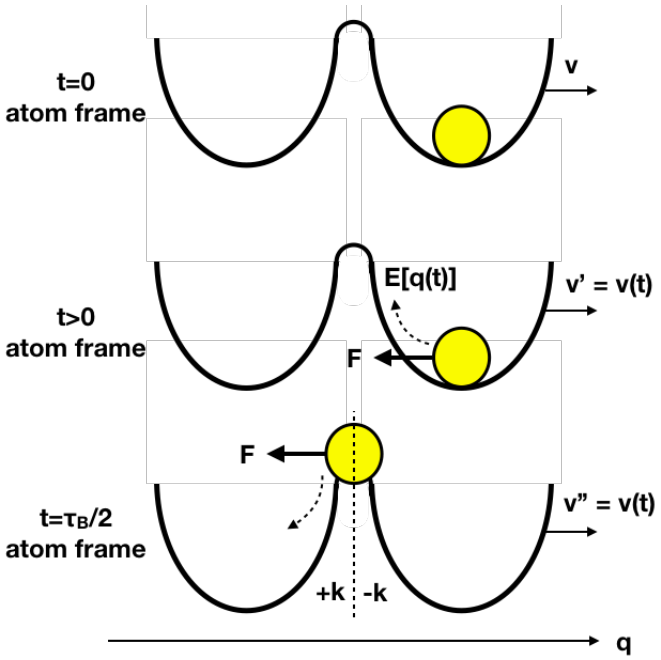

Figure 4.4: The half cycle of Bloch oscillation. τ_B is the period of Bloch oscillation; F is the external force caused by the accelerated frame; $E[q(t)]$ means the atomic energy is a functional of $q(t)$; v' and v" are the velocities at their respective time.

lattice, whose velocity was detected by Raman velocity-selective spectroscopy. In this figure, the average momentum of the atomic ensemble kept increasing up to the zone boundary at the half period $\tau_B/2$, and gradually became a superposition state with the momentum $+k$ and $-k$. After $\tau_B/2$, the momentum with a negative sign $(-k)$ dominated and kept increasing again. Finally the average momentum of atoms returned to the initial value.

In the analysis above, the dynamics of the atom in the moving lattice look similar with the harmonic oscillation in the classical dynamics. However, there are several differences: 1. the curve of the band structure is not a parabolic, sine or cosine function; 2. the external force is a constant value, so Bloch oscillation is not a harmonic oscillation; 3. the oscillation happens in k-space, so the oscillation amplitude is not related to the spatial period d of the lattice. Considering the bandwidth Δ_n ($n = 0$ for the fundamental band), the spatial amplitude A_s can be derived by:

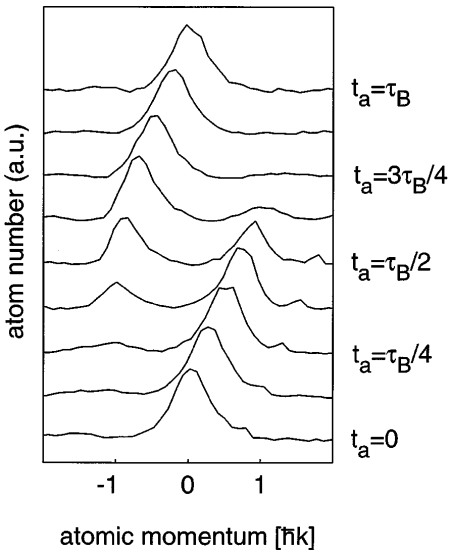

Figure 4.5: The number of atom is a function of the atomic momentum with the time evolution t_a. τ_B is the oscillation period [7].

$$|F| \cdot A_s = \frac{\Delta_n}{2}$$
$$A_s = \frac{\Delta_n}{2|F|}. \tag{4.8}$$

Bandwidth Δ_n is a function of the intensity of the lattice fields, and the force F is proportional to the acceleration a. Both of Δ_n and F can be tuned with the parameters of the laser, but there is no relation with a spatial period ($d = \lambda/2$) of the lattice. Therefore, Bloch oscillation is not a classical oscillating motion by the collision among physical walls. Another important parameter is the oscillation period τ_B. According to Eq. 4.4, the period τ_B could be obtained as:

$$\frac{|F|\tau_B}{\hbar} = \frac{2\pi}{d}$$
$$\tau_B = \frac{h}{|F|d}. \tag{4.9}$$

From Eqs. 4.7 and 4.9, they show the reason why the Bloch oscillation period τ_B of the electrons in the metal could be much longer than the defect scattering period. Assuming the absolute values of the external force F are similar in "electrons in the metal" case and "atoms in the optical lattice" case, the spatial period d shows a

large difference between these two cases. In our optical lattice, d is 390 nm and τ_B is about 0.5 ms. In the metal, however, d is about 0.1 to 0.2 nm, so its τ_B could be much longer than the defect scattering period (100 ms for the vacancy defect scattering only in FCC copper [2, 3]).

4.1.2 Quantum Optics Picture

Compared with the moving lattice picture, the quantum optics picture directly observes the velocity change in the lab frame, rather than in a non-inertial frame. As shown in Fig. 4.6 [8], similar to Bragg diffraction, atoms gain $\hbar(\mathbf{k}_1 - \mathbf{k}_2)$ ($\approx 2\hbar k$) momentum kick and the corresponding kinetic energy from two counter-propagating lattice fields based on momentum conservation and energy conservation.

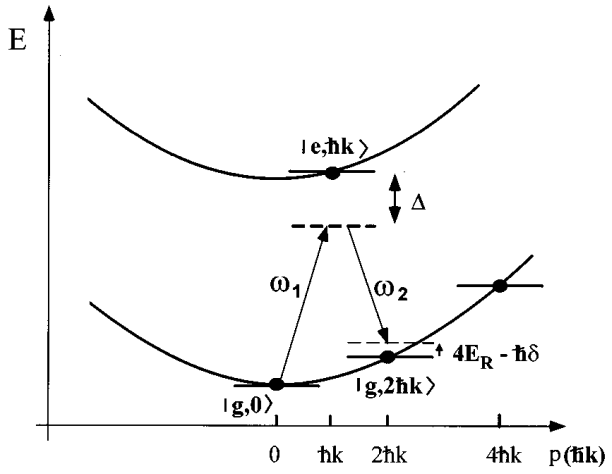

Figure 4.6: The atomic momentum states are transferred by the momentum kicks from two counter-propagating lattice fields. $|g, 0\rangle$ is the initial momentum state on the fundamental (ground) band; $|e, (2j+1)\hbar k\rangle$ is the excited state (j is a positive integer or 0); Δ and δ are the single- and two-photon detuning of the two-photon Raman transition, respectively [8].

When the frequency difference between two counter-propagating fields is increased linearly, the atom receives the $2\hbar k$ momentum kick in each momentum transfer cycle at some discrete point. As a result, the total momentum change of the atom is $2j\hbar k$, where j is the index number of the transfer cycle. Accompanying the momentum transfer, the kinetic energy of the atom also increases to $4j^2 E_R$

$\big((2j\hbar k)^2/2M = 4j^2E_R$, where E_R is the recoil energy for the lattice field$\big)$, which means that the energy $4(2j+1)E_R$ $\big(4((j+1)^2-j^2)E_R\big)$ would be added to the atom from jth to $(j+1)$th cycle. However, the energy increase relies on the two-photon Raman transition, so the given energy in the cycle might be not enough if the frequency difference between two lattice fields is not tuned to some specific value to match the energy gap $4(2j+1)E_R$. In the experimental data of Peik *et al.* shown in Fig. 4.7 [8], the energy non-conservation in the process caused that the momentum transfers in most of the cycles failed (see the plateaus in the figure). The transfer only worked in the narrow ranges of the frequency difference of two lattice fields and the theoretical energy gap (see the rising slopes in the figure). The momentum (velocity) of the atom was therefore increased stepwise rather than linearly. Additionally, because the energy gap $4(2j+1)E_R$ was linearly boosted, if the detuning between two lattice fields was also linearly ramped ($\Delta\dot{\omega}$ is a constant), the stepwise rising of the velocity in Fig. 4.7 had a constant period, which totally agreed with the conclusion of the oscillation period τ_B in the moving lattice picture (see Eq. 4.9), because of the constant external force F.

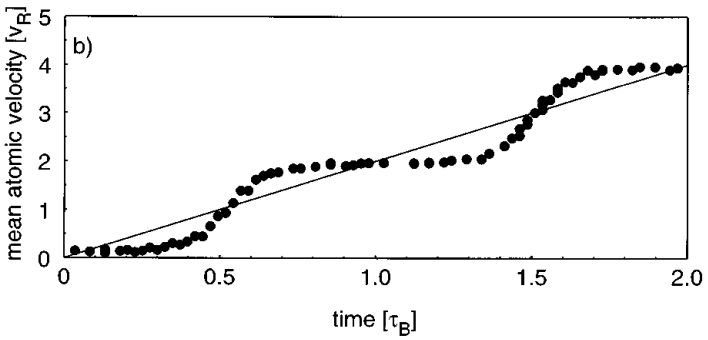

Figure 4.7: The mean velocity of the atomic ensemble is a function of time during Bloch oscillation process. The dots and the solid line are the measured data and the theoretical velocity of the moving lattice, respectively [8].

The experimental result in Fig. 4.7 was measured in the lab frame, but it showed the same oscillatory behaviour of the atom in an accelerated frame. Assuming an periodic function v_2 as the velocity of an atom in the accelerated frame, and a linear function v_1 as the velocity of the moving lattice in the lab frame, the total velocity v_{total} of the atom in the lab frame can be calculated with $v_1 + v_2$. Equations 4.10

- 4.12 are plotted in Fig. 4.8, where a is the acceleration, defined in Eq. 4.7, A_v is the amplitude of the atom's velocity in accelerated frame, which is proportional to the band width Δ_n, and Ω_B is the angular frequency of Bloch oscillation. Eq. 4.12 qualitatively matches the experimental data in Fig. 4.7, which allows us to decompose the total velocity function into two parts: v_1 for the moving lattice and v_2 for the atom inside of the moving lattice, which shows the same behaviour of Bloch oscillation as the conclusion in the moving lattice picture.

$$v_1 = at \tag{4.10}$$

$$v_2 = A_v \sin\left(\Omega_B(t + 0.2\pi) + 0.5\sin(\Omega_B(t + 0.2\pi))\right) \tag{4.11}$$

$$v_{\text{total}} = v_1 + v_2. \tag{4.12}$$

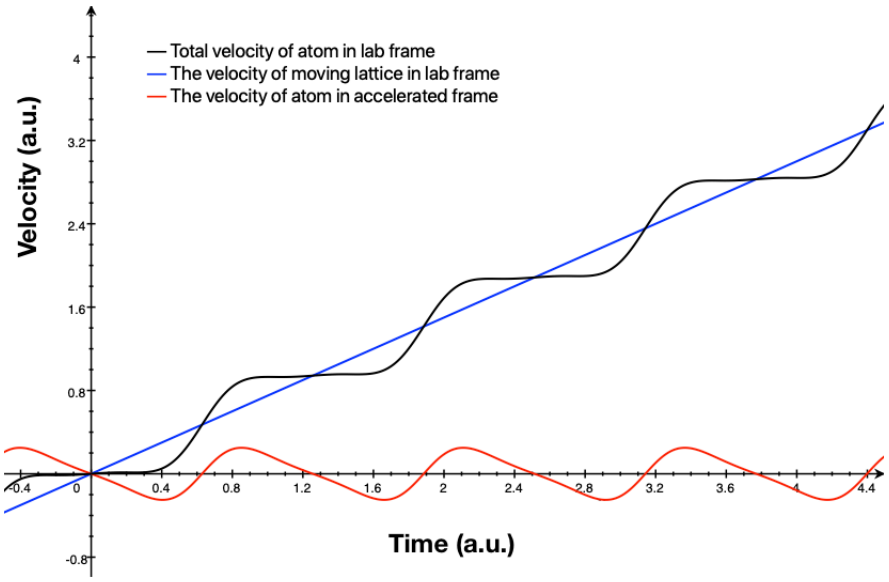

Figure 4.8: The plot of Eq. 4.10 (blue line), 4.11 (red line) and 4.12 (black line) with a=0.75; A_v=0.25; Ω_B=5.

As mentioned in Section 4.1.1, the band structure of the lattice is not a simple sine or cosine function of the quasi-momentum q, and the average velocity $\langle v \rangle$ could be calculated by:

$$\langle v \rangle(q) = \frac{1}{\hbar}\frac{dE_n(q)}{dq}. \tag{4.13}$$

Based on Eq. 4.13, the velocity function is not a sine or cosine periodic function. Equation 4.11 mimics the velocity curve in Fig. 4.11 [7, 8] to simplify the mathematical function for the qualitative analysis. The real simulation data will be shown in Section 4.3.1.

4.1.3 Oscillation Efficiency

From Sections 4.1.1 and 4.1.2, we can see that the efficiency of Bloch oscillation is mainly determined by the two-photon Raman transitions. In the moving lattice picture, the Raman transition needs to work at each zone boundary (see Fig. 4.4), if the atom jumps to a higher energy band, it would not follow the motion of the lattice anymore, and its oscillation behaviour would stop as shown in Fig. 4.9 [9]. In the quantum optics picture, once the atom misses the Raman transition with the specific frequency difference $4(2j+1)E_R$, it would miss $2\hbar k$ momentum kick, which means its velocity would remian unchanged.

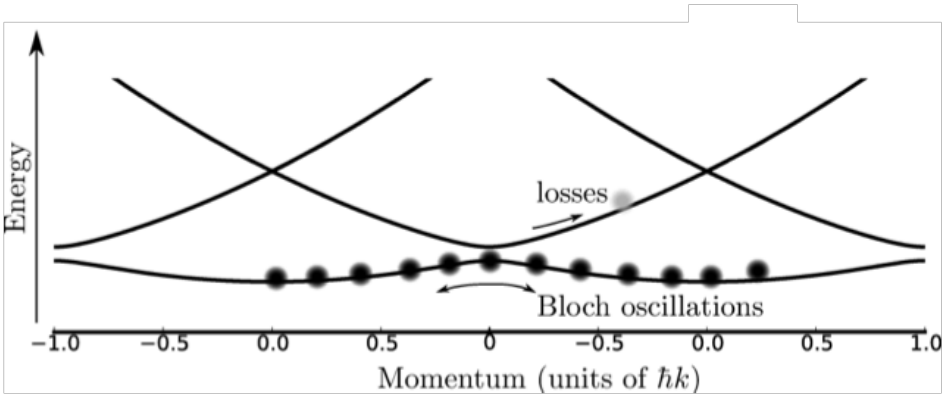

Figure 4.9: The energy band structure of an atom. When the atom reaches the zone boundary, there are two routes: 1. staying in the fundamental band, which is Bloch oscillation; 2. jumping to the higher energy band, which is the loss out of the moving lattice [9].

From the above discussions and Fig. 4.9, the loss to the higher order bands determines the efficiency of Bloch oscillation. The source of the losses is called Landau-Zener tunnelling effect. The tunneling rate r is given by [10]:

$$r = exp(-\frac{\Delta E_{ge}^2/4\hbar}{|\frac{d}{dt}(E_e - E_g)|}), \tag{4.14}$$

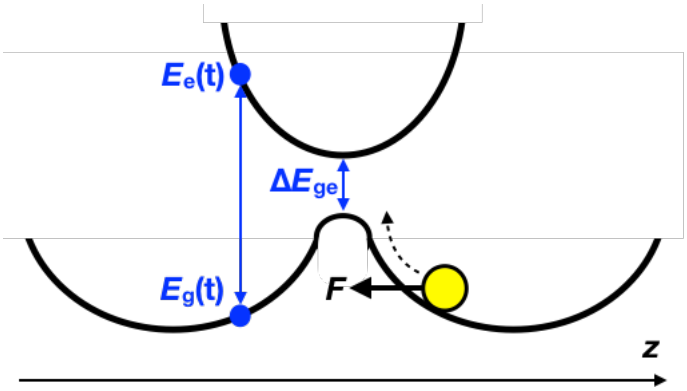

Figure 4.10: The diagram of the parameters ΔE_{ge} and $E_{g,e}$ in Eq. 4.14. The detail is explained in the text.

where ΔE_{ge} is the energy gap between the fundamental band and the first higher order band at the crosspoint of two potential wells; $E_{g,e}$ is the energy of the ground (g) or the excited (e) state, which is a function of time because the atom is accelerated, as shown in Fig. 4.10. Equation 4.14 shows the tunnelling rate increases when the energy gap at the crosspoint is smaller, the slopes (absolute values) of the potential curves are larger, or the atomic acceleration (the external force F) is higher. The energy gap and the curve slope depend on the total potential depth U_0. So Eq. 4.14 can be converted to another form, as shown in Eq. 4.15 for the analysis of Bloch oscillation [8, 9]:

$$r = exp(-\frac{a_c}{a}) \tag{4.15}$$

$$\frac{a_c}{a} = \frac{\pi\Omega^2}{2\Delta\dot{\omega}} \propto (\frac{U_0}{E_R})^2 \tag{4.16}$$

$$\Omega = \frac{\Omega_1\Omega_2}{2\Delta} = \frac{U_0}{2\hbar}, \tag{4.17}$$

where a and a_c are the acceleration in Eq. 4.7 and the critical acceleration, respectively, Ω and $\Omega_{1,2}$ are the Rabi frequencies of the Raman transition and the single lattice beam 1 or 2 in Fig. 4.2, respectively, and Δ is the single-photon detuning, the same as that in Fig. 4.6, and U_0 is the potential depth of $U(z)$ in Eq. 4.1.

Landau-Zener tunnelling effect describes the probability of the non-adiabatic transfer of the population from one energy band to anther one. Here, we would discuss two tunable parameters: the potential depth U_0 and the external force F, to improve the efficiency of Bloch oscillation.

Based on the Fourier transform, a higher potential depth corresponds to a narrower band width Δ_n and a smaller velocity range in k-space as shown in the experimental data of Dahan *et al.* in Fig. 4.11 [7, 8]. A higher potential depth could efficiently reduce the tunnelling rate to higher energy bands, because the band gap becomes larger and the atomic velocity becomes lower, as shown in Eqs. 4.14 - 4.16. However, Landau-Zener formula makes some approximation in the derivation, so it is valid in weak-binding limit only ($U_0 \leq 20E_R$, where E_R is the recoil energy, defined in Eq. 1.11). The efficiency does not change after the potential depth is higher than $20E_R$, so the magnitude of the external force F dominates in tight-binding limit.

The efficiency increased by a deep potential well looks helpful for the experiment, however, the narrow band width and velocity range would cause a small oscillation amplitude as shown in Eq. 4.8. Therefore, it is efficient to push the atomic ensemble in some direction, but also increases the difficulty to observe the oscillation behaviour, so it is not suitable for our experiment because we tend to measure the recoil velocity v_R. The same argument can be also explained in the quantum optics picture, where the total velocity simulation of Fig. 4.8 would show smaller deviations from the straight line of the lattice velocity when the lattice field is more intense. The reason is that, when the lattice field intensity increases, the scattering rates of the off-resonant Raman transitions also increase, so the total velocity would be closer to a linear function of time. As a result, the oscillation behaviour is difficult to observe in this configuration.

The external force of Bloch oscillation is proportional to the acceleration a of the moving lattice and the frequency ramping rate $\Delta\dot{\omega}$. A stronger force could make a higher probability to drive atoms jump to higher energy band, consistent with the varied tendencies in Eqs. 4.14 and 4.15. Because the external force F is inversely proportional to the oscillation period τ_B as shown in Eq. 4.9, the experimental data and the simulation of Cladé *et al.* in Fig. 4.12 showed the efficiency as the function of the oscillation period [9].

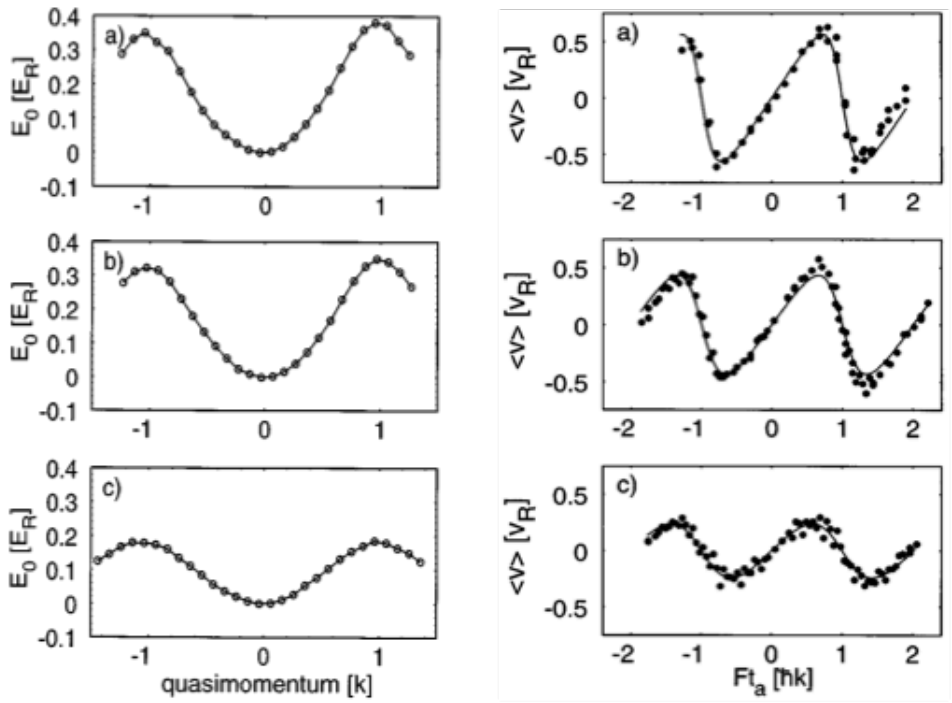

Figure 4.11: *Left*: the band structure of Cs atoms (in unit of the recoil energy E_R) as a function of the quasi-momentum; *Right*: the atomic mean velocity (in unit of the recoil velocity v_R) as a function of time-variable quasi-momentum Ft_a for three different values of the potential depth: (a) $U_0 = 1.4\ E_R$; (b) $U_0 = 2.3\ E_R$; (c) $U_0 = 4.4\ E_R$ [7, 8].

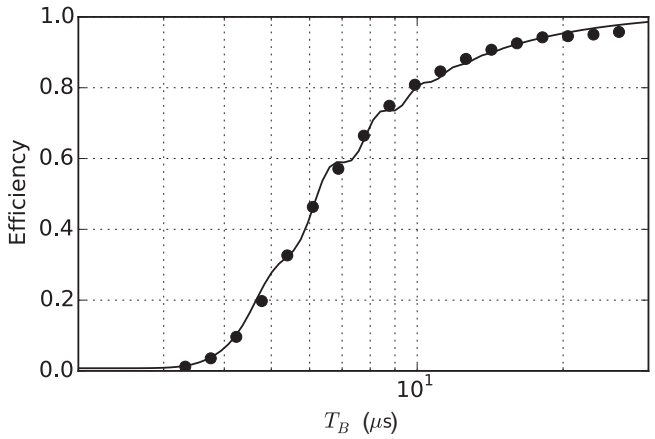

Figure 4.12: The efficiency of 20 Bloch oscillations as a function of the oscillation period (T_B in Reference [9]) The dots and the solid line are experimental data and the simulation, respectively; the potential depth U_0 is $40E_R$ [9].

Bloch oscillation is a kind of adiabatic transitions, so a weaker force could help achieve a higher efficiency of this process. If the force is weak enough not to induce the internal transitions among energy bands, it needs to satisfy the adiabatic criterion:

$$|\langle u_{n',q}|\frac{d}{dt}|u_{n,q}\rangle| \ll \frac{|E_{n'}(q) - E_n(q)|}{\hbar} \quad (n' \neq n), \tag{4.18}$$

where $u_{n,q}$ is the wavepacket function of Bloch state, as defined in Eq. 4.2. For the case $U_0 \leq 10E_R$, Eq. 4.18 shows the condition $|Mad| \ll (\pi/8)U_0^2/E_R$ ($d = \lambda/2$, which is the spatial period of the lattice), which is easier to be satisfied in a deeper potential well and a small external force [8]. The adiabaticity could be improved with a reduced force as shown in Fig. 4.12, but it is not an ideal strategy to choose a long oscillation period in the experiment due to the system stability and coherence concerns. Therefore, there are two more ways to improve the adiabaticity, one is to tune the frequency ramping rates adabatically, and the other is to tune relative phases of two lattice fields in the beginning and ending stages of the frequency ramping, both of which improvement methods are discussed in Reference [9]. In this experiment, we optimize the potential depth U_0 and the acceleration a to $7E_R$ and 30 m/s^2, respectively, which satisfy the adiabatic criterion in Eq. 4.18.

4.2 Experimental Setup

4.2.1 Optical Setup

Figure 4.13 shows the optical setup for EIT measurement with Bloch oscillation. Because the precooling of Raman sideband cooling is necessary to achieve efficient Bloch oscillation, the optical setup was built on the foundation of Raman sideband cooling alignment as described in Section 3.2.2. Other optical components for the 1D optical lattice of Bloch oscillation and EIT phase measurement were then added. The lattice field for Bloch oscillation shared the same light source with the lattice field for Raman sideband cooling. The setup for frequency ramping of the lattice field for Bloch oscillation is shown in Fig. 4.14. The lattice beam was separated into two parts, both of which double-passed two independent AOMs with driving frequency f_1 and f_2, and then returned to the original optical paths and were coupled

into an optical fibre. Frequency f_1 was ramped from 80 MHz, and frequency f_2 was fixed at 80 MHz.

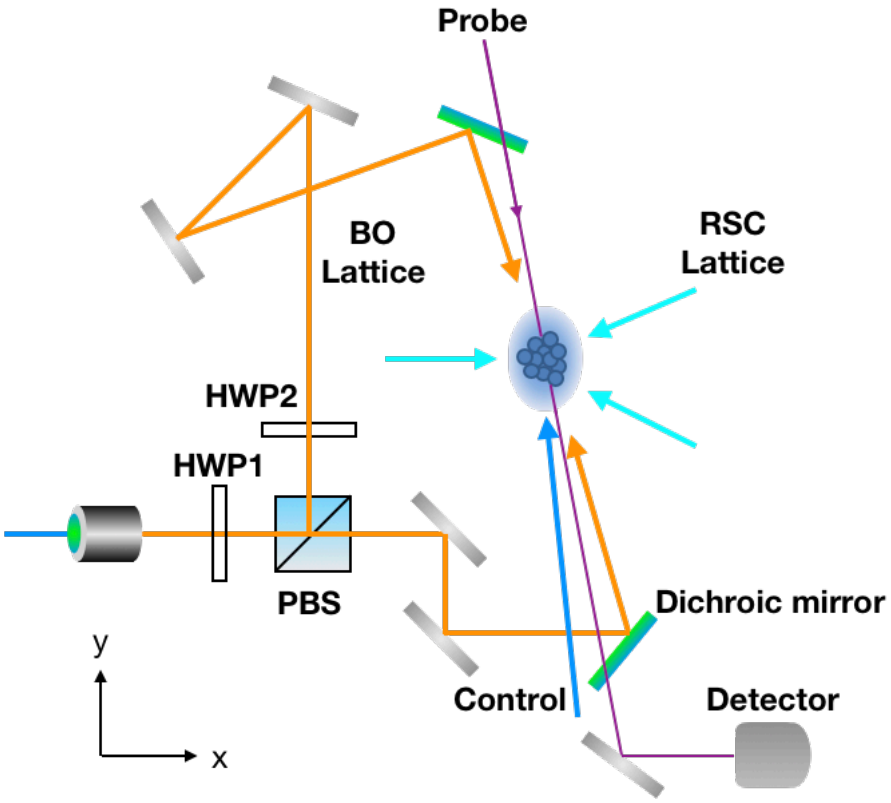

Figure 4.13: The optical setup for EIT measurement for Bloch oscillation experiment, where RSC and BO are Raman sideband cooling and Bloch oscillation, respectively; PBS is the polarizing beam splitter; Dichroic mirrors (785 nm RazorEdge Dichroic laser beamsplitter from Semrock), with a longpass edge at 785 nm; HWP1,2 are the half-waveplates. In our frequency tuning setup of the BO lattice fields in Fig. 4.14, the frequencies of two orthogonally-polarized BO lattice fields are tuned by the RF inputs of two AOMs: one can be ramped, and the other is fixed. Therefore, the direction of Bloch oscillation can be switched by changing the angle of HWP1, and HWP2 is used to tune and keep the polarization of one BO lattice field the same as another one.

Continuing from the output of the optical fibre, the lattice field was separated into two parts to build a 1D optical lattice with the potential depth U_0 ($7E_R$), where the polarization of two fields should be the same, and optimized with two

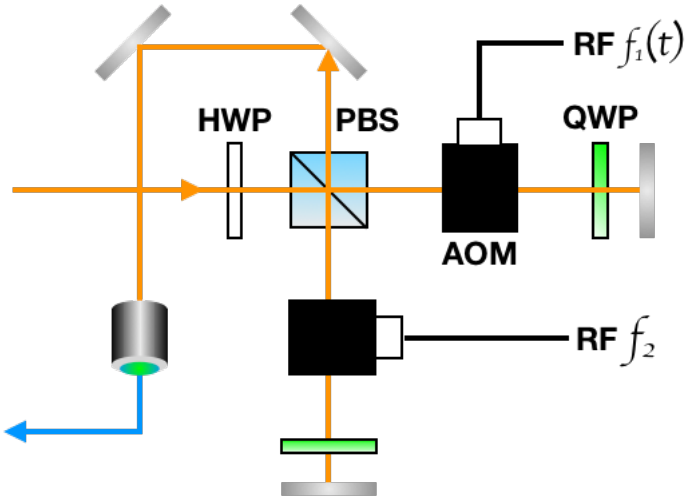

Figure 4.14: The frequency tuning setup of the lattice fields for Bloch oscillation, where HWP is the half-waveplate; QWP is the quarter-waveplate; PBS is the polarizing beam splitter; AOM is acoustic optical modulator; RF $f_{1,2}$ is the input frequency of AOM for frequency tuning.

HWPs (half-waveplates) in the setup. The probe and control fields still counter-propagated with each other ($\measuredangle 185°$) such as the alignment described in Section 2.2.2, but the interaction plane was changed from the vertical plane (yOz) to the horizontal plane (xOy). The frequencies, the heterodyne detection setup, and the beam size of the probe and control fields have already been discussed in Section 2.2.2. The atomic transitions used in the probe and control fields were changed to D1 $|F = 2\rangle \rightarrow |F' = 3\rangle$ and D1 $|F = 3\rangle \rightarrow |F' = 3\rangle$, respectively. Changing the frequency of the probe and control fields to D1 line provided a possibility to align the lattice beams and the probe beam with a dichroic mirror (see Fig. 4.13).

4.2.2 Time Sequence

Figure 4.15 shows the time sequence of this experiment, including four parts:

1. MOT: This stage prepared a cold atomic ensemble with the cooling field, repump field and the quadratic magnetic field, which are discussed in Sections 2.2.1 and 2.2.3.

2. Raman sideband cooling: This stage was the precooling phase for loading atoms into the 1D optical lattice of Bloch oscillation, as discussed in Section 3.2.3. The total duration of z-axis magnetic field was reduced to 8 ms.

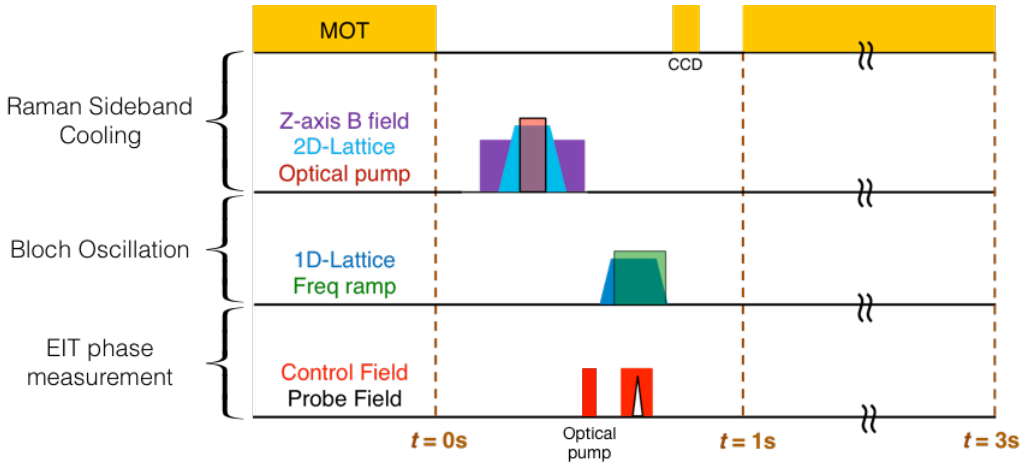

Figure 4.15: The time sequence of the experiments: MOT, Raman sideband cooling, Bloch oscillation and EIT phase measurement.

3. Bloch oscillation: The pulse duration of the 1D lattice was 4 - 8 ms, where the rising and falling time were 0.8 and 0.1 ms, respectively. In Eq. 4.19 (b_i and b_f were 6 and 50, respectively) and Fig. 4.16, the rising time was the same as that of Raman sideband cooling to avoid the internal transitions; the falling time was close to 0 (0.1 ms) to keep the atomic velocity after Bloch oscillation. The linear frequency ramping started at 1 ms after introducing the lattice field, and lasted a few ms with the optimized acceleration a 30 m/s^2 (75 MHz/s).

$$I = \tanh(b_i(t-0.4)) + \tanh(-b_f(t-4)). \tag{4.19}$$

4. EIT phase measurement: This part was the same as in Section 2.2.3. To measure the atomic velocity at different moments during the acceleration of Bloch oscillation, the delay generator DG535 (DG535 - Low jitter delay generator from SRS) was used to shift the timing of the control and the probe pulses. Additionally, we added an extra control field pulse with 0.5 ms duration for the optical pumping from $|F=3\rangle$ to $|F=2\rangle$. This pulse was introduced before Bloch oscillation started with two reasons. One is to use full power of the control field to pump the populations to $|F=2\rangle$, because most population were on $|F=3, m_F=3\rangle$ state after Raman sideband cooling process. The other is to avoid the extra momentum kicks of the optical pumping during the acceleration of Bloch oscillation. In this experiment, we tended to measure the recoil velocity caused by the accelerating lattice, so the extra momentum kicks from the optical pumping could cause some systematic errors.

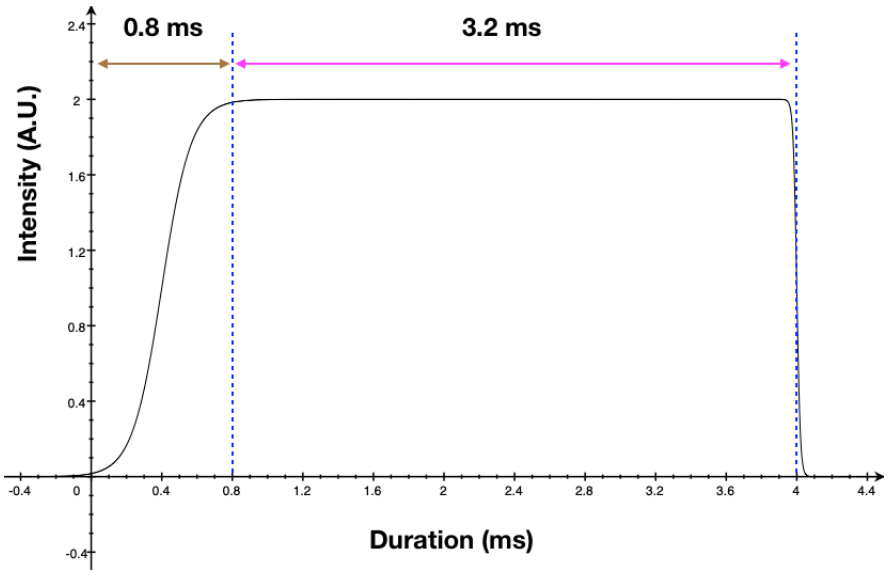

Figure 4.16: The time profile of the 4 ms lattice field pulse for Bloch oscillation.

4.3 Data and Discussion

Figure 4.17 shows the displacement of the atomic ensemble at different flight time after the same Bloch oscillation process, where the ramping rate was 75 MHz/s (30 m/s^2) and the ramping time was fixed at 3 ms. Only part of atoms were accelerated by Bloch oscillation, which the highest ratio was 55% in this experiment. There were two reasons for this low transfer ratio. Firstly, the temperature of the atomic ensemble was not low enough with respect to the recoil temperature, so there were some atoms not following the motion of the lattice. Moreover, the oscillation efficiency mentioned in Section 4.1.3 might not be 100%. Referring to Eqs. 4.15 - 4.17, the Landau-Zener tunnelling probability r in this case was $e^{-24} = 3.8 \times 10^{-11}$ and the oscillation period τ_B was 411 μs (calculated from Eq. 4.9), so the oscillation efficiency during the ramping time 3 ms was $(1 - 3.8 \times 10^{-11})^{3000/411} = 0.9999999997 \approx 1$, which means the atomic temperature dominated the final oscillation efficiency in this case. Additionally, in Fig. 4.17 we can also see that the fluorescent images become dimmer and dimmer with the longer flight time. This was due to the escape of atoms from the dipole trap on z-axis, where our Raman sideband cooling was on xy plane only.

From the experiment in Chapter 2 to that in this chapter, we added some components for Raman sideband cooling and Bloch oscillation, both of which caused a few

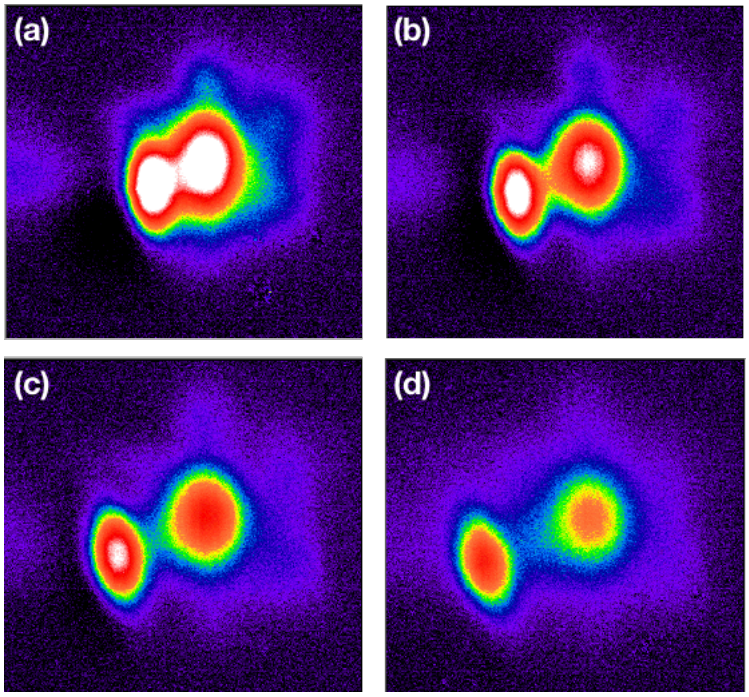

Figure 4.17: The images of the atomic ensembles after Bloch oscillation, where the acceleration a is 30 m/s^2; the ramping time is 3 ms; the waiting time for imaging after frequency ramping is: (a) 15 ms; (b) 20 ms; (c) 25 ms; (d) 30 ms.

loss of the atoms. In addition, sub-Doppler cooling also needed to be implemented to pre-cool atoms for the following Raman sideband cooling, which could cause a huge loss of atoms as well. As mentioned above, the reduction of optical depth (OD) was inevitable, which shrank from 36 to 1. This degradation means the phase shift in the EIT measurement would roughly shrink to 1/36 of the magnitude shown in Chapter 2, in addition, our target was to measure the recoil velocity, which meant the data precision needed to be improved 2 orders of magnitude.

To achieve a better precision, we built PID system to stabilize the control field power (see Appendix A.2) and improved the algorithm of the phase shift calculations (see Section 4.3.2). We did a test of the delay time with different detunings of the probe field without Bloch oscillation as shown in Fig. 4.18. Based on Eq. 4.20 [11] (where Γ_{31} is the spontaneous decay rate of $|3\rangle \rightarrow |1\rangle$ transition, Ω_c is the Rabi frequency of the control field, and δ is the two-photon detuning), the delay time was proportional to the refractive index due to no light dragging effect under this circumstance. The resolution (precision) was 0.005 ns (0.7 mm/s), which was about 1 order of magnitude smaller than the performance shown in Chapter 2 (0.03 ns).

$$Re[\chi^{(1)}] \propto \frac{\Gamma_{31}}{\Omega_c^2}\delta + O(\delta^2). \tag{4.20}$$

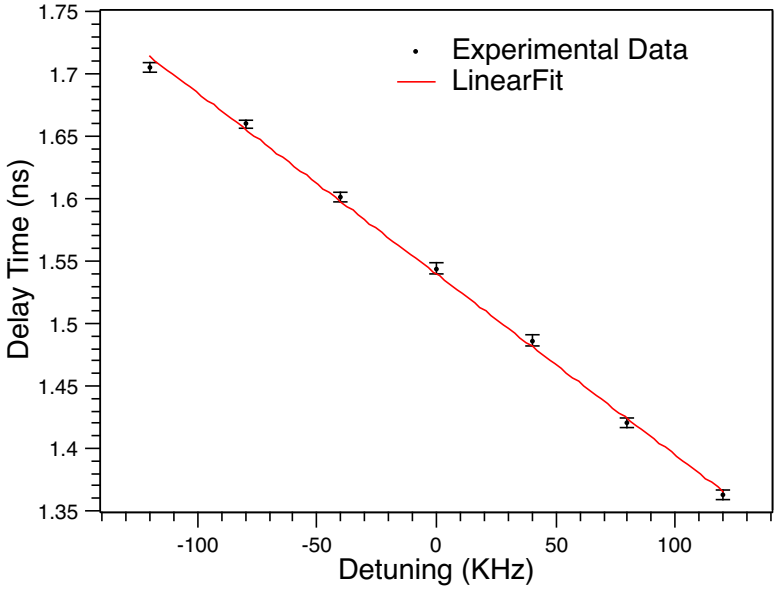

Figure 4.18: The delay time as a function of the detuning of the probe field, where the control field power is 2 mW.

The phase measurement for a different ramping time of Bloch oscillation is shown in Fig. 4.19. The control field power was 0.6 mW, corresponding to 0.2 μs group delay t_g in EIT process. The pulse widths of the control and the probe fields were 1 ms square pulse and 5 μs (FWHM) Gaussian pulse, respectively. The frequencies of the control and the probe fields were both resonant with $|2\rangle \leftrightarrow |3\rangle$ and $|1\rangle \leftrightarrow |3\rangle$, respectively. The ramping rate was 75 MHz/s (30 m/s^2), and the potential depth U_0 was $7E_R$. The acquisition time for each data point was 75 s on average 25 times. From Fig. 4.19, we can see the phase shift in the beginning of frequency ramping increased 2 times faster than other data points, which might be caused by the non-adiabaticity of the external force (see Section 4.1.3). The direction of Bloch oscillation can be switched by tuning the angles of the HWP shown in Fig. 4.13. Both of the phase shifts with Bloch oscillation in two directions had the same offsets from the phase shifts caused by EIT effect, the partial atoms not accelerated by Bloch oscillation and the optical path difference between the signal beam and the reference beam (see the signal and the reference beam alignment in Section 2.2.2).

To take out these offsets, we took the difference between the phase shifts in two oscillating directions and plotted them in Fig. 4.20.

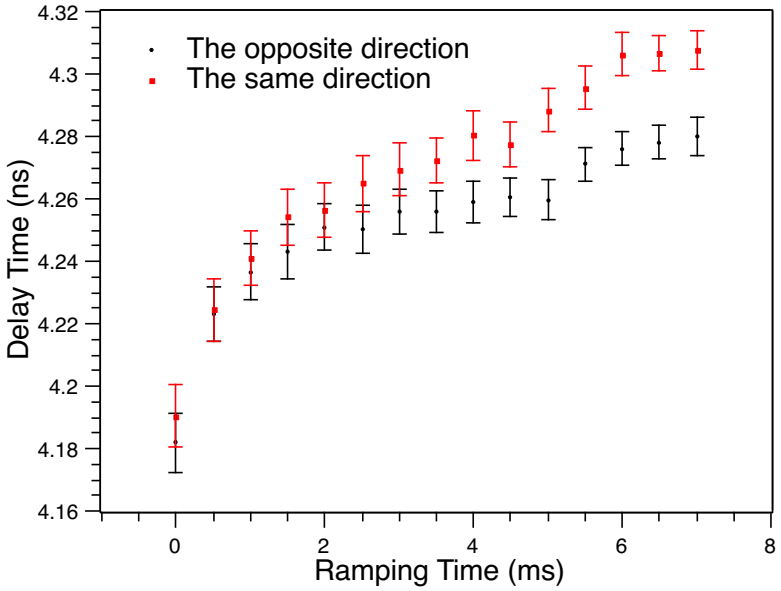

Figure 4.19: The delay time as a function of the ramping time, where the red squares are the data of co-propagated Bloch oscillation and the probe field; the black circles are the data of counter-propagated Bloch oscillation and the probe field.

Figure 4.20 shows the velocity of the atomic ensemble increasing monotonically during Bloch oscillation, which is not stepwise like Fig. 4.7. To improve this result, we had two strategies: One was to extend the data acquisition time to 30 minutes per data point, as shown in Fig. 4.21, which achieved the precision 0.52 ps (0.00052 ns), one more order of magnitude improvement. The other was to use the theoretical simulation to search for an optimized potential depth U_0 and the cooling temperature T_B for Bloch oscillation.

4.3.1 Theoretical Simulation

The energy of a particle in a 1D periodic potential can be described by the following Schrodinger equation:

$$\widehat{H}_M \Psi_n(z) = [-\frac{\hbar^2}{2M}\nabla_z^2 + \widehat{U}(z)]\Psi_n(z) = E_n \Psi_n(z), \tag{4.21}$$

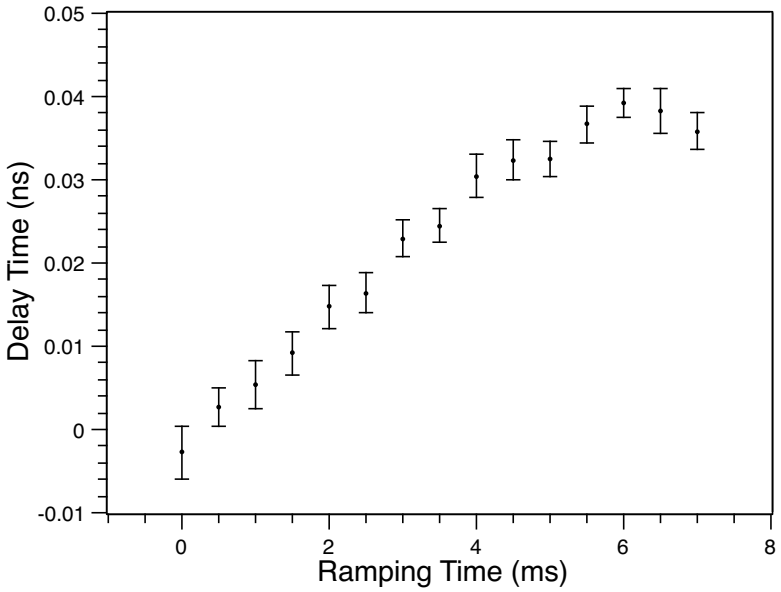

Figure 4.20: The delay time as a function of the ramping time, where the phase time data are the difference between the data in two configurations in Fig. 4.19.

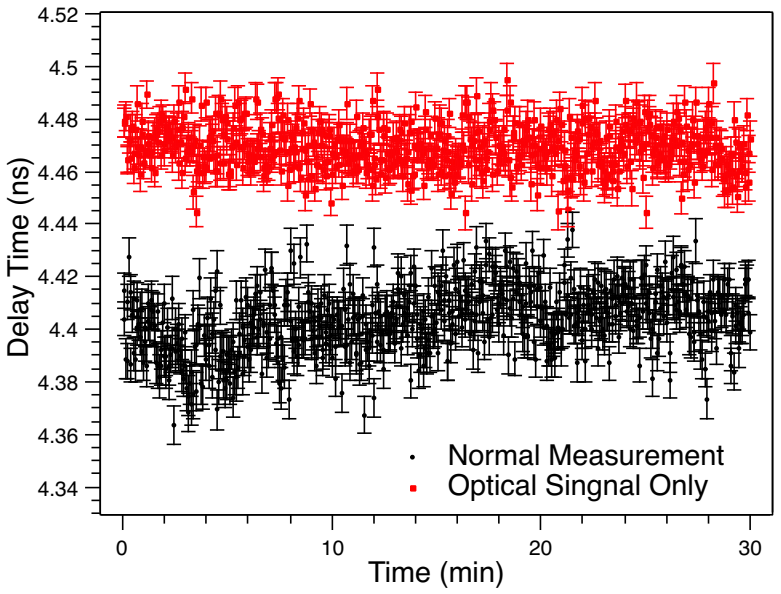

Figure 4.21: The stability test of the phase measurement, where black circles are the measurement data; red circles are the optical signals of phase differences without passing EIT media. The precision of phase measurement data and the optical signals are 0.52 ps and 0.36 ps, respectively.

where M is the mass of the particle; n is the quantum number of the energy band; $\widehat{U}(z)$ is a periodic function of the potential well. To obtain the energy band structure, we convert Eq. 4.21 to the form in k-space:

$$\widehat{H}_M\Psi_n(p) = [\frac{(\widehat{p}+n\cdot 2\hbar k)^2}{2M} + \int dp'\widehat{U}(p-p')]\Psi_n(p) = E_n(p)\Psi_n(p), \tag{4.22}$$

where k is the wavevector of the lattice field; $2k$ is the lattice base vector of 1D lattice, which is explained in Section 3.1.1.2. Considering the fundamental, first-excited and second-excited band, the Hamiltonian in k-space with $n \in [-2, 2]$ can be expressed in a matrix form for the numerical calculation as follows:

$$\begin{bmatrix} \frac{(p-4\hbar k)^2}{2M} & & & & & \\ & \frac{(p-2\hbar k)^2}{2M} & & & & \\ & & \frac{(p)^2}{2M} & & & \\ & & & \frac{(p+2\hbar k)^2}{2M} & & \\ & & & & \frac{(p+4\hbar k)^2}{2M} & \end{bmatrix} + \begin{bmatrix} \frac{U_0}{2} & \frac{U_0}{4} & & & & \\ \frac{U_0}{4} & \frac{U_0}{2} & \frac{U_0}{4} & & & \\ & \frac{U_0}{4} & \frac{U_0}{2} & \frac{U_0}{4} & & \\ & & \frac{U_0}{4} & \frac{U_0}{2} & \frac{U_0}{4} & \\ & & & \frac{U_0}{4} & \frac{U_0}{2} & \end{bmatrix}, \tag{4.23}$$

where U_p is assumed to be a constant U_0 in the numerical integration under the weak-binding limit ($U_0 < 20E_R$). Spanning p to the first Brillouin zone ($-\hbar k$ to $+\hbar k$), the band structure of the first three bands could be obtained by the eigenvalue calculation of Eq. 4.23. The results of the first two bands are shown in Fig. 4.22, and we can see the band structure of $U_0 = 7E_R$ case has a higher offset potential energy, a larger band gap, and a flatter energy curve (narrower bandwidth) than $U_0 = 2.3E_R$ case, which is consistent with the discussion in Section 4.1.3.

Referring to Eq. 4.13, the average velocity $\langle v\rangle(p)$ of the particle in the fundamental band can be calculated by p derivative of the energy structure, as shown in Fig. 4.23. In the figure, we can see the velocity oscillation in $U_0 = 2.3E_R$ case is much larger than that in $U_0 = 7E_R$ case, so it is more difficult to observe Bloch oscillation with higher potential depth.

For the total velocity v_{total} during Bloch oscillation, in this case, the momentum p is a function of time and the changing average velocity $\langle v\rangle$ of the particles in the lattice becomes a functional of $p(t)$. Combining $\langle v\rangle[p(t)]$ and the additional velocity at given by the accelerating lattice, the total velocity v_{total} can be obtained as:

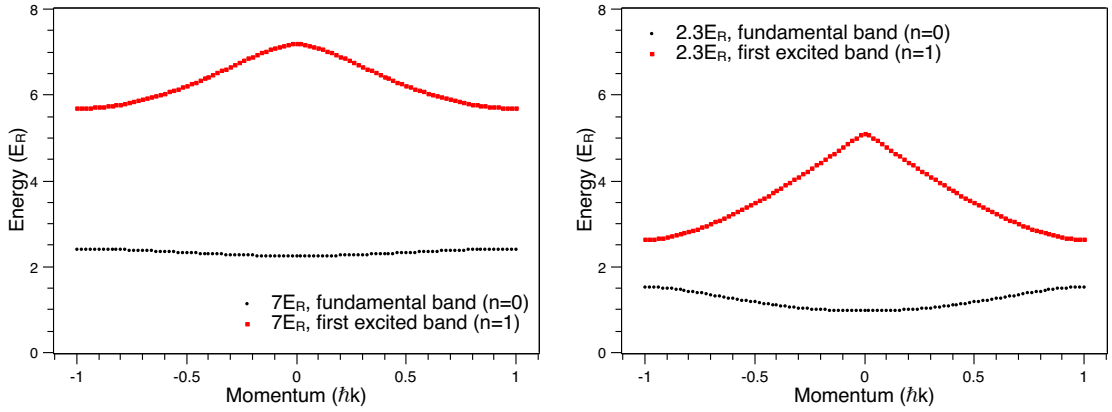

Figure 4.22: The band structure of the fundamental and the first excited bands. *Left*: U_0 is $7E_R$; *Right*: U_0 is $2.3E_R$.

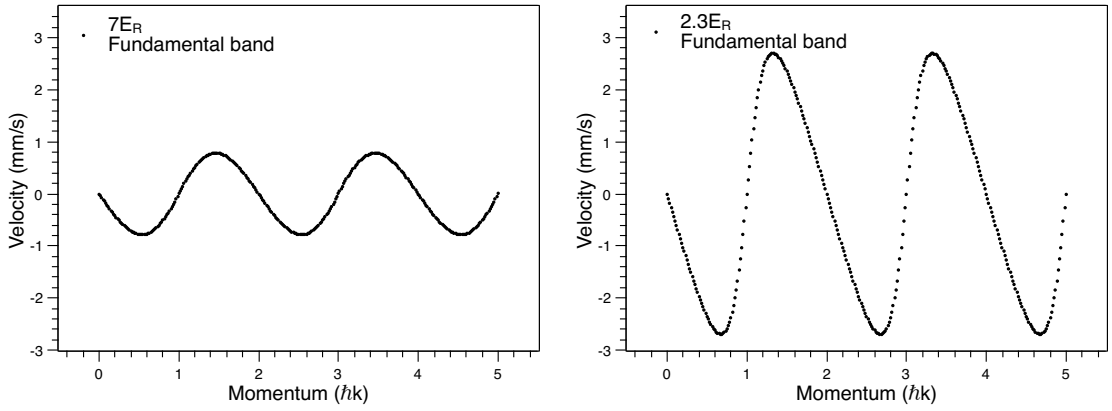

Figure 4.23: The velocity of the particle in the fundamental band as a function of momentum p in the unit of $\hbar k$. *Left*: U_0 is $7E_R$; *Right*: U_0 is $2.3E_R$.

$$p(t) = p(0) + Mat \tag{4.24}$$

$$v_{\text{total}} = \frac{exp(-E_0(p)/k_BT)}{Z} \cdot \big(\langle v\rangle[p(t)] + at\big). \tag{4.25}$$

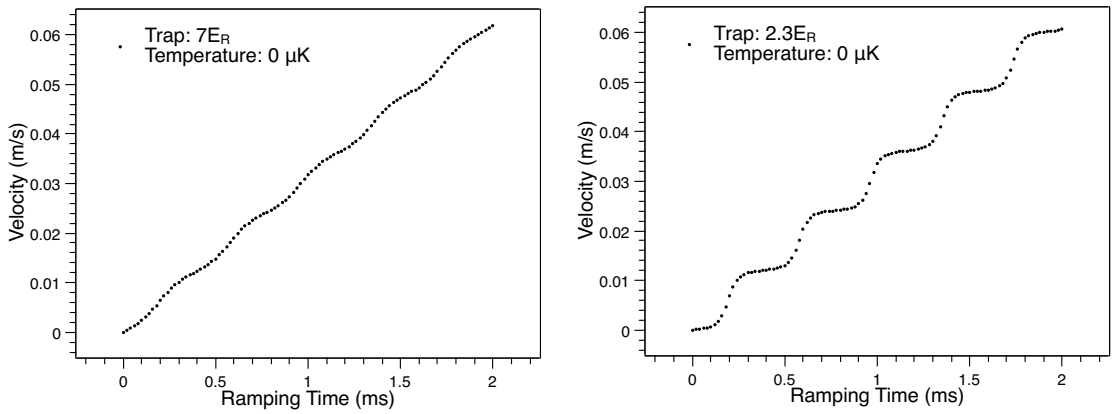

Figure 4.24: The simulation of the total velocity v_{total} as a function of the ramping time, where the accelerations are both 30 m/s^2. *Left*: U_0 is $7E_R$, T_B is 0 μK; *Right*: U_0 is $2.3E_R$, T_B is 0 μK.

Figure 4.24 shows the simulation of Eq. 4.25 with two potential depths U_0: $7E_R$ and $2.3E_R$. To simulate the real temperature of our atomic ensemble before Bloch oscillation, the Boltzmann factor $exp(-E_0(p)/k_BT)/Z$ is added into Eq. 4.25, where $E_0(p)$ is the energy of the fundamental band (n=0), and the simulation result is shown in Fig. 4.25.

From Figs. 4.24 and 4.25, we can see that it is impossible to observe the stepwise increasing of the velocities under our current configuration (U_0 is $7E_R$, T_B is 2 μK). The potential depth U_0 should be lower than $3E_R$ to avoid a flat curve of the energy structure. However, a shallower trap depth would cause a lower oscillation efficiency (see Eqs. 4.15 - 4.17). For example, when U_0 is $3E_R$, tunnelling probability r is $exp(-4.4)$, so the oscillation efficiencies after 3 ms and 7 ms ramping time are 91% and 81%, both of which are lower than those in $U_0 = 7E_R$ case, but they are acceptible, so reducing the lattice potential is a good solution. The real temperature T_B in our experiment was 1.5 - 2 μK, which was caused by the heating effect of the optical pumping before Bloch oscillation. Velocity selection (Raman cooling) [12, 13]

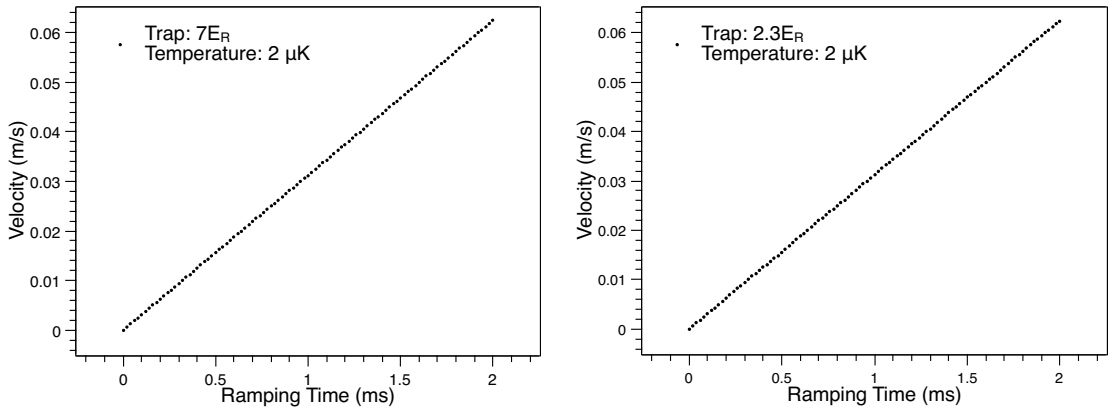

Figure 4.25: The simulation of the total velocity v_{total} as a function of the ramping time, where the accelerations are both 30 m/s^2. *Left*: U_0 is $7E_R$, T_B is 2 μK; *Right*: U_0 is $2.3E_R$, T_B is 2 μK.

is a possible solution to select the cold atoms in some specific momentum range, which can achieve a high efficiency of Bloch oscillation. We plan to implement the velocity selection to replace the optical pumping in the near future.

4.3.2 Phase Measurement Algorithm

In our phase measurement, we acquired two waveform (signal and reference) data from the oscilloscope and calculated their phase difference. Fig.4.26 is the user interface of the acquisition program, which includes three acquisition modules: left, center, and right part. In Chapter 2, we used the left part to compare the zero points of two waveforms to calculate the phase difference. This method picked the data near the zero points only, which was usually less than 20 data points in a single shot. This was a huge waste of the information we obtained (the oscilloscope acquired 2500 points each cycle). To utilise the data points more efficiently and improve the measurement precision, we implemented the ellipse fitting to calculate the phase shifts with all data points. In our demonstration, there were two stages of the ellipse fitting:

1. Construction of the Lissajous curve with the acquired data: As shown in Eq. 4.26, the two waveforms were represented by two cosine functions with different amplitudes (A_1 and A_2), different offsets (B_1 and B_2) and a phase difference ($\Delta\theta$). Here we assumed the frequencies ω of two waveforms were the same (70 MHz in this

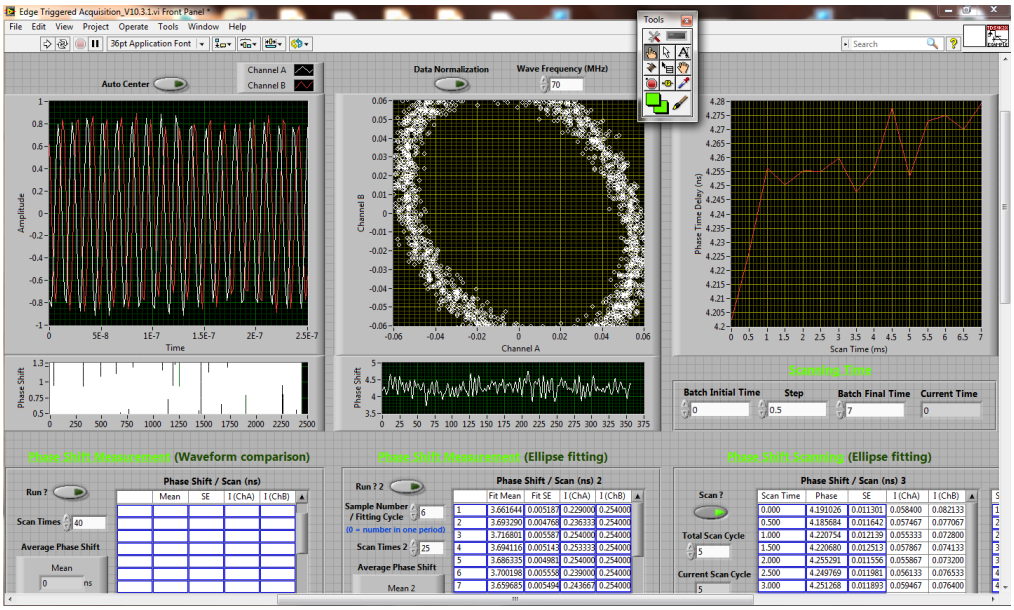

Figure 4.26: The user interface of the acquisition LabVIEW program. This program provides two methods to calculate the phase difference: waveform camparison and ellipse fitting. The mean value and the standard error are calculated in each acquisition cycle, and calculated again after a few cycles (20 times in Chapter 2, 25 times in Chapter 4) to obtain one final data point on the plot. The right part integrates the pulse delay control with the delay generator DG535 to scan the phase shifts at different timings.

experiment), and eliminated the time variable t and ω:

$$\begin{cases} x = A_1 \cos(\omega t + 0) + B_1 \\ y = A_2 \cos(\omega t + \Delta\theta) + B_2 \end{cases} \tag{4.26}$$

$$t = \frac{1}{\omega} cos^{-1}(\frac{x - B_1}{A_1}) = \frac{1}{\omega}\big[cos^{-1}(\frac{y - B_2}{A_2}) - \Delta\theta\big]. \tag{4.27}$$

Equation 4.27 can be rearranged to:

$$\begin{aligned} \frac{x - B_1}{A_1} &= cos\big(cos^{-1}(\frac{y - B_2}{A_2}) - \Delta\theta\big) \\ &= \frac{y - B_2}{A_2} cos\Delta\theta + sin\big(cos^{-1}(\frac{y - B_2}{A_2})\big) sin\Delta\theta \end{aligned} \tag{4.28}$$

$$\Rightarrow \frac{x - B_1}{A_1} - \frac{y - B_2}{A_2} cos\Delta\theta = \sqrt{1 - (\frac{y - B_2}{A_2})^2} sin\Delta\theta \tag{4.29}$$

$$\Rightarrow (\frac{x - B_1}{A_1})^2 + (\frac{y - B_2}{A_2})^2 - 2(\frac{x - B_1}{A_1})(\frac{y - B_2}{A_2}) cos\Delta\theta = sin^2\Delta\theta \tag{4.30}$$

$$\Rightarrow \frac{1}{A_1^2}x^2 + \frac{1}{A_2^2}y^2 - \frac{2}{A_1 A_2} cos\Delta\theta xy + \cdots, \tag{4.31}$$

Comparing Eq.4.31 with the equation of the conic section: $ax^2 + bxy + cy^2 + dx + ey + f = 0$, if we could obtain the parameters in the conic section function, the phase difference $\Delta\theta$ could be calculated with:

$$\Delta\theta = cos^{-1}(\frac{b}{-2\sqrt{ac}}). \tag{4.32}$$

2. Direct least square ellipse fitting: Normally, the curve fitting requires some initial guess of the fitting parameters. It is often necessary to manually tune the parameters during the fitting process to avoid the local minimum as the fitting result (taking least square method as an example, it tends to find the minimum of the square-value summation of the deviation between experimental data and the theoretical model). Here, we used another fitting method to automate this process.

"Direct least square ellipse fitting" algorithm was developed by Fitzgibbon *et al.* in 1996 [14], which featured the conversion from a curve fitting problem (specifically for ellipse curves only) to an eigenvalue / eigenvector calculation. Based on the general equation of the conic section ($ax^2 + bxy + cy^2 + dx + ey + f = 0$), we set the fitting error as $F(\alpha, D)$, where the definitions of α and D were:

$$\alpha = \begin{bmatrix} a \\ b \\ c \\ d \\ e \\ f \end{bmatrix} \quad D = \begin{bmatrix} x_1^2 & x_1y_1 & y_1^2 & x_1 & y_1 & 1 \\ x_2^2 & x_2y_2 & y_2^2 & x_2 & y_2 & 1 \\ x_3^2 & x_3y_3 & y_3^2 & x_3 & y_3 & 1 \\ \vdots & \vdots & \vdots & \vdots & \vdots & \vdots \\ \vdots & \vdots & \vdots & \vdots & \vdots & \vdots \\ \vdots & \vdots & \vdots & \vdots & \vdots & \vdots \end{bmatrix}, \tag{4.33}$$

where α was a vector composed of the fitting parameters, and D was a matrix with the calculated values from (x_i, y_i) data (i was the index of the data point). Using the least square method, we needed to find the minimum value of $F(\alpha, D)^2$:

$$F(\alpha, D)^2 = (D\alpha)^T(D\alpha). \tag{4.34}$$

For the ellipse fitting, we set an extra constraint C matrix:

$$4ac - b^2 > 0 \tag{4.35}$$

$$\alpha^T C\alpha - p = 0 \quad (p > 0) \tag{4.36}$$

$$C = \begin{bmatrix} 0 & 0 & 2 & 0 & 0 & 0 \\ 0 & -1 & 0 & 0 & 0 & 0 \\ 2 & 0 & 0 & 0 & 0 & 0 \\ 0 & 0 & 0 & 0 & 0 & 0 \\ 0 & 0 & 0 & 0 & 0 & 0 \\ 0 & 0 & 0 & 0 & 0 & 0 \end{bmatrix}. \tag{4.37}$$

Introducing Lagrange multiplier λ and the constraint C, the formula of error square became:

$$F(\alpha, D)'^2 = (D\alpha)^T(D\alpha) - \lambda(\alpha^T C\alpha - p). \tag{4.38}$$

To obtain the minimum value of Eq.4.38, we took its α derivative, and set it as 0:

$$2D^T D\alpha - 2\lambda C\alpha = 0. \tag{4.39}$$

We set $D^T D = S$. Considering the determinant of C must be 0 (so there is no inverse matrix of C), Equation 4.39 can be rearranged to:

$$S^{-1}C\alpha = \frac{1}{\lambda}\alpha. \tag{4.40}$$

As shown in Eq. 4.40, the curve fitting problem is converted to an eigenvalue / eigenvector calculation. However, there are six pairs of the eigenvalues and their corresponding eigenvectors, denoted by $[1/\lambda_i, \alpha_i]$, so choosing a correct solution is crucial. In addition, the scalings of the eigenvectors cause the solution of eigenvectors not unique, so we assumed the eigenvector solution α_i was $\mu\upsilon_i$. Using the relation in Eq. 4.39 and timing α^T in the front of each side of Eq. 4.39, we wrote equations as follows:

$$\alpha^T S\alpha = \lambda\alpha^T C\alpha = p\lambda \tag{4.41}$$

$$\mu = \sqrt{\frac{p\lambda}{\upsilon^T S\upsilon}}, \tag{4.42}$$

where p and $\upsilon^T S\upsilon$ are always positive, so μ exists only if λ is positive. Therefore, we chose a pair of the eigenvector with a positive eigenvalue $(1/\lambda)$ as the fitting solution, and it was the only pair under the ellipse constraint C. The unknown value μ does not make a difference to our result, because it is eliminated in the $\Delta\theta$ calculation (see Eq. 4.32).

An advantage of the ellipse fitting is able to use the information of all data points, and it requires only 6 points to define an ellipse (see Fig.4.27). Because of the six unknown parameters in α, we separated the data (2500 pionts) to 2500/6 fitting cycles to enhance the precision. The drawback of the ellipse fitting is its fitting range, which cannot tell $\Delta\theta$ from $2\pi - \Delta\theta$, so $\Delta\theta$ needs to be in the range $[0, \pi]$, which is the reason why we tuned the phase difference with signal cables in different lengths to fit our measurement data in this range.

References

[1] F. Bloch. Über die Quantenmechanik der Elektronen in Kristallgittern. *Z. Phys.*, 52:555–600, 1929.

[2] D. R. Askeland and P. P. Phule. *The Science and Engineering of Materials.* Thomson, 5th edition, 2006.

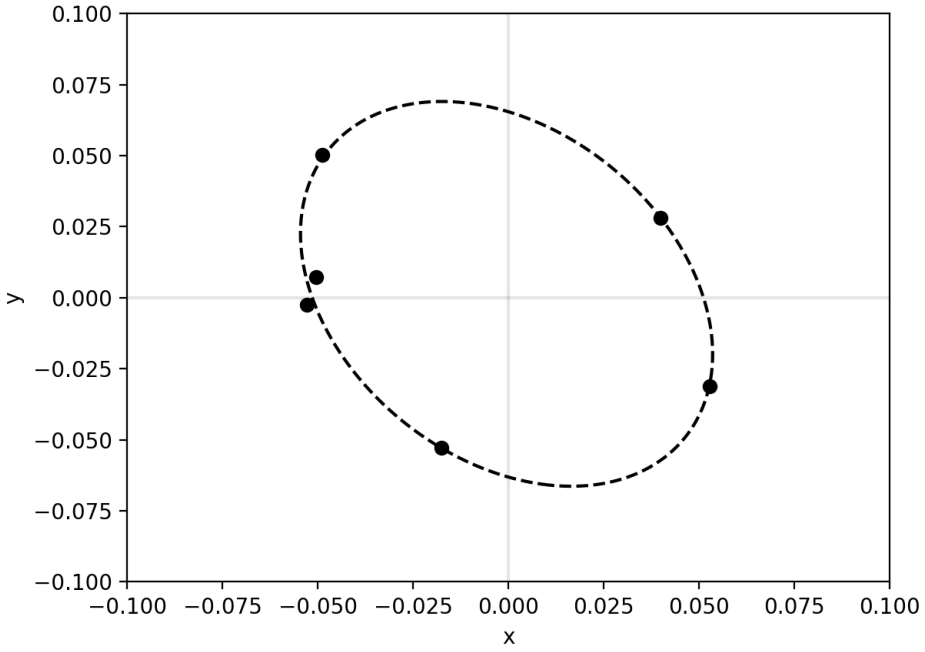

Figure 4.27: Direct ellipse fitting with the first six data points, where the black circles are the data points; the dash line is the fitting ellipse curve.

[3] P. A. Tipler and R. A. Llewellyn. Classical Concept Review, Chapter 10: Mean Free Path (`http://bcs.whfreeman.com/webpub/Ektron/Tipler%20Modern%20Physics%206e/Classical%20Concept%20Review/Chapter_10_CCR_10_Mean_Free_Path.pdf`), 2008.

[4] P. J. McNally. 3D Imaging of Crystal Defects. *Nature*, 496(7443):37–38, April 2013.

[5] E. Spain and A. Venkatanarayanan. Review of Physical Principles of Sensing and Types of Sensing Materials. *Comprehensive Materials Processing*, 13:5–46, 2014.

[6] C. Waschke, H. G. Roskos, R. Schwedler, K. Leo, H. Kurz, and K. Köhler. Coherent Submillimeter-wave Emission from Bloch Oscillations in a Semiconductor Superlattice. *Phys. Rev. Lett.*, 70(21):3319–3322, May 1993.

[7] M. B. Dahan, E. Peik, J. Reichel, Y. Castin, and C. Salomon. Bloch Oscillations

of Atoms in an Optical Potential. *Phys. Rev. Lett.*, 76(24):4508–4511, June 1996.

[8] E. Peik, M. B. Dahan, I. Bouchoule, Y. Castin, and C. Salomon. Bloch Oscillations of Atoms, Adiabatic Rapid Passage, and Monokinetic Atomic Beams. *Phys. Rev. A*, 55(4):2989–3001, April 1997.

[9] P. Cladé, M. Andia, and S. Guellati-Khélifa. Improving Efficiency of Bloch Oscillations in the Tight-binding Limit. *Phys. Rev. A*, 95(6):063604, 2017.

[10] C. Zener. Non-adiabatic Crossing of Energy Levels. *Proc. R. Soc. London Ser. A*, 137:696–702, July 1932.

[11] M. Fleischhauer, A. Imamoglu, and J. P. Marangos. Electromagnetically Induced Transparency: Optics in Coherent Media. *Rev. Mod. Phys.*, 77(2):633–673, 2005.

[12] K. Moler, D. S.Weiss, M. Kasevich, and S. Chu. Theoretical Analysis of Velocity-selective Raman Transitions. *Phys. Rev. A*, 45(1):342–348, January 1992.

[13] H. J. Lee, C. S. Adams, M. Kasevich, and S. Chu. Raman Cooling of Atoms in an Optical Dipole Trap. *Phys. Rev. Lett.*, 76(15):2658–2661, April 1996.

[14] A. W. Fitzgibbon, M. Pilu, and R. B. Fisher. Direct Least Squares Fitting of Ellipses (`http://cseweb.ucsd.edu/~mdailey/Face-Coord/ellipse-specific-fitting.pdf`), January 1996.

Chapter 5

Conclusion

In this thesis, a new experimental method of EIT-enhanced light dragging effect for the motion quantum sensing is introduced. To prove the feasibility and performance of this new technique, two experiments were demonstrated.

The light dragging effect was performed by the interaction between the light field and a moving atomic ensemble in free space. The light dragging effect induced a phase shift of light, which was proportional to the velocity of the moving medium. The chosen medium was a ^{85}Rb cold atomic ensemble. The centre-of-mass velocity of the ensemble was induced by the resonant scattering of the light fields. EIT effect was used to enhance the dragging coefficient F_d with a high dispersion of the refractive index and reduce the absorption of the probe field intensity. A large dragging coefficient F_d ($= 1.67 \times 10^5$), two orders of magnitude larger than the ^{85}Rb hot vapour [1], and five orders of magnitude larger than the first light dragging effect [2, 3] was achieved. The sensitivity of the velocity was 1 mm/s, two orders of magnitude smaller than thermal velocity width (Doppler broadening) of the atomic ensemble (about 100 mm/s).

Also, a degenerate Raman sideband cooling of ^{85}Rb atoms was demonstrated. With a 2D lattice produced by three lattice fields, an external magnetic field, and an optical pumping field, the temperature of the atomic ensemble achieved near recoil temperature of 357 nK. Moreover, the measurements of atoms' motion in a driven periodic potential were conducted using the atomic ensemble trapped in a 1D optical lattice and accelerated by Bloch oscillation. The phase shift measurements showed the linear-like relation to the accelerating time with the data precision 0.00036 rad (0.005 ns, 0.7 mm/s), but did not show the stepwise trend with the oscillation period

τ_B. With the help of the theoretical simulation, we are aware that the potential depth and the atom's temperature are too high to observe the stepwise motion in our phase measurement. In the future, we will reduce the lattice field intensity and implement the velocity selection technique to approach the precision measurement of the recoil velocity of the atoms during Bloch oscillation. Besides, the sensitivity of the phase shift measurements can also be improved by using larger lattice beam waist to load more atoms into the lattice, since the sensitivity of the phase shift measurement is proportional to the square root of OD.

References

[1] A. Safari, I. D. Leon, M. Mirhosseini, O. S. Magaña-Loaiza, and R. W. Boyd. Light-drag Enhancement by a Highly Dispersive Rubidium Vapor. *Phys. Rev. Lett.*, 116:013601, 2016.

[2] H. Fizeau. Sur les Hypothèses Relatives *à* l'*é*ther Lumineux. *C. R. Acad. Sci.*, 33:349–355, 1851.

[3] H. Fizeau. The Hypotheses Relating to the Luminous Aether, and an Experiment which Appears to Demonstrate that the Motion of Bodies Alters the Velocity with which Light Propagates itself in their Interior. *Philosophical Magazine*, 2:568–573, 1851.

Appendix A

Circuit Design

A.1 Magnetic Field Switching

In addition to the MOT coil to produce a quadratic magnetic field with a pair of anti-Helmholtz coil, we also set three pairs of Helmholtz coils to generate the magnetic fields on x, y, and z axes to compensate the ambient magnetic field, and provide a magnetic field along a specific direction during the experiment. To control the magnetic field, we build a current controlling box with a voltage-controlled current circuit as shown in Fig. A.1, and connect it with a constant voltage V_{cc} as the power supply to generate a variable current.

In Fig. A.1, the input controllable voltage V_s is the sum of two voltages. One is from the trimmer used to set an offset current (magnetic field) to compensate the ambient magnetic field. The other is from the trigger pulse regulated by an AND-gate and a constant voltage of the power supply. This is used to switch the current. The input voltage V_s is converted to a tunable current i_o by a n-channel MOSFET (NMOS).

MOSFET has a multi-layer structure made with some semiconductor materials, whose performance is sensitive to the temperature and humidity in the surroundings. To stabilize the current, a v-i (voltage to current) feedback loop is introduced into the circuit. The basic model of the v-i feedback loop is shown in Fig. A.2 [1]. The input voltage V_s is adjusted by the feedback voltage V_f to the real input voltage V_i, which is amplified by OP amp (operational amplifier) and MOSFET to the current AV_i. Because the output current i_o is short to the ground in the ideal case, i_o would

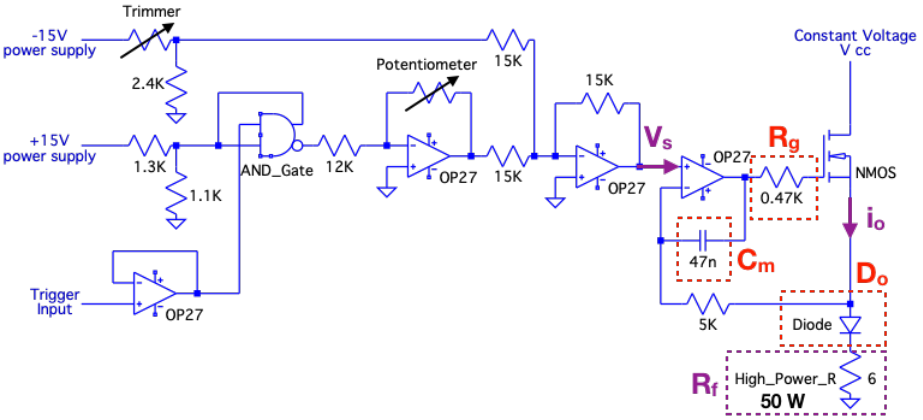

Figure A.1: The circuit design of the voltage-controlled current. The components connected before V_s are to manipulate a tunable input voltage V_s, which corresponds to the output current i_o. The input voltage is amplified and converted to the out current, and the current flows into a feedback loop, which could stabilize the final output current i_o. R_f is the resistor for the feedback gain; R_g resistor, C_m capacitor and D_o diode are designed to ease the high frequency noise.

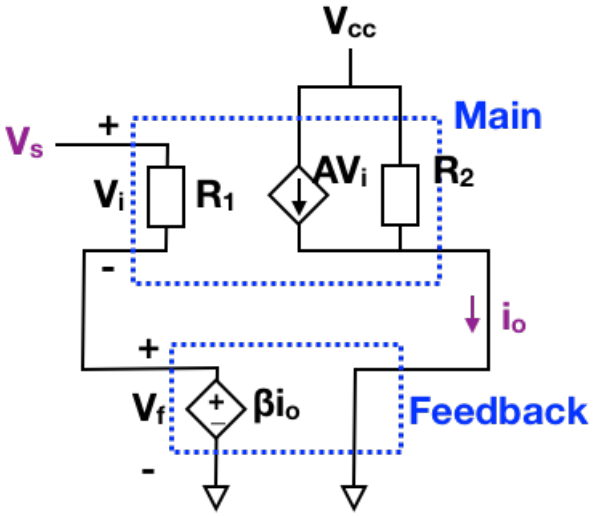

Figure A.2: The basic model of the feedback loop, where $R_{1,2}$ are general load resistors; V_i and V_f are the real input voltage and the feedback voltage, respectively; A and β are the gains in the main circuit (from OP amp and MOSFET) and the feedback circuit, respectively.

be equal to AV_i. To make a feedback voltage, the feedback gain β converts the output current to the feedback voltage βi_0. The above process can be summarized to three equations shown as Eq. A.1:

$$\begin{cases} V_i = V_s - V_f \\ i_o = AV_i \\ V_f = \beta i_o \end{cases} \tag{A.1}$$

$$\Rightarrow \frac{i_o}{V_s} = \frac{A}{1+\beta A}, \tag{A.2}$$

in our case, the gain of OP amp (OP27) is 1.8×10^6, and the transconductance of NMOS (IRF630) is about 0.09 A/V around 400 mA, so the total gain A is much larger than 1. The feedback gain β can be calculated with Eq. A.3:

$$\beta = \left.\frac{V_f}{i_o}\right|_{\text{open}}, \tag{A.3}$$

where the term "open" in Eq. A.3 means that input port is supposed to be open under this condition ($V_s = 0$), therefore, β is equal to R_f, where there is no current flowing through the 5 KΩ resistor (see Fig. A.1). From Eq. A.2, we can see the output current i_o is proportional to $1/R_f$ when A is large enough. R_f is a resistor for high power (80 W) use, which is insensitive to the surrounding changes, so the output current can be very stable. In our experience, there is only 1 mA drift under the condition with 5℃ deviation.

MOSFET is a good current source, but it has an issue called the parasitic oscillation [2], which is proportional to time derivative of the input voltage ($\mathrm{d}V_s/\mathrm{d}t$). This issue becomes non-negligible when the input voltage increases sharply, such as a square trigger pulse (see Fig. A.3). So, R_g, C_m and D_o are designed to ease and block the high frequency noise, and finally the oscillation is not observable.

A.2 PID Stabilization System

To acquire the data with higher precision, the stability of the experimental setup needs to be taken with great care. In our experiment, the data of the phase shifts are proportional to the light frequency and the dragging coefficient as shown in Eq.

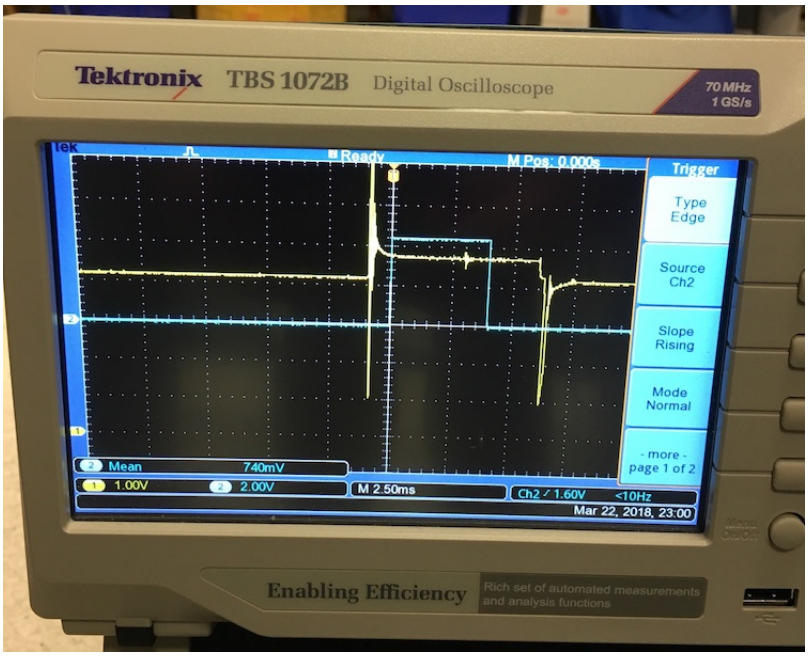

Figure A.3: The parasitic oscillation shows up in the beginning and ending of the signal pulse, where the yellow line is the voltage signal converted from the output current; the blue line is the trigger pulse.

2.6. The light frequency could be well-controlled with the RF synthesizer, but the dragging coefficient is proportional to the dispersion of the refractive index $\partial n/\partial\omega$, which is shown as the central slope in Fig. 1.18 ($Re[\chi]$ function). The dispersion of the refractive index is a function of the control field power as Eq. 2.11 shows, and there is 10% power fluctuation of the probe and control fields. Therefore, a power stabilization setup could improve the precision of our phase measurement.

Figure A.4 shows the system to stabilize the control field power with the combination of AOM and PID (proportional–integral–derivative) controller. We first set a reference level with the wheel of the potentometer on the PID box, and then compare it with the signal level measured by the detector (input from "Detect In" port). Also, the PID box sends out a feedback voltage from "Modulation Out" port to the RF synthesizer (Agile RF synthesizer ARF from MOGLabs) to modulate the RF output power corresponding to our PID feedback voltage. After a few cycles, the control field power would be the reference level we set.

PID circuit is the key role in this feedback system, which is shown in Fig. A.6. PID circuit needs to work with the modulation function of the external equipment,

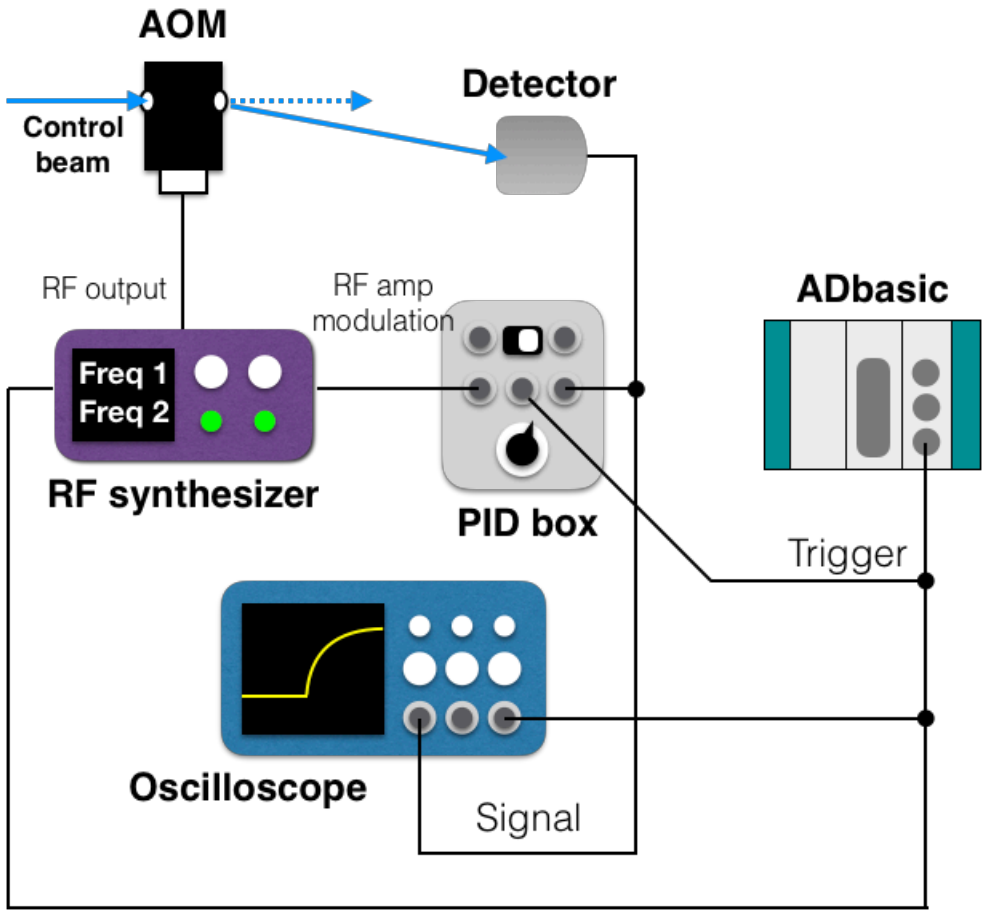

Figure A.4: The power stabilization system of the control field, where the components and their functionalities are explained in the text.

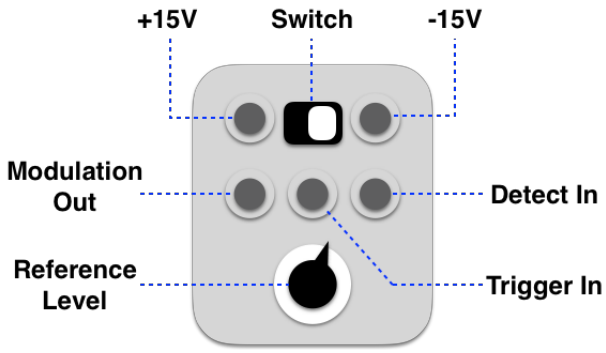

Figure A.5: The input and output (IO) ports of the homemade PID circuit box, where the switch is used to permanently turn on or off the box; $\pm 15V$ are the power supplies of the OP amp (operational amplifier); the others are explained in the text.

and send out the error signal (the difference between the measured signal and reference level set by the user) to compensate the fluctuation of the measured signal. In our experiment, we mainly focus on the power fluctuation, so the PID circuit works with the amplitude modulation of the RF synthesizer. The way which PID deals with the error is to produce a negative gain to respond the change of the signal, which includes three parts: 1. the proportional gain (P-gain G_P), responding to the current error; 2. the integral gain (I-gain G_I), representing the past error from its charged memory (capacitance); 3. the derivative gain (D-gain G_D), predicting the future error with the time derivative of the error to realize the instant fluctuation of the signal. Based on the parameters of our PID circuit, the error compensation $Err_c(t)$ as a function of the error $Err(t)$ is shown as below [3]:

$$\begin{aligned} Err_c(t) =& - G_P \cdot Err(t) - G_I \int_0^t Err(t)dt - G_D \frac{d}{dt} Err(t) \\ =& - \frac{(Trimmer1)}{(2.8K\Omega)} Err(t) \\ & - \frac{1}{(Trimmer2)(4.7nF)} \int_0^t Err(t)dt \\ & - (Trimmer3)(4.7nF) \frac{d}{dt} Err(t). \end{aligned} \tag{A.4}$$

Usually P-gain is the main power of feedback gains, but it cannot compensate the error signal to 0. Therefore, the assistance of I-gain is necessary. D-gain can respond to the fast fluctuation, but a large D-gain might cause the signal to oscillate. We set three trimmers to optimize their resistance values for different conditions. OP27 is a serial number of a kind of OP amp (operational amplifier), which has the characteristics of low 3dB cut-off frequency (10 Hz for open-loop gain) and slow slew rate (2.8 $V/\mu s$), which performs a rising / response time 300 μs in our circuit. R_I and R_D are resistors to solve DC-biasing defect of OP amp and the high frequency noise amplification, respectively.

Figure A.7 shows the performance of our feedback system, where the initial power fluctuation (about 10%) is reduced to less than 1%.

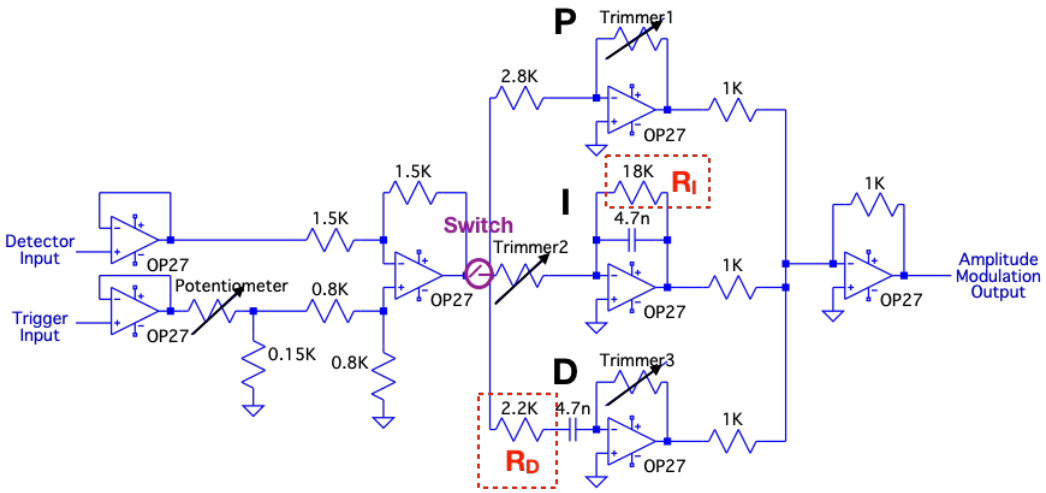

Figure A.6: The circuit of the PID controller, where the resistance of Trimmer 1, 2 and 3 are around 2.2, 0.28 and 0.85 KΩ, respectively; the switch is also shown on the box cover (see Fig. A.5); R_I and R_D are special resistors designed to solve some issues, as explained in the text.

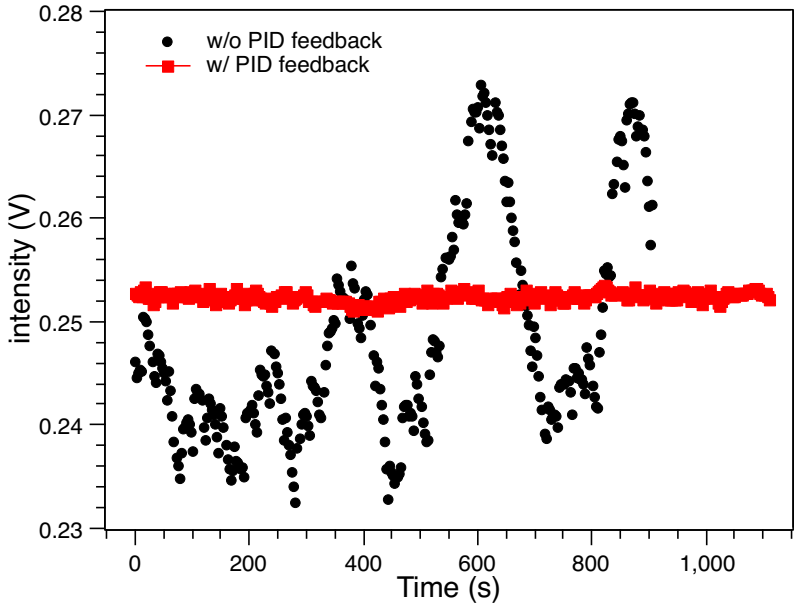

Figure A.7: The stability test of the control field power. The PID feedback system reduces the power fluctuation to less than 1%.

References

[1] A. S. Sedra and K. C. Smith. *Microelectronic Circuits*. Oxford, 7th edition, 2015.

[2] P. E. J. Dodge. Eliminating Parasitic Oscillation between Parallel MOSFETs. *Power Electronics Technology Conference*, Issues with Paralleling MOSFETs and IGBTs, 2003.

[3] K. J. Aström and T. Hägglund. *PID Controllers: Theory, Design, and Tuning*. International Society of Automation, 2nd edition, 1995.